UNIVERSITY
OF TRENTO - Italy
DEPARTMENT OF INDUSTRIAL ENGINEERING

XXXI cycle

Doctoral School in Materials, Mechatronics
and Systems Engineering

New methodologies of Silk Proteins processing for advanced applications

Alessio Bucciarelli

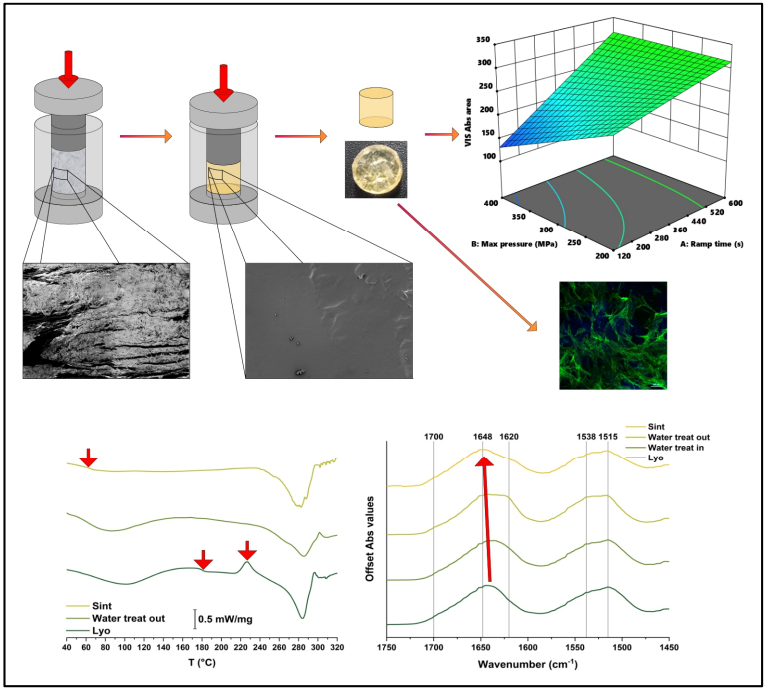

October 2019

NEW METHODOLOGIES OF SILK PROTEINS PROCESSING FOR ADVANCED APPLICATIONS

Alessio Bucciarelli

E-mail: Alessio.Bucciarelli@unitn.it
Bucciarelli@fbk.eu

Approved by:

Prof. Alberto Quaranta,
Department of Industrial Engineering
University of Trento, Italy.

Prof. Devid Maniglio,
Department of Industrial Engineering
University of Trento, Italy.

Ph.D. Commission:

Prof. Antonella Motta,
Department of Industrial Engineering
University of Trento, Italy.

Prof. Ines Mancini,
Department of Physics
University of Trento, Italy.

Prof. Martin Humenik,
Department of Molecular Bioscience
University of Bayreuth, Germany.

University of Trento,
Department of Industrial Engineering
October 2019

University of Trento - Department of Industrial Engineering

Doctoral Thesis

Alessio Bucciarelli - 2019
Published in Trento (Italy) – by University of Trento

ISBN: - - - - - - - - -

Abstract

Silk fibroin is a widely studied material in the context of tissue engineering. Thanks to its versatility and impressive properties, the fields where silk fibroin is used have grown. In particular, silk fibroin has proved to be useful in all the cases when an interface with living tissues is needed (e.g. biophotonics, bioelectronics). As a consequence of this increasing interest, a wide range of protocols have been developed to prepare different materials starting from cocoons.

The aim of this thesis is to investigate new strategies to fabricate silk fibroin-based materials, either improving previously developed protocols or proposing new methodologies both with the purpose to overcome certain limitations of current approaches and to propose new areas of application. We choose to work on three topics: the production of patterns using photolithography on a fibroin photoresist films (fibroin photocrosslinkable photoresist, FPP), the production of sponges made from a chemically modified version of the native protein (Methacrylated fibroin, Sil-MA), and the production of a solid bulk resin made starting from the regenerated protein.

In the case of the FPP (and its counterpart made of sericine, SPP) the fabrication of films and pattern was restricted to the use of harsh chemicals. In addition, the resulting material had a roughness that limits its use in optical applications, making the determination of the refractive index (RI) not possible. The novelty of our work consisted in the modification of the original protocol to make it environmentally sustainable and to decrease the roughness in order to use ellipsometry to determine the RI dispersion.

The broadly used silk-based sponges can be prepared by several protocols but they all suffer of the same limitations: the sponges are stabilized only by physical crosslinking (the change from the random to the crystalline secondary structure), and there are no clear models that correlate the sponge properties to their composition. We produced a new sponge, chemically crosslinked, whose stability was ensured by the creation, of chemical bonds between the protein chains during an UV curing. This task was accomplished using a simple protocol and a statistical method to model the composition-properties relations.

The possibility to obtain a bulk, non-porous solid monolith from fibroin (solid-fibroin) has been received attention only in the last few years. This material is produced by a transition from solution to solid through solvent evaporation, a very slow process that takes weeks to be completed. The advantage of this transition is that it occurs at room temperature, allowing the addition of thermally degradable molecules (e.g. enzymes). We were able to optimize a procedure to produce the same material by compression of a silk sponge at high pressure and low temperature. The advantage of this method is the lower amount of time required to produce the material, minutes instead of days.

Preface

This thesis represents several months of my research work in three research projects over the course of the 3 years of my PhD studies at the University of Trento. My project started with an internal collaboration inside the Industrial Engineering Department, between prof Alberto Quaranta, a physicist with a wide experience in optics, and prof. Devid Maniglio who is also a physicist working on biopolymers. This allowed me to become part of the Biotech Research Center team, and to meet prof. Motta, who, albeit in an unofficial capacity, guided me throughout my entire PhD career. The initial idea of this project concerned optical sensors made of fibroin, and this led us to collaborate with both Dr. Vamsi Yadavalli, head of the Bionano group at the Virginia Commowealth University, who developed the protocol to produce a photoresist made of silk fibroin and for the part related to the optical characterization, with Dr. Viviana Mulloni, of the Micro System Technology group in Fondazione Bruno Kessler. Then my interest in silk proteins as a material, and the freedom that all my advisors gave me, allowed me to move to the general topic of processing and fabrication of materials from silk fibroin. In this wider context, we were able to

develop a new approach to produce a solid non-pours bulk fibroin as an alternative to the sol-gel-solid transition from the aqueous solution. Later during my PhD studies, thanks to the support provided by the REMIX project (founded by the EU's Horizon 2020 Marie Sklodowska Curie action), I enjoyed the opportunity to spend 3 months in the laboratory of prof. Gilson Khang at the Chonbuk National University, located in Jeonju, South Korea. There, I focused my research on the development of a stable crosslinked foam, starting from a chemical modification of fibroin protein. This thesis focuses on material fabrication from silk. I voluntarily excluded other studies in which I collaborated but that were unrelated to the main topic. The structure of this work consists of three main parts related to the three materials studied. In all cases, at the beginning each chapter, I will introduce the novelty of my approach and the reasons that took me to modify or create these new protocols. This thesis is written treating silk as a biopolymer, from the material science viewpoint; I want to apologize from the beginning if this could result inaccurate or incomplete from other perspectives. I hope that this work would be useful to

those who will come after me in the road of silk, as the footprints of the people in front of me were the beginning of my journey.

Table of Contents

1. Introduction

Silk is an animal fibre spun from the specialized glands of a certain number of arthropods and annelids to build their cocoons or webs. This material has been known by humans since ancient times. Since of sericulture and the introduction of the techniques that allowed to obtain a continuous fibre from cocoons, silk has been used as material to produce ornaments and high-value textile.

Nowadays, the main application of silk fibres remains basically the same as centuries ago: the textile production. Nonetheless, thanks to its intrinsic properties, the commercial usage of silk has spread to different fields: dietary applications, as a precursor for cosmetics and in pharmaceutics. As far as the scientific community is concerned, the driving mechanism behind the studies on this material is the unique balance of its properties such as good tensile strength[1–3], elasticity[1–3], resistance to fracture[1–3], biocompatibility[2,4,5], and easy processability[2,6–9]. In particular, proteins derived from silk fibers have found their natural applications in tissue engineering and all the emerging fields in which well-known technologies have been extended to biological applications (bio-electronics, bio-

photonics, bio-sensing, optics, microfluidics)[10]. All these interesting developments have led to the advance of countless manufacturing techniques.

Although, the majority of procedures for the material preparations starting from *Bombyx mori* cocoons have been unified and standardized in a protocol in 2011 by *Rockwood et al*[9], other procedures, especially the ones adopted for advanced technological applications, were excluded. In particular, in the Rockwood protocol, all the methods that imply a chemical modification of the native protein[11], as the one used to produce a fibroin photoresist[12,13] or a solution suitable for DLP 3D printing[14], and all the methods used for the preparation of a solid bulk fibroin[15–18] are missing. Some of the newest techniques were not standardized, or they were not suitable for an up-scaling; other techniques were used without being optimized for the application they were intended for.

The standardization and optimization of procedures to fabricate materials starting from silk are usually tricky, because silk proteins tend to be susceptible to many factors: the secondary structure, the molecular weight and, consequently, all the physical responses depend upon process variables.

Therefore, the leap from the scientific world to real applications is still a challenge for an unconventional material as silk proteins. In the industry, the standardization and optimization of processes is accomplished by a modeling procedure that allows to know exactly how the variables considered affect the material properties. This was rarely accomplished in the case of silk fibroin, especially for the preparation of “new materials”.

The goal of this thesis was to investigate new strategies to fabricate silk fibroin-based materials, either by improving previously developed protocols or by proposing new methodologies, with the aim to overcome certain limitations of current approaches. We chose to work on three topics: the production of a pattern using photolithography deriving from a fibroin photoresist (fibroin photocrosslinkable photoresist, FPP), the production of sponges deriving from a bio-ink (Methacrylated fibroin, Sil-MA), and the production of a solid bulk resin starting from the regenerated protein.

In case of FPP[12] (and its counterpart made of sericine, SPP[19]) the fabrication of films and patterns required the use of harsh chemicals and the resulting material presented a roughness that made the determination of the refractive index

(RI) difficult. The novelty of our work was to modify this protocol to make it environmentally sustainable and to decrease the resulting roughness in order to be able to perform ellipsometry to determine the RI dispersion[20,21].

Widely used sponges can be prepared by a number of different protocols[22–27] but they all suffer from one common limitation: the sponges can be stabilized only by physical crosslinking (the change from the random to the crystalline secondary structure) and there are no clear models that correlate the sponge properties to their composition. We produced chemically crosslinked sponges; whose stability was ensured by the creation of chemical bonds between the protein chains during a UV curing. This task was accomplished using a very simple protocol and implementing in our study a statistical method to model the composition-properties relations.

The possibility to produce a bulk fibroin resin (solid-fibroin) has received attention only in recent years[15,28]. This material is obtained by a transition from solution to solid through solvent evaporation over several weeks[15]. We were able to optimize the procedure to produce the same material in minutes instead of days. In our case, we decreased the working

temperature down to 40°C using high pressure and a starting material with low crystallinity (a silk sponges produced by lyophilization), combining the speed of the compression with the low temperature of the evaporation.

1.1. A brief story about silk

According to Chinese myth, Lady Hsi-Ling-Shih, wife of the Yellow Emperor who is said to have ruled China in 3,000 BC, was the inventor of both sericulture and of the loom upon which silk is woven[29]. Silk, initially and for a long time, was reserved exclusively for the Chinese Emperor, his family and for dignitaries with a very high rank. This restriction on who could wear and use silk in China, was gradually relaxed and those who could afford this precious material could soon be seen wearing silk clothing and silk ornaments.

Eventually, the silk production grew to a large industry in China. Silk, in fact, became a material suitable not only for making luxury textile but useful also for a large variety of other applications: from fishing-lines and bowstrings to musical instruments. Silk became somewhat of a currency during the

Han Dynasty: in this era farmers were allowed to pay their taxes in grain, and, in turn, the state would also pay the salary of its civil servants in silk.

Sericulture spread into Korea around the year 200 BC and after 300 AD this practice became established in India. Around the year 550 AD sericulture arrived at the Emperor Justinian's court in Byzantium and, from there, by the 6th century, silk weaving was established in Persia. It was during the period of the Crusades that silk production reached Europe: skilled silk weavers from Constantinople arrived in Italy, setting up their business there.

The term "silk road" is far more modern, and it was originally coined by a German geographer, Ferdinand von Richthofen, to indicate the routes along which Chinese silk travelled to Central Asia during the Han dynasty. The term "silk road" was then taken from another German geographer August Hermann, who used it in the title of his essay: "The Silk road from China to the Roman Empire". In that essay "Silk road" acquired its modern meaning: the road linking the east to the west with the lucrative trade in silk carried out along its length. It was this trade that made it possible for people in places

located far away from any silk cultivation and silk weaving facilities to wear and use silk. However, it is a misconception to think about the silk road only as an east-west route; in fact, in fact, nowadays historians prefer to look at it as a network of complex routes connecting all the different middle-European countries where silk was commercialized[30,31].

1.2. Silk fibroin structure

Many insects and arachnids produce silk, mainly to accomplish two different tasks: either silk is used as protective external structure during the metamorphosis from larva to the adult life stage of an insect, or silk is used as a construct to catch preys (in the case of spiders). Among all the silk-producing species only few are used in the large-scale production of silk. The majority of commercial silk comes from the mulberry silk moths Bombyx mori, that has been domesticated for millennia to induce it to live in a closed environment and produce a larger quantity of silk.

The Bombyx mori cocoon is made of a single continuous fibre consisting of two main parts, as schematically

shown in **figure 1-1**: an external glue-like protein, named sericin, that protects two cores made of a mechanically resistant protein, called fibroin. These two proteins can be separated by a well-known procedure[9] (called degumming), in which Sericin is solubilized by a hot bath of sodium carbonate (Na_2CO_3). This bath leaves the fibroin unaffected, that can thus be recovered as solid fibrous product.

The starting point for materials preparations from the Bombyx mori cocoons is the production of a solution of the protein in its denaturated state (**Figure 1-1**): after the degumming process the fibroin fibres are washed and dried, then solubilized in a concentrate solution of lithium chloride (9.3M) that breaks the hydrogen bonding in the β-sheet structure and denature the protein. This process is usually performed at 60 °C for 4h in an oven. Subsequently, a dialysis is conducted for 3 days to remove the salt. The solution obtained is then used as it is to fabricate materials or to chemically modify the protein[11,12,14].

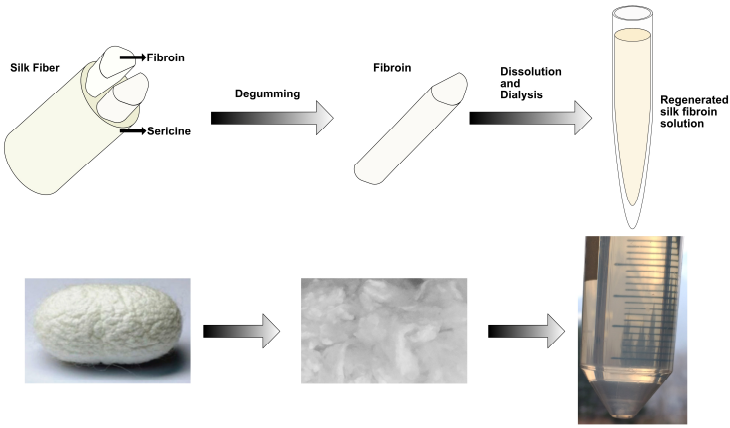

Figure 1-1: Process to obtain a regenerated silk fibroin solution, starting from the cocoons.

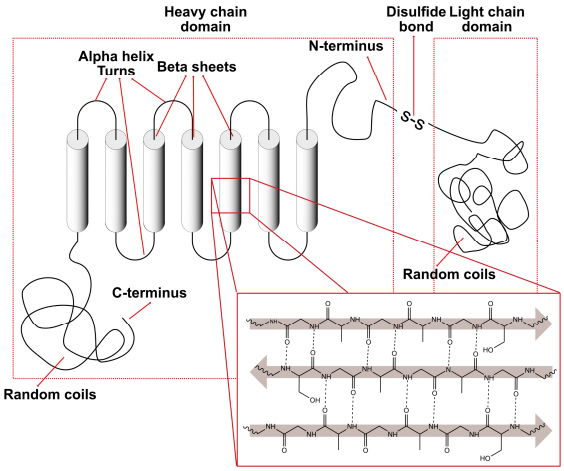

Figure 1-2: Structure of silk fibroin. Heavy chain domain (H), primarily composed by β-sheets strand and light chain domain (L) primarily in the random coil conformation.

A simplified scheme of the silk fibroin structure is shown in **Figure 1-2**: the protein is composed by heavy (H) and light (L) chains with a molecular weight of above 370 kDa and 26 kDA respectively[32]. These two chains are bonded with a disulphide bond to form a H-L complex that is able to bind another glycoprotein, called P25, in a ratio of 6:1 via hydrophobic interactions[1,27]. The 6 H-L plus the glycoprotein form the single micellar unit.

The heavy chain contains structures with a highly repetitive aminoacidic sequence such as $(Gly\text{-}Ala\text{-}Gly\text{-}Ala\text{-}Gly\text{-}Ser)_n$, $(Gly\text{-}Ala\text{-}Gly\text{-}Ala\text{-}Gly\text{-}Tyr)_n$, and $(Ala\text{-}Gly\text{-}Val\text{-}Gly\text{-}Tyr\text{-}Gly\text{-}Ala\text{-}Gly)_n$. which are mainly hydrophobic. These repetitive sequences, called strands, organize themselves in β-sheet crystallites giving a high mechanical stability to the spun fibre[33]. β-strands, in order to be packed, can organize themselves in two way: anti-parallel and parallel (**Figure 1-3**). In the anti-parallel arrangement, the C-terminus end of one segment is on the same side as the N-terminus end of the other segment. In the parallel arrangement, the C-terminus end and the N-terminus end are on the same sides for both segments[34]. The

formation of sheets occurs because of the alternating planes of the peptide bonds between amino acids[34].

The parallel arrangement is less stable because the geometry of the individual amino acid molecules forces the hydrogen bonds to occur at an angle, making them longer and thus weaker[34].Conversely, in the anti-parallel arrangement the hydrogen bonds are aligned directly opposite each other, making for stronger and more stable bonds[34].

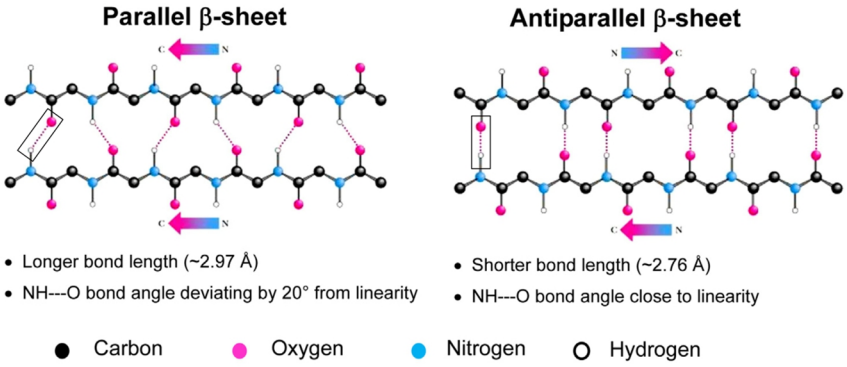

Figure 1-3: Parallel and antiparallel configuration of β-sheet. In the first case nitrogen atoms of different strands will face each other in the staking configuration (as well as the carbons atom), the h bonds are angled. In the second case nitrogen atoms will face carbon atoms, so the h bonds are aligned.

The crystallites are separated by a less ordered hydrophilic domain that forms the semi amorphous region with a secondary

structure, known as β-turn that facilitates the protein folding into micellar structures[1,2,27,33].

The Light chain, instead, presents a non-repetitive amino acid sequence, and a secondary structure that is mainly configured in random coils, with little or no crystallinity.

The two chains are very different from a structural point of view and this affects their physical properties: the heavy chain is rigid and hydrophobic; the light chain is flexible and hydrophilic. Even though the heavy chain dominates in terms of percentage in the total composition (by mass), the overall behaviour of silk fibroin is strongly affected by the presence of the light chain component[1,2,32,33]. The mixture between the rigidity and mechanical stability of the crystalline parts and the flexibility of the random coil part is the main reason for the impressive mechanical properties of silk[1,2,7,27].

1.2.1. Secondary structure determination by FTIR

Assignment	Peak position cm^{-1}	References
Side chain	1597-1609	[35–38]
Intermolecular antiparallel β-sheet	1610-1625	[35–37,39–46]
Native β-sheet	1626-1635	[35,38,40–45]
Random coil	1636-1655	[35,38,40,44,46,47]
α-helix	1656-1662	[35,38,40,44]
B-turns	1663-1696	[35,37,39,40,44,45,48]
Intermolecular parallel β-sheet	1697-1703	[35,44,45,49]

Table 1-1: Bands assignment in the FTIR deconvolved spectra.

Fourier Transform Infrared Spectroscopy (FTIR) has been commonly used as a technique to determine the protein secondary structure. In fact, the shape of the Amide I peak (approximately in the 1720-1580 cm^{-1}) resulted to be dependent on the secondary structure conformation[35].

In many studies, a transition of this peak to lower wavenumber has been used as proof of the protein transition to the crystalline stable β-sheet structure[50–54] without any further analysis. However, even though that approach is common and well-established, more sophisticated methods involving the use of a Fourier Self-

Deconvolution (FSD)[55–58] to enhance the spectral resolution, allowed to discriminate different β components. A crucial aspect in using FTIR in combination with FSD, is the peak assignment. Usually this assignment is done by checking the peak position and comparing it with a reference table. In all the structural analysis conducted in this thesis the reference table used is **Table 1-1**.

While the other assignments (Side chain, Random-coil, α-helix and β-turn) are well-established (see the references in **Table 1-1**), our choice for bands assignment of the different β-sheets structures needs an in-depth explanation. Supported by several works in literature[42,43], in a recent paper the distinction between the peaks related to parallel, antiparallel and native β sheet has been made[40].

The band between 1610 and 1625 cm^{-1} (centred around 1622 cm^{-1}), usually present in most crystallized protein[39,46], can, in the case of silk fibroin be assigned to the intramolecular antiparallel β-sheet structure[35–37,39–46]. Analysis performed on the second-derivative spectrum shown that this band increases during the isothermal

crystallization whereas the side-chain bands remain stable[35]. In some studies[35], inside this band 2 peaks could be recognized; in most of our cases, after the FSD only one component has been found[59].

The second band between 1626 and 1635 cm^{-1}, named β-native, can be associated to beta-sheet-like[60], or to non-bonded beta-sheets[61], or to irregular pieces of extended chain structures similar to the beta-sheets[62]. The same band was also found in the bio-synthetized silk I structure[45] which was used as a model in NMR studies to substitute for the less ordered (non-crystalline) silk fibroin[63]. In other studies, the peak related to the native β structure has been used to distinguish the globular protein in solution from its aggregates[41,43]. The spectral shift to a lower wavenumber has been recognized as a reorganization of the β secondary structure that, during the transition to fibre, can differ from the native by the average number of strands per sheet, and possibly, the sheet twist[43]. A more recent work, involving the natural fibroin protein extracted from the gland of the silk-worm proposed the distinction between the β structure of the native protein (β-native) in solution

and the β structure in silk micrococoons (Intramolecular antiparallel β-sheets) obtained from self-aggregation into a microfluidic device. In this case, the transition to a lower wavenumber of the Amide I peak (and consequently an increasing of the peak associated with the Intramolecular β antiparallel structure) has been suggested as an explanation for formation of aggregates such fibrils. This shifts of the amide I peak toward lower wavenumbers has been associated with the formation of intermolecular hydrogen bonds[40]. It should be noticed that in the same study, even in the aggregates the presence of the β-native peak has been recognized, and the relative abundancies of the native β structure and the intramolecular β structure have been correlated with the different morphologies of the micrococoons[40]. In our work, the variation of the percentage of secondary structure associated with the β-native peak was related to the higher stability of a lyophilized sponge between and after water annealing[59].

The third band associated with β-structures is 1697-1703 cm^{-1} and it is associated with the thermodynamically unstable β-parallel sheets[35,44,45,49].

1.3. Materials from silk fibroin

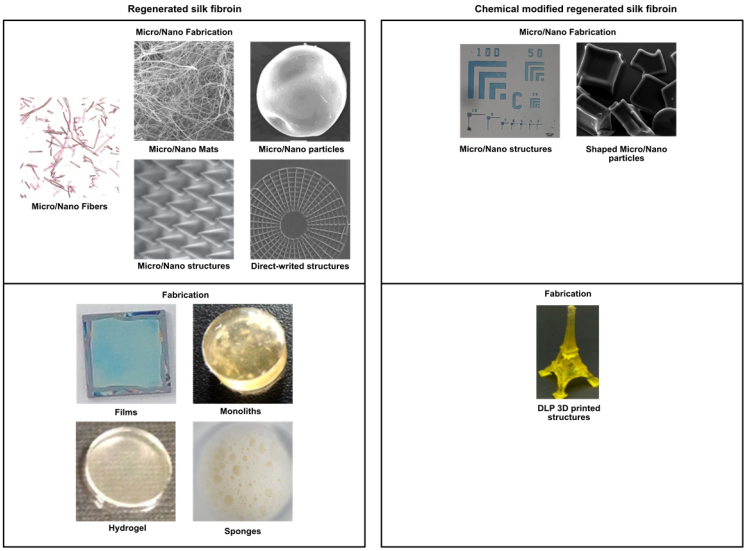

Figure 1-4: Materials derived from silk fibroin. On the left from regenerated silk, on the right from the methacrylated fibroin. A further subdivision has been done to divide microfabrication to fabrication processes.

After the degumming protocol, starting from the aqueous solution of the regenerated silk fibroin an entire set of different materials has been made (**Figure 1-4**). These materials are mostly used in tissue engineering to fabricate complex structures aiming to mimic the natural ones. Natural materials are usually composed by several layers of complexity:

from nano/micropatterns at microscopic scale to macro patterns recognizable at higher scale[7]. This degree of complexity had led to the use of sophisticated techniques (e.g. soft-lithography, nanoimprinting, photolithography, 3D printing, sintering) in combination with biopolymers, and in our specific case, with silk fibroin.

Some processes for the material production are more suitable for the fabrication in the micro/nanoscale while others can be used to fabricate macro scale objects. Even if in some cases this distinction proves difficult, a general definition of nano/micro fabrication can help to make a classification. A micro/nano fabrication process is a technique that allows to produce micro or nanofeatures with predesigned shapes, maintaining a certain degree of control on their dimensions.

The main scope of “microfabrication” is to produce micrometric features; from then, the production of macro-object is achieved through a “bottom-up” approach. On the contrary, “fabrication” techniques are used to produce macroscopic objects that could have, as a second order of complexity micro/nano peculiarities, partially controllable using a “top-down” approach. Using this distinction, as shown in **Figure 1-5**,

sponges should be considered as “fabricated” constructs, because a partial control on the porosity can be exercised. Mats and nanomats, instead, are “microfabricated” because the fabrication process begin from an accurate control on the fibre diameter.

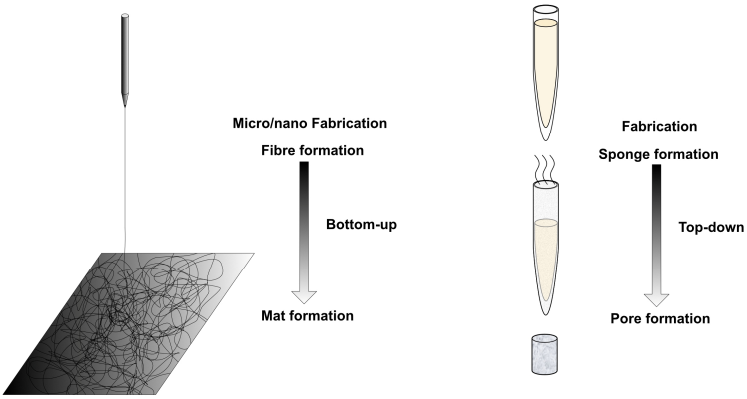

Figure 1-5: An example of the difference between micro/nanofabrication and fabrication. In the case of mats formation, the first step is the spun of the microfibre, then the mat is developed through multiple depositions of fibres in a sort of “bottom-up” approach. The sponge preparation requires, starting from a regenerated silk fibroin solution, a freeze-drying process. The micrometric features (pores) require a sort of “top-down” approach.

Another useful distinction can be made between the techniques that use unmodified and chemically modified fibroin: in the specific context of fabrication, the most useful modification consists of the addition of methacrylate groups that

allow the crosslinking of the material through UV light exposure. This method combined with conventional photolithographic techniques[12,13,20] permits to obtain both micrometric and nanometric patterns and, using the 3D digital light processing (DLP) printing[14], macroscopic objects.

1.3.1. Fabrication techniques

Materials obtainable from silk fibroin solution are listed in **figure 1-1**; the techniques that allow to obtain macroscopic objects are briefly described in the list below. We divided the list in techniques that require the natural protein and in the ones that need the addition of methacrylate groups and the successive chemical crosslinking.

Materials deriving from the aqueous solution of regenerated silk fibroin:

- Sponges: fibroin sponges are frequently used as scaffolds for bone and tissue regeneration. They provide mechanical support in combination with biocompatibility, tunable biodegradability, and the possibility to host bioactive molecules[5,25,27,64]. The key feature of this material is its interconnected porosity.

Pore size with a diameter larger than 100 μm is considered essential for cells growth and migration[65]. Sponges should also be stabilized to avoid the rapid dissolution in water; This can be accomplished by a conformational transition to the stable β sheets structure. Different methodologies are reported to produce porous scaffolds among them are salt leaching, gas foaming, and freeze drying. Salt leaching uses a salt as porogen: the silk solution is over-saturated with salt so that the bulk of it is retained as solid[25,66]. The particle size determines the size of the pores. Such salts as $NaCl$ or KCl are able to directly promote the transition to the crystalline form[65]. After the solvent evaporates the salt residue inside the scaffold can be removed by dipping it in water. If necessary, a supplementary step to allow the transition to the crystalline stable form can be performed by immersing the sponges in methanol, ethanol or other solvents that can promote the transition. Other methods incorporate bubbles in the silk solution. As an example, we report here two of these techniques: the first

consists in the addition of ammonium bicarbonate to the solution. This salt decomposes when the scaffold is immersed in hot water, allowing the formation of gas and consequently pores[25]. The second method consist in the use of a siphon filled with silk fibroin solution in which NO_2 is expanded forcing the solution through a nozzle and allowing the formation of a stable sponge[24]. Lyophilization, is a method that uses ice particles as pores template. the pore size can be determined by controlling the process parameters (time and temperature)[67,68].

- Hydrogels and crosslinked hydrogels: hydrogels are polymeric, three-dimensional networks that entrap water. They possess a mechanical behaviour that resembles that of solids, and they can incorporate other components such as cells and drugs. The formation of a network implies a crosslinking reaction, which can be physical or chemical. In case of pure silk fibroin solution, the crosslinking is mainly physical and is usually accompanied by a random to beta structure transition during the gelation time[69]. The transition to a

gel is usually driven by methods that give energy to the system allowing the secondary structure transition. These methods include sonication[70,71], the application of a shear stress[72,73], the concentration of the fibroin solution[74,75], its pH change[76–78], and the electrogelation[79,80]. A chemical crosslinking can be induced adding to the solution molecules (e.g. metallic ions[81], horseradish peroxidase[82] in combination with hydrogen peroxide, riboflavin[83], ruthenium[84], Sodium dodecyl sulfate[85]) that promotes the formation of dityrosine and trityrosine bonds.

- Films: fibroin films have a limited utility when used without any post-processing. The technique to produce fibroin films is generally selected on the basis of the thickness and roughness needed. Thick films (>10 μm) are usually obtained by solvent casting: the fibroin solution is placed on a substrate and then the solvent is let to evaporate. Thin and ultrathin films can be prepared by spin coating or layer-by-layer deposition (LBL)[86]. Recently, silk fibroin films were investigated as coatings for food storage and conservation. The results

indicate that with the increase in film crystallinity both strawberries and bananas went to a slower degradation if compared with the uncoated fruits[87]. Silk films has been extensively exploited as support for metallic layers to make conformal bio-electronics[10,88–92] and food sensors[93]. These applications were the results of the possibility to transfer metals to the fibroin substrate via mold imprinting[94]. The imprinting process allows to transfer the features of a mold to the film substrate through a thermal reflow mechanism[95,96]. This mechanism was also studied to form laminates of stacked protein films[97] used to protect and control the degradation of bioresorbable devices.

- Monoliths: only few methods are available to produce a solid bulk fibroin material, the first proposed several years ago[16,18] and recently repurposed[17] based on a hot pressing of silk fibroin with or without the addition of water. The temperature needed to get a full densified material was between 100 and 200 °C. This solid-solid transition is not well understood, but water is known to act as plasticizer decreasing the glass transition

temperature thus allowing the phenomena of thermal-reflow to occur at a lower temperature. The other method consists in a liquid-gel-solid transition that occurs when the solvent is allowed to evaporate from the regenerated silk fibroin solution[15]. The time needed for a complete evaporation is usually long ranging from several weeks (using water as solvent) to several days (using 1,1,1,3,3,3-Hexafluoro-2-propanol as solvent). The great advantage of this method is the fact that this transition occurs at room temperature thus allowing the addition of thermally degradable biomolecules. With this last method a cranial fixation system was developed and tested in vivo[28].

Some fabrication techniques, as said before, require an additional modification of the protein, in particular the addition of methacrylate groups to allow a chemical UV or thermal crosslinking. The techniques listed below all required the protein methacrylation:

- DLP 3D-printed structures: recently, a photocurable silk fibroin resin was produced through a simple reaction

involving glycidyl methacrylate (GMA) and silk fibroin[14,98]. This resin (Sil-MA) was printed using a digital light processing (DLP) 3D printer to obtain objects with complex shapes, and with the addition of cells directly into the ink. The developed material retained water inside a 3D crosslinked structure, therefore the results was a hydrogel with mechanical properties tunable in accordance with the initial concentration of Sil-MA. From the fabrication perspective the interesting part of this technique is the possibility to directly convert a CAD drawing into an object.

1.3.2. Micro fabrication techniques

Following the definition of micro-fabrication as techniques that allow to carefully control the shapes and the dimension of the micro/nano features, the subsequent materials are obtainable with silk fibroin:

- Mats and Nanomats: these materials are produced to mimic the extracellular matrix (ECM) and then used in wound healing[99]. The most common production

technique is electrospinning: it basically consists in the acceleration of the solution passing through a needle, due to the presence of a high potential difference between the needle and the collector[100,101]. The attractive force of the collector and the repulsive force of the solution charges produce a tensile stress that forces the ejection of a fibre from the needle. Many variables influence the diameters of the fibre such as the type of solutions, instrumental settings, and environmental parameters. The type of the solvent used, the viscosity and the concentration of the solution, its conductivity, the molecular weight of the protein are all parameters related to the solution. The applied potential, the geometry of the configuration, the size and geometry of the needle used are the parameters related to the instrument. Finally, the humidity, the temperature and the air velocity are environmental parameters[102].

- Micro and nanoparticle: this kind of particles found their natural application in drug delivery systems[103–105]. Several methodologies have been adopted to prepare

them: spray drying from aqueous solution[106,107], lipid-aqueous separation[108], laminar jet[109,110], polymer phase separation[111,112], organic-aqueous phase separation[110], pH variation[113] and ball milling[114,115]. Each technique is specific to obtain a determinate size distribution. Nanoparticles are used as fast-releasing drug carriers administrated via intramuscular, intravenous, oral, subcutaneous, or transdermal route. Their nanometric dimension allows them to penetrate through biological barriers. Microparticle, on the other hand, are used to slow release systems.

- Micro and nanofiber: micro and nanofibers can be produced by self/assembly or by electrospinning[116]. The regenerated protein in aqueous solution, due to its instability in the solubilized state, tends to form different nanostructure with different sizes from nanosphere to nanofibers. In this process, the negative charge of the molecules play an important role. Starting from the spontaneous formation of nanoparticles an accurate control of the zeta potential in an iterative drying-dissolving process, allows to obtain microfibers[117]. A

transition from micelles to nanofibrils in a fibroin water solution can be obtained by controlling the pH. The pH is slowly decreased from 6.5 to 4.8 through the addition of chloridric acid (HCl), promoting the formation of β crystalline structures thus the formation of fibrils[118]. Another approach consists in exfoliating the degummed silk fibre to obtain nanofibrils. This can be achieved by placing the degummed fibre in hexafluoroisopropanol (HFIP) or HCl, incubate it and finally sonicate to obtain the nanofibrils [119,120]. Another well-known procedure consists in the treatment of the degummed fibroin in alkali solutions. This treatment that can be conducted with different reagents, allows the hydrolysis of amide bonds. The length of the resultant microfibers is inversely proportional to the bathing time[121].

- Microstructures: using silk fibroin solutions as it is micro- and nano- structures can be easily obtained by direct imprinting[95]. This technique consists in heating a fibroin film above its glass transition temperature and to imprint a microstructure by the use of a micropatterned

mould[95,96,122,123]. The regenerated protein solution can be also used as photoresist both positive or negative in accordance to the technique used (electron beam lithography, multiphoton lithography, microprinting) [124–126]. As negative resist, a film of regenerated silk fibroin is physically crosslinked in specific points, then the uncrosslinked part is washed to reveal the printed micro- or nano- structure. Instead, in case of positive resist, a crosslinked film is de-crosslinked in specific points and then the developing phase (as in the previous case) reveals the structure. Natural silk fibroin has been used in combination with riboflavin to produce microstructures through photolithography. Riboflavin in conjunction with light exposure can promote the formation of dityrosine and trityrosine chemical bonds, ensuring the crosslinking of the exposed parts[83].

- Direct writing: using a micrometric nozzle mounted on a 3 axes computer controlled stage, complex 3D structures are achievable[127]. The silk fibroin solution ejected from the nozzle undergoes a gel transition that allows the direct deposition on a substrate. Using a

layer-by-layer deposition of a lattice of silk fibroin, macroscopic objects with controlled micrometric features can be obtained[128]. This technique used in combination with cells is known as bioprinting. This allows the direct encapsulation of cells into the fibroin 3D-printed structure[129–131].

Similarly, to the previous section, the techniques reported below required the protein chemical functionalization by attaching vinyl groups:

- Micro/Nano structures: the methacrylation of the natural protein through the use of an isocyanate leads to the development of a high-grade methacrylated protein (fibroin photocrosslinkable photoresist, FPP) that can be used as photoresist in photolithographic processes[12,13,132]. Using the same approach silk sericin can be modified as well[19]. Microstructures can be obtained by a contact photolithographic process[12,13,20,133–135]. Nanostructures have been recently achieved by electron beam lithography, in this case FPP has

been proven to act both as negative or positive resist in accordance to the energy used in the e-beam[136].

- Shaped micro/nano particles: using FPP it is likewise possible to produce particles with well-defined shapes. The preparation method consists in the UV crosslinking of a FPP film through a micropatterned mask, the development to reveal the shaped particles and the successive lift-off of the particles from the substrate[137].

1.4. Protocols insight

In this paragraph, some insight into the techniques treated in the next chapters will be given. In particular, on how to form a sponge by foaming, a resin by sintering and a micropattern by photolithography. The first two techniques commonly require the regenerated silk fibroin solution. To produce high-resolved patterns, instead, a chemical modification is needed; therefore, two methods to methacrylate the natural protein will be also described.

1.4.1. Foaming

Gas forming uses bicarbonate salt (e.g., ammonium bicarbonate or sodium bicarbonate) as the surfactant added to silk solution, with a surfactant-to-silk weight ratio of 10:1 or 20:1. After drying and beta-sheet crystallization in alcohol, the scaffolds are immersed in 95 °C water to induce gas foaming and remove/dissolve the bicarbonate particles[25].

There are a variety of approaches to generate air bubbles in a silk solution: after rapid crystallization by alcohol or by freezing before crystallization, with the air bubbles used to produce the pores in the scaffolds[25].

A recent method proposes the direct foaming of the silk fibroin solution by the use of a siphon in which the addition of nitrous oxide (N_2O) allows the formation of bubbles. The successive expulsion through a nozzle promotes the direct transition to the stable β secondary structure due to the shear stress applied[24].

1.4.2. Sintering

Sintering essentially consists in a thermal treatment that bonds particles into a coherent, predominantly solid, structure via mass transport events that often occurs on the atomic scale[138]. This technique is mainly used in ceramic and metal industry to melt particles to form complex objects. For most materials the interdiffusion at particle boundaries play the main role. In the conventional process, after the compaction of the particles, the thermal treatment inside a furnace allow the grain interdiffusion and thus the formation of a continuous solid[139].

Silk fibroin powder has been reported in literature to form a compact resin by sintering. The resins were formed in a temperature range of 100-200 °C by applying pressure from 20 MPa to 100 MPa[16–18] for 30-60 min. The mechanism of the formation of a compact material from fibroin is not clear[16–18]. In fact, unlike ceramic and metal particles, fibroin does not melt, but only degrade when the temperature increases[53]. It is known that the addition of water in silk materials decrease the glass transition temperature (T_g) down to 40 °C[140]. This was used in

several processes to induce a thermal reflow of the material in order to obtain microstructures[97,123].

1.4.3. Photolithography

To better understand the content of the second and third chapters where, in different procedures, a UV crosslinking takes place, a brief introduction of the photographic techniques is here presented. Photolithography is a technique to fabricate micropatterns, originally used in electronics to develop printed circuit board. Basically, it uses light to transfer a pattern on a light-sensitive material called photoresist, by exposing it to light through a microstructured mask.

A schematic illustration of this technique is shown in **figure 1-6**. The resist is usually deposed on a substrate, whose nature depends on the application. UV light is then shone through a mask, which selectively allows light through certain regions in order to generate a pattern on the resist. Historically, the mask has been made of quartz, with chrome patterns on top that control where the light shines through the mask. The radiation pattern from the UV light induces chemical changes in

the resist, which selectively modify the solubility of the exposed regions in a liquid called developer.

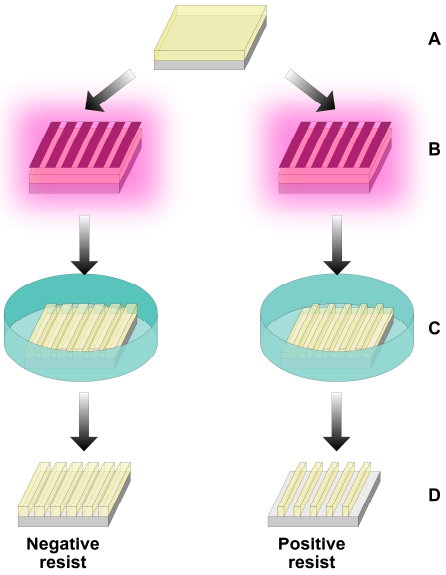

Figure 1-6: Schematic procedure of conventional photolithography. The photoresist is deposited on a substrate (usually silicon), then exposed through a micropatterned mask to UV-light to imprint the microstructure. A chemical bath is used to develop the resist, removing the unexposed part, in case of negative resist, or the exposed part, in case of positive resist.

According to the chemistry the exposed parts are, in case of negative resists, polymerized or crosslinked, making them insoluble; instead, in case of positive resists, decomposed, making them soluble. Then a developing bath is used to remove the soluble parts from the resist, exposing the

microstructure[141]. Photoresist can be divided in three major categories (**Figure 1-7**): photopolymeric, photocrosslinking, and photodecomposing.

The first category of reactions involves the formation of free radicals that initiate a radical polymerization; this includes all the negative resists that contain monomers with a double carbon-carbon bond that opens during the polymerization, as allyl groups or methacrylate groups (**Figure 1-7 A**).

The second category includes negative resists that due to the UV exposure generates crosslinking bonds between polymer chains (**Figure 1-7 B**). In case of silk fibroin, a crosslinking can be accomplished by the addition of Riboflavin that promotes the formation of dytirosine and trityrosine bonds between protein chains when irradiated with a 450 nm light[83]. The same mechanism can be promoted by the addition of a Rhutenium complex and an exposure to UV light[84]. Another method suitable for silk fibroin crosslinking is its chemical modification by the addition of methacrylate groups, that can be opened by the use of a photoinitiator and UV exposure[12][14].

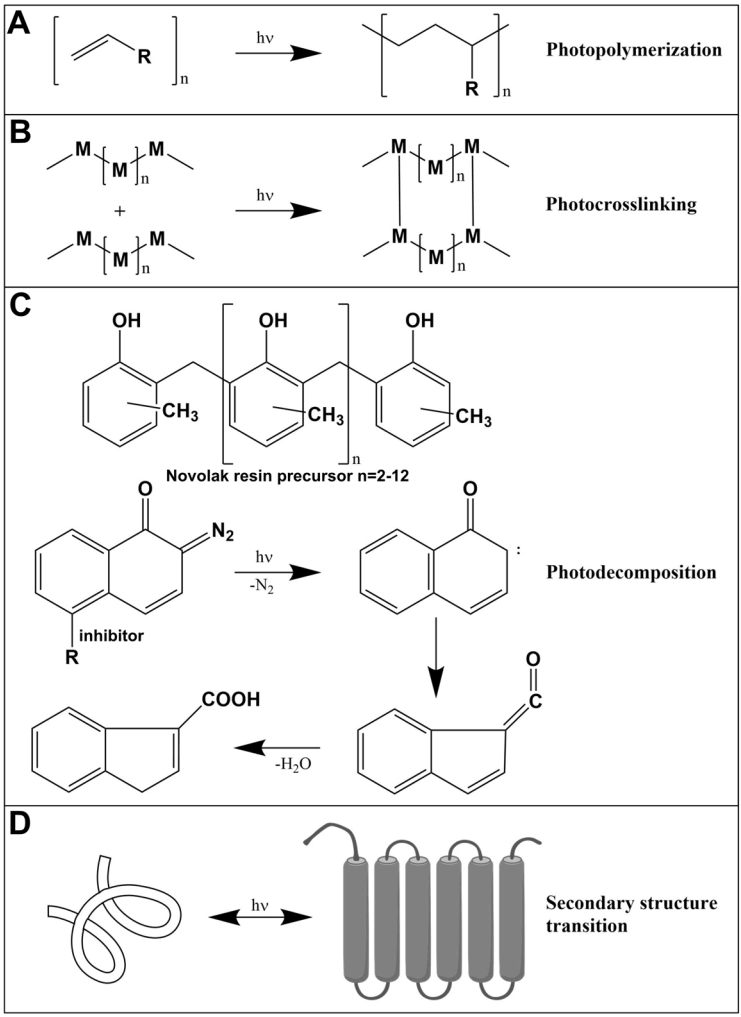

Figure 1-7: Scheme of photoreaction that can occur in photoresists. Photopolymerization and photocrosslinking are both reactions suitable for a negative resist. The difference between the two of them is basically determined by the formation of bonds between monomers (photopolymerization) or bonds between pre-existent polymer chains (photocrosslinking). Photodecomposition is the reaction that occurs in case of negative photoresist: it involves the decomposition of a molecules to give a soluble product.

The third category of reactions is used for positive resists and is based on molecules that decompose when exposed to UV light, making the material soluble in a determined solvent. The basic polymeric compound for these photoresists is Novolak resin precursor (**Figure 1-7 C**), that is usually soluble in alkali solutions. For resist applications this solubility is inhibited by the presence of a photoactive compound that undergoes to photolysis during the exposure to UV radiation, allowing the exposed part to be removed using an alkaline bath.

In case of proteins, and more specifically of silk fibroin, a fourth mechanism should be added: the conformational change (**Figure 1-5 D**). In fact, depending on the secondary structure, fibroin can be water-soluble or insoluble: the transition from the amorphous random coil to the crystalline β-sheet structure makes the protein stable in water. This phenomenon improperly reported in literature as “crosslinking” does not imply the formation of interchain bonds; rather, intrachain h-bonds are formed during the transition to β structures. The process is then reversible, and in some condition the protein can be denaturated again, making it water-

soluble. For this reason, silk fibroin can act both as positive and negative resist. High β-structured films acts as a positive resist: techniques as electron beam lithography (EBL) and ArF excimer laser lithography allow to obtain a transition to amorphous phase[124][126]. Instead, amorphous films acts as negative resists and EBL promotes the transition to β structure[126].

1.4.4. Chemical modifications of silk fibroin

There are several chemical reactions that allow to graft methacrylated groups on the aminoacidic chain. In the next chapters two different approaches to achieve fibroin methacrylation will be adopted.

The first, illustrated in **Figure 1-8 A,** consists in the use of an isocyanate that, due to its high reactivity is able to form different types of bonds: amide, urea and urethane[12,13]. The second one, illustrated in **Figure 1-8 B** consists in the reaction of the modification of the lysine residue by the use of an epoxy group[14].

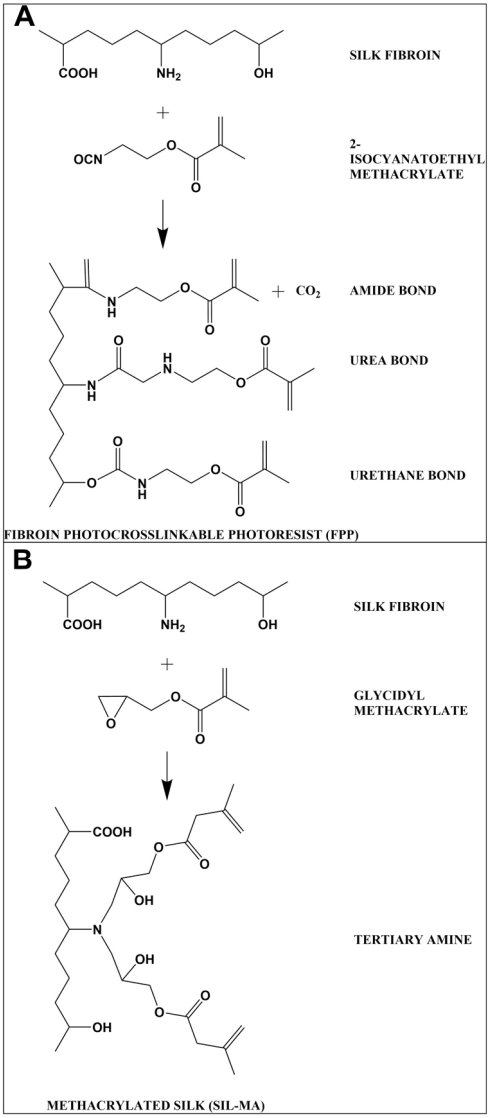

*Figure 1-8: Scheme of the chemical modification of silk fibroin that allows the addition of methacrylate groups, (**A**) using an isocyanate, (**B**) using an epoxide. The product of the first reaction (FPP) is not water-soluble, while the second product is developed to be in water solution (Sil-MA).*

The product of the first reaction, namely fibroin photocrosslinkable photoresist (FPP), is solid and is not water-soluble. In order to solubilize this material 1,1,1,3,3,3-Hexafluoro-2-propanol (HFIP)[12,13] was used as solvent. The high methacrylation rate of this material consents a high resolution patterning: from the micrometric scale, using the conventional photolithographic approach[12,13], to the nanometric scale using the electron beam lithography (EBL)[136]. However, after crosslinking the product is still soluble in the solvent, so it is not possible to use it in technique as the DLP 3D printing, where the insolubility of the crosslinked resin in the same solvent where the photocurable resin was initially dissolved is a prerequisite.

The second reaction uses water as solvent and the resultant methacrylated protein is still denaturated a in water solution. The advantage of this approach is that the Sil-MA can be used in all those cases where the toxicity of the solvent is an issue and, since the crosslinked SIL-MA is not soluble in its solvent (water), it can likewise be used in application as the DPL 3D printing[14].

2. Design of experiment (DOE)

Only in few studies design of experiment has been used in literature[142–144] to optimize methods of material fabrication from Bombyx mori cocoons, and, in nearly all cases it was used to evaluate a single yield on well-established procedures. Instead, DOE is universally used as statistical technique to optimize and standardize the industrial production[145–147]. In this chapter, basic statistical procedures will be illustrated with the purpose of providing some instruments to understand the data analysis performed in the following chapters. This entire chapter is adapted from material extracted from few books on the argument[145,147–149].

2.1. One-variable-at-time versus design of experiment

One of the common approaches to perform an experiment is the one variable at a time (OVAT) where one variable at a time is changed, while keeping all other variables fixed. The success of this method often depends on the intuition and the experience

of the experimenter. Moreover, the OVAT method may yield false optimum condition for the process[146].

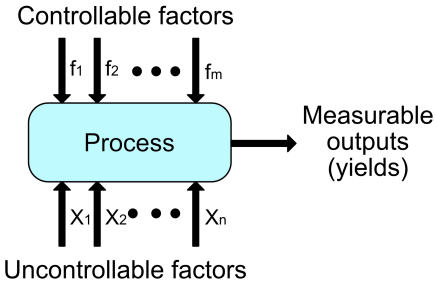

Figure 2-1: Block scheme of a process. Both controllable and uncontrollable factors influence the measurable outputs.

When several variables are involved in the process a more efficient way to conduct a reliable experiment that can provide insight into the process is Design Of Experiment (DOE).

In the DOE method the process can be considered as a "black box" (**Figure 2-1**) in which controllable and uncontrollable factors influence the measurable outputs. The controllable factors are easily changeable and under control during the experiment (e.g. the temperature and the pressure in a reaction chamber, the quantity of reagents, the volume of solvent). Instead the uncontrollable factors are parameters that change independently over time (e.g. environmental parameters such as temperature, pressure, and humidity). Measurable outputs

(yields) are all those properties that require an optimization (e.g. the elastic modulus, the particle size).

In comparison with the OVAT the use of the DOE allows the estimation of the factor interactions and how they influence the yields. The main aim of DOE is to model the factors-yields relationship and to determine the optimal setting of controllable factors to minimize the effect of the uncontrollable factors on the yields (robust design).

In the experiments performed in **chapter 3** and **4** we decided to adopt the DOE approach to characterize and optimize new protocols.

2.2. Basic principles in DOE

To conduct a correct experiment using the DOE method some basic procedures are usually performed. Not all of them are always needed because their use is mainly related to the process and how the trials are performed.

- **Randomization**: On the assumption that the variation of the uncontrollable factors is aleatory their effect on the yield can be considered random and, on a first assumption, normal distributed. To minimize the impact

of uncontrollable variables, a total randomization of the trials is always performed. In all our experimental design was used a full randomization of the trial.

- **Replicates:** Replicates are repetition of trials. The production of more than one replicate allows the estimation of the experimental error, and to obtain a more precise analysis of the factor's interactions. However, for an exploratory experiment (more specifically in cases when the experiment is complex or too expensive, or the quantity of the material required is significant) a single replica is sufficient.
- **Blocking:** Blocking is a method of eliminating the effects of extraneous variations due to noise factors and thereby improves the efficiency of experimental design. The main objective is to eliminate unwanted sources of variability such as batch-to-batch, shift-to-shift, operator-to-operator, etc. The idea is to arrange similar experimental runs into blocks (or groups).

2.3. 2^N Full factorial design: an example

An easy an efficient way to perform a DOE when the number of factors to be taken into consideration is small (<5) is the 2^N full factorial design. In this design, each factor is considered at 2 level, low (-1) and high (+1) and the trials include every combination of the factor levels.

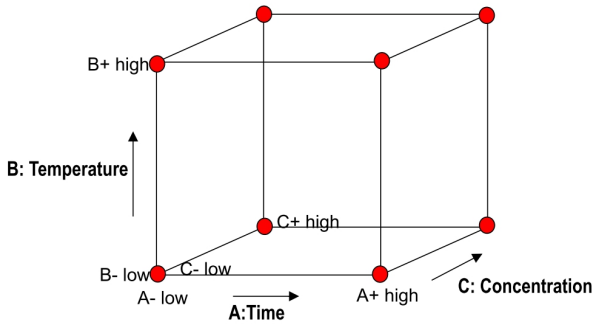

Figure 2-2: 2^3 Full factorial experimental design. Each factor is tested on two levels (high and low). The experiment requires to test all the combination of levels from different factors.

An example of this design is reported in **Figure 2-2** for 3 factors. In this case, the variable space is three-dimensional, and the number of required trials is 2^3. The complete predictive equation of this design is:

$$Y = \beta_0 + \beta_1 A + \beta_2 B + \beta_3 C + \beta_4 AB + \beta_5 AC + \beta_6 ABC$$

	Main effects			Interaction effects				Yield
N	**A**	**B**	**C**	**AB**	**AC**	**BC**	**ABC**	**Y**
1	-	-	-	+	+	+	-	74
2	+	-	-	-	-	+	+	75
3	-	+	-	-	+	-	+	71
4	+	+	-	+	-	-	-	80
5	-	-	+	+	-	-	+	81
6	+	-	+	-	+	-	-	77
7	-	+	+	-	-	+	-	42
8	+	+	+	+	+	+	+	32
Effect	-1	-20.5	-17	0.5	-6	-21.5	-3.5	66.5

Table 2-1: Effect matrix for a 2^3 design of experiment. Levels are listed as +(high) and –(low). So, for example, the first trial requires all the factors to be at the high level. The interaction effect level is obtained by multiplying component factor levels.

The complete matrix of the effect is shown in **Table 2-1**; in the matrix we added as example one yield (Y_1) in the last row and the calculated effect of each factor. To calculate, for example, the effect of the factor THE mean of the yield values obtained with a low A level are subtracted to the mean yield values obtained with a high A level; in equation:

$$E_A = \frac{Y_{A+}}{4} - \frac{Y_{A-}}{4} = \frac{74 + 75 + 71 + 80}{4} - \frac{81 + 77 + 42 + 32}{4} = -1$$

The first evaluation of the impact of the factors on the yield can be done by plotting the effect in the half-normal plot. This implies to sort the absolute value of effects in ascending order, divide the 0 to 100 % cumulative probability scale into n equal segments (with n equal to the number of effects) and plot the data at the midpoint of each probability segment. **Table 2-2** shows the sorted data of the example: each probability segment is approximately 14.28 % (100/7). The lowest weight will be plotted at 7.14 %, which is the midpoint of the first segment.

Point	Factor	|Effect|	Cumulative Probability (%)
1	AB	0.5	7.14
2	A	1	21.43
3	ABC	3.5	35.71
4	AC	6	50
5	C	17	64.29
6	B	20.5	78.57
7	BC	21.5	92.86

Table 2-2: Cumulative probability associated with the controllable factors. The effects were sorted in ascending order and associated with the corresponding cumulative probability.

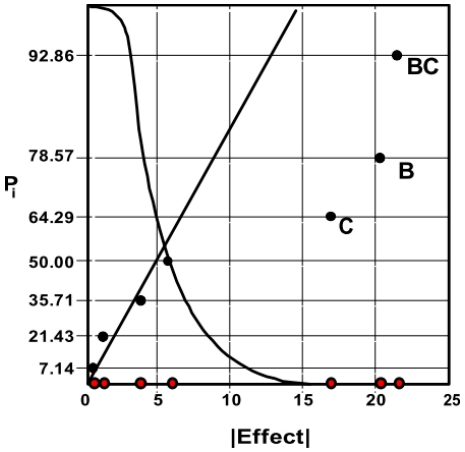

Figure 2-3: Normal plot of the proposed example. The effects out of the normal curve are significant. In the specific case only the term B, C and BC should be included in the predictive model.

In **Figure 2-3** the analysis conducted on the example data shown. The most significant effects fall out of the tail of the normal curve (to the right). These three effects (C, B, and BC) are most likely significant in a statistical sense. The other effects (AC, ABC, A, and AB—from biggest to smallest, respectively) fall in line, which represents the normal scatter in this graph. These four trivial effects (nearest 0) are used as an estimate of error for the analysis of variance (ANOVA). When the levels are restricted to two, the calculation of the sum of squares is simple.

Therefore, the sum of square for the factor X is calculated as follow:

$$SS_X = \frac{N}{4}(E_X)^2$$

When added together, the sums of squares of the effect that resulted to be significant in the half-normal plot, provide the beginning of the ANOVA of the model. In the specific case of the proposed example:

$$SS_{Model} = SS_B + SS_C + SS_{BC} = 2343$$

The sum of squares of the other effects are summed to provide the residual:

$$SS_{Residual} = SS_A + SS_{AB} + SS_{AC} + SS_{ABC} = 99$$

The ANOVA table is shown in **Table 2-3**. The degree of freedom (Df) of each term, only in the case the 2^N full factorial design, is equal to the number of effects counted in the sum of squares.

The mean of squares (MS) is calculated as the ratio of SS and Df, in equation:

$$MS = \frac{SS}{Df}$$

The F value is computed by dividing the MS by the MS of the residual:

$$F = \frac{MS}{MS_{Residual}}$$

	Sum of squares (SS)	**Df**	**Mean of squares (MS)**	**F value**	**Prob>F**
Model	2343.0	3	781.0	31.5	<0.001
B	840.5	1	840.5	34.0	<0.001
C	578.0	1	578.0	23.3	<0.001
BC	924.5	1	924.5	37.3	
Residual	99.0	4	24.8		
Cor Total	2442.0	7			

Table 2-3: ANOVA table for the proposed example. Both the model and the factors composing it are tested to verify their significance.

To understand the significance of each factor, the F-value should be compared with a reference F-distribution with the same degree of freedom; in the example the degree of freedom is 3 for the numerator (equal to the degree of freedom of the model and 4 for the denominator (equal to the degree of freedom of the residual). The critical distribution is shown in **Figure 2-4**.

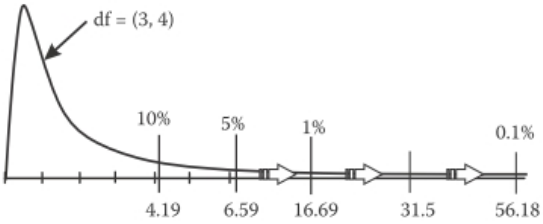

Figure 2-4: Reference t distribution for df= (3,4). In the example case the model has an F-value of 31.5 that resulted to be in the tail of the distribution, between 0.1 and 1 % of probability.

In this case the F-value of the model is between 0.1% and 1%, so we can state that the probability to get an F as higher as the actual one, only by chance, is less than 1%. In other words, we are 99% confident that the yield is affected by the terms chosen in the model. The same test has to be performed for each factor chosen to avoid to insignificant terms. However, for each term we must consider the correct comparison distribution that, for

instance, in case of the factor A is 1 for the nominator and 4 for the denominator.

Depending on the risk that we are willing to tolerate we can choose whether a factor should be considered significant or not. In the specific case of our study we will include in the model all the terms that have an F-value that in the F distribution resulted to be <10% (corresponding to a P-value<0.1). Basically, we decided that, due to the variability in the process and in the raw material, we could tolerate a 10% confidence risk.

2.3.1. The predictive model

A predictive model is a mathematical equation that is used to predict a specific yield based on the factor values. For example, the linear model for a yield influenced by 1 factor (A) is shown in **Figure 2-5**. Here, the equation of the model represents a straight line:

$$\hat{Y} = \beta_0 + \beta_1 A$$

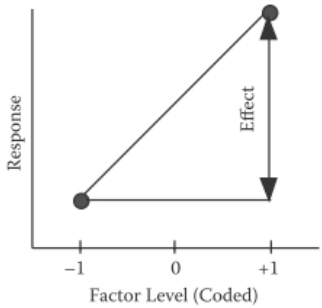

Figure 2-5: linear model for a single factor.

Using, for the sake of simplicity, the factor in its coded value (varying from -1 to +1), the intercept β_0 is the overall yield mean, and the coefficient β_1 is the effect of the factor A divided by two; in equations:

$$\beta_0 = \bar{Y}$$

$$\beta_1 = \frac{E_A}{2}$$

With more than one factor the predictive equation becomes progressively more complex; however, the calculation of the coefficients remains the same. The complete equation for 3 factors is:

$$\mathrm{Y} = \beta_0 + \beta_1 \mathrm{A} + \beta_2 \mathrm{B} + \beta_3 \mathrm{C} + \beta_4 \mathrm{AB} + \beta_5 \mathrm{AC} + \beta_5 \mathrm{BC} + \beta_7 \mathrm{ABC}$$

Not all factors have to be included; in fact, following the example of the last paragraph, we can provide a predicting equation:

$$\hat{Y} = 66.5 - 10.25\,B - 8.50\,C - 10.75\,BC$$

The equation given with factors in coded form allows the direct comparison of the effects by comparing coefficients values. All the predictive equations in our study were reported in form of coded factors. The use of these equations as predictive requires their conversion into equations with factors in non-coded form (expressed in their unit of measurement). This can be done by linear regression.

3. Materials and methods

3.1. Regenerated silk fibroin solution and chemical modifications

3.1.1. Silk fibroin solution

Extraction and purification of silk fibroin was conducted using an adapted version of a well-known protocol[9]. In short, to separate silk fibroin from silk sericin, Bombyx mori silk cocoons have been cut in small pieces and placed in a 0.01 M hot bath of sodium carbonate (Na_2CO_3, Sigma Aldrich) for 1 hour, followed by a second immersion in a bath of sodium carbonate with a concentration of 0.003M for 1 hour. The resultant silk fibroin, progressively taken to room temperature, was carefully rinsed for 3 times using ultrapure water and then dried for 2 days.

3.1.2. Lyophilized silk fibroin

The regenerated silk fibroin solution was placed into 15 mL vials that were frozen using liquid nitrogen and freeze-dried for 3

days to obtain the lyophilized silk fibroin used for the sintering process.

3.1.3. Methacrylated silk fibroin solution (Sil-MA) preparation

Sil-MA was prepared following a protocol described elsewhere[14]. Briefly, 20 g of the degummed silk fibroin were dissolved into 100 mL of a 9.3 M water solution of lithium bromide (LiBr, Sigma Aldrich) at 60°C for 4 h in an oven. Subsequently, 10 mL of glycidyl methacrylate (GMA, Sigma Aldrich) were added to the solution, which was stirred at 65°C for 4 h in order to allow the conjunction reaction. To remove the salt and the unreacted GMA, the resulting Sil-MA solution was dialyzed for 4 days against water using a 3.5 kDa dialysis tube. The solution concentration in mg/mL was checked using a spectrophotometer (BioSpectrometer basic, Eppendorf) evaluating the intensity of the A280 protein peak (280 nm). The solution was concentrated (10 or 20 %) evaporating the water at low temperature by the use of a rotavapor (Eyela N-1110AN) at 70°C and 300 rpm, checking the concentration at regular intervals until the desired one was reached. The resultant Sil-

MA water solution was then filtered with a 50 μm filter paper and then stored at 4 °C.

3.1.4. Synthesis of fibroin and sericine photoresists (FPP and SPP).

Briefly, fibroin protein was completely solubilized in 1M solution of LiCl (Sigma Aldrich) in DMSO (99.9%, Fisher Scientific). After the addition of a stoichiometric quantity of 2-isocyanoethyl methacrylate (IEM, Sigma Aldrich), the solution was maintained under stirring for 5 hours at 60° C to allow the conjugation reaction. The entire procedure was conducted in an anhydrous environment under continuous nitrogen flux. The solution was poured into an excess of cold ethanol in order to precipitate the fibroin with methacrylate conjugated side groups. The collected methacrylate protein was washed and centrifuged three times in a mixture of 50% cold, 200 proof, ethanol (Koptec) and 50% acetone (Alfa Aesar). The final product, fibroin protein photoresist (FPP), was obtained after 48 hours of lyophilization[12]. The same process, but using a different amount of IEM, was conducted starting from silk sericin to

obtain its crosslinkable version (sericin photocrosslinkable photoresist, SPP)[19].

3.2. Protocols for material preparation

3.2.1. Sponges preparation

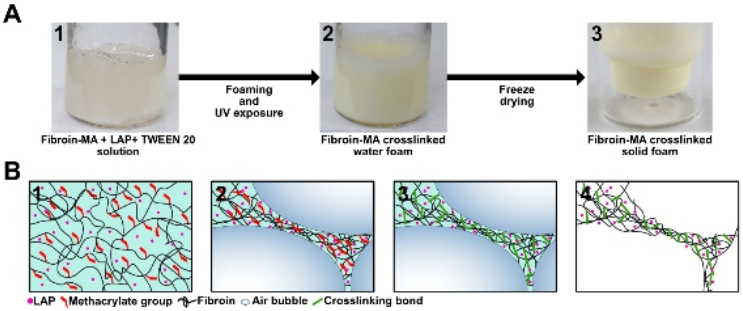

*Figure 3-1: (**A**) Method for Sil-MA foam preparation, **1** in the Sil-MA solution the photoinitiator (LAP) and the surfactant (Tween 20) were added, **2** the solution was then foamed using a mixer and exposed to a 365 nm UV light to stabilized the structure by chemical crosslinking, **3** finally to remove the excess of water the foamed solution was frozen at -80°C and then freeze dried to obtain the final material. (**B**) Proposed mechanism of sponge formation, **1** the double bond group are attached to the protein chain as side group, in the denaturated state of the protein these groups are highly reactive cause no steric impediment is present, **2** with the formation of the foam thin layer between air bubbles are formed, **3** the exposure to UV light ensure the opening of the double bond and the stabilization of the overall structure, **4** the freeze drying ensure the removal of the water leaving the final porous structure.*

Sample	[Fibroin–MA]	$V_{Tween20}$	m_{LAP}
	%	µL	mg
1	10	0	5
2	20	0	5
3	10	50	5
4	20	50	5
5	10	0	75
6	20	0	75
7	10	50	75
8	20	50	75

Table 3-1: Composition of the prepared sponges. We choose to vary the percentage of the protein in solution, the volume of the surfactant (Tween20) and the amount of initiator (LAP). Three samples were prepared for each composition.

We prepared 3 Sil-MA sponges for each composition shown in **Table 3-1**, for a total of 24 samples. The sponge preparation follows the scheme of **Figure 3-1**. Briefly, based on the sample composition, a certain amount of Sil-MA solution was transferred to a 15 mL glass vial, then the surfactant, Polyethylene glycol sorbitan monolaurate (Tween 20, Sigma Aldrich), and the photoinitiator, lithium phenyl-2,4,6-trimethylbenzoylphosphinate (LAP, Sigma Aldrich), were added. The solution was mixed and emulsified using a Bio-gen Pro 200 homogenizer (PRO Scientific) at 35000 rpm for 2.5 min. Immediately the structure was allowed to crosslink under UV

light (SpotLED curing equipment centered at 365 nm, Photo electronics) for 20 min. To ensure a more homogeneous crosslink the lamp was mounted inside a white chamber in where UV radiation could diffuse. The UV light itself is specially designed to guarantee minimal spot inhomogeneity (<10% on a 40 mm spot at 100 mm of distance from the lamp) Then the foam was frozen at -80 °C into an ultra-low freezer for 2 h and lyophilized at -50 °C for 2 days.

3.2.2. Sintering process

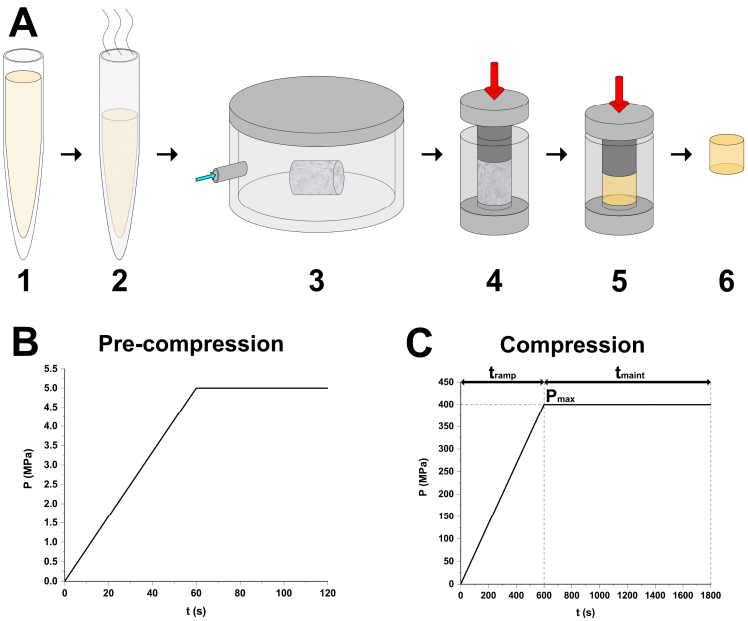

*Figure 3-2: (**A**) Steps of the overall process, 1 production of a fibroin solution, 2 rapid cooling with liquid nitrogen and lyophilization, 3 addition of water via moisture absorption in a humidostatic chamber, 4 a pre-compression phase uniform the initial material, 5 the compression phase in which the solid-solid transition occur and the fibroin pass from the lyophilized to the solid state , 6 the extraction from the mould. (**B**) Pressure vs. time pre-compression diagram: the pre-compression phase is the same for all the prepared samples, it consists in a compression ramp of 1 min to reach the pressure of 5 MPa that is maintained for another minute. (**C**) Pressure vs. time compression diagram: a maximum pressure is reached (P_{max}) during the ramp time (t_{ramp}) then this pressure is maintained for the maintaining time (t_{maint}). These three variables and the amount of added water ($m_{W\%}$, as fourth variable) were used to evaluate and optimize the process.*

Sample	Ramp time [s]	Max Pressure [MPa]	Maint. time [s]	Added water %
1	120	200	0	0
2	600	200	0	0
3	120	400	0	0
4	600	400	0	0
5	120	200	1200	0
6	600	200	1200	0
7	120	400	1200	0
8	600	400	1200	0
9	120	200	0	20
10	600	200	0	20
11	120	400	0	20
12	600	400	0	20
13	120	200	1200	20
14	600	200	1200	20
15	120	400	1200	20
16	600	400	1200	20

Table 3-2: List of the prepared samples for the optimization procedure. We chose to modify 3 parameters of the compression ramp (ramp time, maximum pressure, and maintenance time) and one parameter of the material (the amount of added water).

The compression of lyophilized silk fibroin was performed on a hydraulic universal testing machine equipped with a

thermostatic chamber allowing the temperature control within a range of ±1 °C (MTS 858 Mini Bionix, Italy) using a stainless-steel mold. The process is represented in **Figure 3-2 A**: the regenerated silk fibroin solution (**step 1**) was frozen in liquid nitrogen and then lyophilized (**step 2**) for 3 days at -50 °C; then a single block of lyophilized silk fibroin was placed into a humidostatic chamber with a controlled temperature of 25 °C and a constant humidity of 80 % for a time sufficient to reach a 20 % increment in weight, typically between 30 and 60 min. (**step 3**); subsequently, the material was placed inside the mold and a pre-compression (**Figure 3-2 B**) of 5 MPa was applied for 60 s (**step 4**). Then, the chamber was heated at 40 °C and a compression curve (**step 5**) was applied; finally, the resulting solid-fibroin was extracted from the mold (**step 6**). An example of compression is shown in **Figure 3-2 C**: the maximum pressure (P_{max}) was reached during the ramp time (t_{ramp}), then the pressure was kept constant during the maintaining time (t_{maint}). These three factors and the mass percentage of adsorbed water ($m_{w\%}$) were used to optimize the process in the design of experiment. The optimization required the preparation of 16 samples, listed in **Table 3-2.**

3.2.3. Spin coating process and film preparation

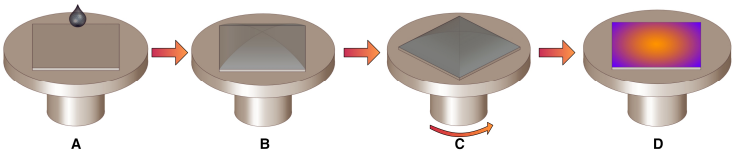

*Figure 3-3: modified spin coating process: (**A**) deposition of 70 µL of silk protein solution at low concentration, (**B**) delay time of 5 minutes in a closed chamber under nitrogen flux, (**C**) spinning and, (**D**) evaporation. This process allows the production of very smooth surfaces suitable for ellipsometry.*

Fibroin architectures were formed on silicon and glass substrates. To obtain a covalent adhesion of the protein to the surface, functionalization with acrylate groups was required. A bath of piranha solution (3 parts 98% H_2SO_4 and 1 part 30% H_2O_2 (v/v)) was used to clean the substrates for 30 minutes in ambient condition. The functionalization with 3-(trichlorosilyl) propyl methacrylate (TPM, Sigma Aldrich) was conducted using a chemical vapour deposition in a vacuum dryer for 12 hours at 0.4 bars. Surfaces were subsequently washed with methanol (Fisher Scientific) and water in order to remove any excess TPM.

Films for solvent comparison were prepared starting from a 5% (w/v) solution of FPP in formic acid (FA, Acros Organics 98%)

or in 1,1,1,3,3,3-hexafluoro-2-propanol (HFIP, Oakwood Chemicals). To obtain thin films (suitable for ellipsometric analyses) by spin coating, the concentration of the solution was reduced: protein resist (FPP/SPP) were dissolved in FA with a concentration of 1.5 wt.%, aqueous solution of silk fibroin was obtained by dilution of a 5 wt.% water solution to 2%, and FA solutions of silk fibroin and sericin were obtained by dissolving 2 wt.% of lyophilized silk fibroin and 2 wt.% of pure sericin in FA, respectively. In this case the concentrations were not kept constant in order to obtain films with a comparable thickness prior to ellipsometric analysis.

The samples for thickness comparison were prepared by casting the solutions on silicon substrates or using a spin coating process (SPS spin 150). An angular velocity ranging from 1000 to 4000 rpm was used (maintaining the other condition fixed such as angular acceleration: 200 rpm/s, duration: 60 s). To produce thinner films suitable for ellipsometric measurement (thickness and refractive index), the concentration was reduced to 1.5% and 1.2% w/v. In this case, the spin coating process (2000 rpm, 100 rpm/s2, 60 s) was conducted on TPM treated silicon surface. To reduce

environmental effects as much as possible the film deposition process was conducted inside a clean room with controlled temperature and humidity (T = 21 °C, H = 50%) and a specific optimized spin coating protocol (**Figure 3-3**). Briefly, 70 μL of a solution with a protein concentration of 1.5% or 2% was cast on a 1 cm^2 silicon surface (**Figure 3-3 A**). The solution was then left for 5 minutes in a closed chamber under N_2 flux (**Figure 3-3 B**) to allow the attachment of the protein to the surface. To form smooth thin films the process parameters used were optimized: the maximum speed was set at 2000 rpm with an acceleration of 150 rpm/s, for a total spinning time (both spinning **Figure 3-3 C**, and evaporation **Figure 3-3 D**) of 55 s. The evaporation step (**Figure 3-3 D**) was conducted at the maximum velocity of 2000 rpm for 40 s after the spinning ramp, to allow the complete removal of the solvent. The spinning parameters were kept constant regardless the solution concentration and the solute type (fibroin, sericin, FPP, or SPP). To evaluate the effect on the refractive index of the FPP and SPP exposure to UV radiation, 3 films for each type of resist were exposed for 2 s to UV at 365 nm and 2 mW/cm^2 (Lumen Dynamics OmniCure 1000).

3.2.4. Photolithographic process

Contact photolithography was used to produce a microscale test pattern. A photoinitiator (Irgacure 2959, BASF) 1.6% (w/v) was added to the FPP/FA 5% solution and mixed. Spin coating was conducted on functionalized silicon surfaces. To obtain the complete evaporation of the solvent the resulting films were stored for a few hours under a hood. Finally, films were exposed through a photomask for 2 seconds at 2 mW/cm^2 at 365 nm (Lumen Dynamics OmniCure 1000) and then etched in a 1M DMSO/LiCl solution for 2 hours. After an abundant water washing the micropattern was revealed.

3.3. Analysis

3.3.1. Characterization of silk fibroin sponges'

- **Structural analysis:** the structural analysis was conducted using an ATR-FTIR (GX Perkin Elmer), collecting 16 spectra in the 4000-400 cm^{-1} range with a resolution of 1 cm^{-1}. To understand if the methacrylation successfully occurred we analyzed 4 films: two (crosslinked and uncrosslinked) produced from Sil-MA

solution and the two others (treated and untreated with 12h of water annealing) from the regenerated fibroin. The films were chosen as the fastest method to test the on-going reaction in time. In fact, small amount of solvent can quickly evaporate under the hood, allowing a fast comparison between the product in different process steps.

Secondary structures were evaluated using an ATR-FTIR spectrophotometer (Perkin Elmer, Spectrum ONE). To maximize signal-to-noise ratio, 32 spectra with a resolution of 1 cm^{-1} were collected and averaged for each sample. The silk fibroin secondary structures were then quantitively evaluated analyzing the Amide I peak (1580-1720 cm^{-1}). The peak was smoothed with a 5-points averaging function followed by a base subtraction using a quadratic equation and a Fourier self–deconvolution (FSD, with smoothing factor of 0.3 and gamma function of 30) to enhance the resolution and better shape each single component. A second derivative of the deconvoluted peak was then performed to identify the component positions which

were consequently used to fit the singular peaks with a Gaussian function. The fitting routine was recursively applied until χ^2 was minimized. The ratio between the fitted peak area and the total area was calculated to determine the percentage of the specific structure assigned to the peak.

- **Porosity Distribution:** samples' porosity was evaluated by SEM (BioLV-SEM, S-3000N, Hitachi): two images at 60X magnification were taken for each sample.

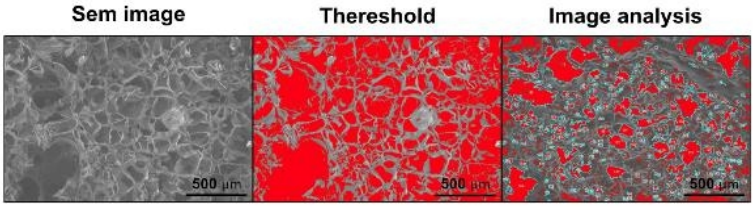

Figure 3-4: Image analysis of porosity distribution. Two SEM images at 60X magnification were taken for each sample; a threshold level was imposed in order to make clear the pore boundaries, finally the area of each closed pore was evaluated.

The images underwent an image analysis (ImageJ[150,151]) schematically shown in **Figure 3-4**. To individuate the pores, a threshold limit was imposed in

the grayscale. The pore shape resulted to not be circular, so we chose to evaluate the porosity referring to the parameter that can be evaluated directly from the thresholded image: the pore area. The pore detection and measurement were performed by an algorithm, that can include artifacts, especially in the low region of the porosity distribution. So, considering the scale of our image, only detected pores with a diameter higher than 1/10 of the scale bar (approximately 50 μm of diameter and 5000 μm^2 of area) were included into further calculations. Then the pores' median area, the interquartile range (IQR), the mean area, and the standard deviation were calculated and used as yield for the successive statistical analysis. An equivalent pore diameter was calculated by the strong assumption of circular porosity, using the formula:

$$\boldsymbol{d = 2 * \frac{\sqrt{A}}{\pi}}$$

where A is the estimated area.

- **Water absorption:** for each of the 8 compositions we prepared 3 sponges of equal weight (about 100 mg) for each time point (1, 3, 7, and 14 days). The sponges

were weighted directly after the freeze drying to ensure that the weight remained unaffected by the presence of water. Subsequently, the samples were soaked in 5 mL of simulated body fluid (SBF) at 37 °C inside a binder. The samples were then removed at the correct time point, rapidly dried with a filter paper and then weighted. The difference between the wet (w_{wet}) and the dry weight (w_{dry}) normalized to the dry weight has been used to report in percentage the adsorbed water using the following formula:

$$\boldsymbol{H_2O}[\%] = \frac{\boldsymbol{w_{wet} - w_{dry}}}{\boldsymbol{w_{dry}}} * \mathbf{100}$$

- **Dissolution in SBF:** the dissolution was evaluated using a spectroscopic method: the concentration in mg/mL of fibroin in the SBF solutions were evaluated by the use of a spectrophotometer (BioSpectrometer basic, Eppendorf) using the absorption at 280 nm (A280 protein peak, molar extinction coefficient of 44,700 $cm^{-1}M^{-1}$[152,153]). The resulting concentration ([rSF]) was then multiplied for the solution volume in mL (5), to obtain the total amount in mg of fibroin present inside the solution. The amount was then normalized to

the initial weight of the sponge (w_{dry}) and reported in percentage using the following formula:

$$\mathbf{m_{rSF}}[\%] = \frac{[\mathbf{rSF}] * \mathbf{5}}{\boldsymbol{w_{dry}}} * \mathbf{100}$$

- **Preliminary in vitro study (MTT assay):** NIH 3T3 cell line was used. RPMI medium was used in cell lines. This culture medium was supplemented with 10% fetal bovine serum and 1% antibiotic-antimycotic under standard conditions (37º C in a humidified atmosphere containing 5% CO_2). The metabolic activity of NIH 3T3 cell line was assessed by MTT assay[154]. The cells were seeded at a density of 2×10^5 cells/ scaffold and incubated with RPMI medium for 72 hours. Three replicates for each sample were incubated and cells cultured with RPMI medium were used as positive control. After 72 hours the cell culture medium was replaced with a culture medium containing MTT assay in a 9:1 ratio and incubated for 3 hours. When violet crystals formed, they were melted using dimethyl sulfoxide solution (DMSO) then the optical density was evaluated at 570 nm using a microplate reader. The results were plotted as percentage of the positive

control, reporting a mean and a standard deviation, then performing an ANOVA test to check if the results were statistically significant in comparison with the control. These data were further analized by DOE to verify if any second order effect influenced the cell viability.

3.3.2. Solid silk fibroin monolith characterization

- **Optical Characterization:** UV-Vis spectra, measured on both flat surfaces of each fibroin cylinder (two for each sample), were collected using a Jasco V-570 spectrophotometer (USA), through a black mask with a 6 mm diameter hole. The transparency indexes were evaluated by integrating these spectra on the visible range (from 400 to 700 nm) to obtain the areas, then calculating the average area value from the two results obtained for each sample and normalizing it for the sample thickness.
- **Mechanical characterization:** compression tests were performed using an Instron 7500 universal testing machine (USA) with a compression rate of 1 mm/min in

a controlled environment (25 °C and 20% RH). A pre-compression of 0.2 kN was applied prior the testing. The Young modulus was evaluated as angular coefficient of the curve in the initial elastic (linear) zone. The same procedure was used to evaluate the compressive young modulus of the material in wet condition at 37 °C, to simulate the environment of a body implant: among 8 solid silk fibroin cylinders produced by the optimized process, 4 were tested after being soaked into water at 37 °C for 6 hours, while the other 4 were tested after keeping them in a desiccator for 48 h at room temperature. The means and the standard deviations of both groups were then calculated.

- **Structural analysis:** secondary structures were evaluated by following the procedure described in **paragraph 3.3.1**.
- **Thermal analysis:** differential scanning calorimetry (DSC, Q20, TA instruments, USA) was used to evaluate the thermal behavior of the samples in the range between 40 and 320 °C. The tests were

performed under nitrogen flow (50 mL/min) using hermetic lids and a temperature ramp of 10 °C/min. Modulated DSC was done in the same range using a temperature ramp of 3 °C/min and a modulation amplitude of ± 0.5 °C and a period of 40 s.

- **Morphological analysis:** SEM analysis has been performed at 4 time points of the compression phase (0, 40, 80 and 120 s) to observe the thermal-reflow of the material. The samples were frozen in liquid nitrogen and cut with a blade to reveal the cross-section. The samples underwent Pt/Pd coating by plasma sputtering prior to SEM observation (FESEM, Zeiss Supra 60, Germany). Distances in the images were estimated by taking 30 measurements and reporting the means and the standard deviations.
- **In vitro cell study and confocal microscopy:** cell adhesion on LTS fibroin cylindrical samples (8 mm diameter, 3 mm height) was evaluated by culturing Adipose-derived Mesenchymal Stem Cells (AdMSCs). Samples with the same geometry made of Poly-ϵ-caprolactone (PCL, Sigma Aldrich) were prepared and

used as control. All samples were sterilized in autoclave at 121 °C for 15 min before seeding. AdMSCs (passage 3) were seeded on samples with a density of $6x10^4$ cells/cm^2 and cells were cultured up to 5 days, at 37 °C and 5% CO_2 in a humidified atmosphere. After each time point (1, 3, and 5 days), cell adhesion, morphology and distribution were analyzed by confocal microscopy (Nikon A1, Nikon Instruments, Amsterdam, The Netherlands) imaging. Before confocal observations, samples were fixed with 10% formalin solution (40 min, RT) (Sigma Aldrich), permeabilized with 0.2% Triton X-100 in PBS (30 min, RT) (Sigma Aldrich) and stained with CytoPainter Phalloidin-iFlour 488 Reagent (Abcam) to mark actin filament distribution of the cytoskeleton and DAPI (Sigma Aldrich) to mark the nuclei, according to the manufacturer's instructions.

3.3.3. Film Characterization

- **Thickness:** thickness profiles for solvent comparison were measured using a Veeco Dektak 150 Stylus Profilometer, with the mean and standard deviation

calculated over different areas on each film. Thinner films thicknesses were determined by a Horiba UVISEL 460 spectroscopic ellipsometer.

- **Morphological analysis:** asylum MFP-3D atomic force microscope (AFM) and Zygo New View 6300 optical profilometer were used to analyze film morphology and surface roughness. Imaging was conducted using a Nikon Eclipse LV100D optical microscope and a JEOL LV-5610 SEM instrument.
- **Optical analysis:** transmittance and absorbance measurements were conducted using a JASCO VR-570 UV-Vis spectrophotometer.
- **Structural analysis:** secondary structures for solvent comparison were determined by following the procedure described in **paragraph 3.3.1**. In this case, we collected 8 spectra per film with higher resolution (0.25 cm^{-1}); as a result the number of peaks discriminated was higher. For thinner films (used for RI determination) the secondary structure was revealed by FTIR Nicolet Avatar 330 using a Diffuse Reflectance (DRIFT) accessory, subtracting the bare silicon

substrate transmission spectrum as background. The analysis was then conducted following the procedure of **paragraph 3.3.1**. In case of DRIFT spectra fewer components have been recognized due to the low signal to noise ratio.

- **Thermal Analysis:** thermal analysis was conducted in the 30-330 °C temperature range using a differential scanning calorimeter (Mettler-Toledo DSC 20) with a heating rate of 10 °C/min fluxing nitrogen. Thermal gravimetric analysis (TGA) (Mettler-Toledo TG50 thermobalance) was conducted over 35-450 °C also in this case with a heating rate of 10° K/min in nitrogen atmosphere.
- **Refractive index determination:** for thinner films, RI were obtained using a Horiba UVISEL 460 spectroscopic ellipsometer, fitting 6 spectra for each protein/solvent combination (2 spectra from each of 3 films of the same type) using the Sellmeier and Cauchy models for transparent materials (formulae in **Table 4-2**).

3.4. Statistical methods

3.4.1. Photocrosslinked sponges

$Y = \beta_0 + \beta_1 A + \beta_2 B + \beta_3 C + \beta_4 AB + \beta_5 AC + \beta_5 BC + \beta_7 ABC$			
Variable	**Factor**	**-1 level**	**+1 level**
[Sil-MA] (%)	A	10	20
$V_{Tween20}$ (μL)	B	0	50
m_{LAP} [mg]	C	5	75

Table 3-3: Factors and their respective levels, considering a property Y a general model can be built to evaluate it as function of the considered variables. This model not only include a first order terms but also "mixed" terms that take into account the interaction between variables. Not all the terms are usually included into the model but only terms that are statistically relevant in accordance with the ANOVA test.

To evaluate the effect of the composition on the final properties of the sponges we conducted a 2^3 full factorial design of experiment (DOE), 3 variables were studied: the Sil-MA solution concentration, the volume of surfactant, and the amount of photoinitiator. For each variable we chose two levels (-1 and +1), listed in **Table 3-3**. Three samples were prepared for each of the 2^3 possible variables combination, for a total of 24 samples. For each sample we studied some properties of interest (yields) building a predictive model. In **Table 3-3** the general model is reported. This model includes all the first order factors that correlate the porosity directly to the composition

variables, the second order factors that consider how the couple of variables mutually interacts with each other, and a third order factor that takes into account the mutual interaction of all variables. A half–normal plot was used to evaluate which terms to include in the model and then an analysis of variance (ANOVA) test was performed to evaluate their significance.

3.4.2. Solid fibroin monoliths

$$Y = \beta_0 + \beta_1 A + \beta_2 B + \beta_3 C + \beta_4 D + \beta_5 AB + \beta_6 AC + \beta_7 AD + \beta_8 BC + \beta_9 BD + \beta_{10} CD + \beta_{11} ABC + \beta_{12} ABD + \beta_{13} ACD + \beta_{14} BCD + \beta_{15} ABCD$$

Variable	Factor	+1 level	-1 level
t_{ramp} (s)	A	600	120
P_{max} (MPa)	B	400	200
t_{maint} (s)	C	1200	0
$m_{\%w}$ (% w/w)	D	20	0

Table 3-3: Considered variables and their respective levels used to build the model equation (bottom). The variables are: the ramp time (t_{ramp}, factor A), the maximum applied pressure (P_{max}, factor B), the maintaining time (t_{maint}, factor C), and the percentage of added water ($m_{\%w}$, factor D). The equation includes first order terms, directly correlated to the variables, and higher order "mixed" terms.

Due to the presence of several process parameters, at such a low temperature it is extremely difficult to find the best

procedure for realizing the complete transition of the lyophilized fibroin to its compact solid state. So, the entire process was optimized with a 2^4 full factorial design of experiment (DOE) considering two levels (+1, -1) for each of the 4 studied parameters. The variables and their respective levels are listed in **Table 3-3**: the ramp time, the maximum pressure and the maintaining time were set directly in the hydraulic press. The last variable refers to use of lyophilized silk fibroin with or without water adsorption: 0% refers to the use of dry lyophilized fibroin, while 20 % refers to the absorption of a 20% (w/w) of water obtained by placing the lyophilized silk in a humidostatic chamber. The experimental design required the production of 16 samples (**Table 3-2**) applying all the possible combinations of the variables. To evaluate the transition from lyophilized to solid silk we chose to measure two physical properties: the sample transparency and the mechanical strength. Transparency was evaluated by calculating the area underlying the optical absorbance spectrum in the 400-800 nm range normalized by the sample thickness. These two parameters (yields) are used to build an empirical model that relate their value to the sintering parameters. The general equation for a 2^4

full factorial design is shown in **Table 3-3**. Pareto plot and half-normal plot followed by analysis of variance (ANOVA) test were used to discriminate the terms to be included in the model on the basis of their significance ($p<0.1$). The equations are reported with coded dimensionless terms, which implies that the all the variables are considered to vary between -1 and +1, allowing a direct comparison. For the sake of simplicity, we decided to report in the result section equations using coded terms and graphs using real variable values.

4. Photocrosslinked Sponges

Part of this chapter has been accepted for publication in:

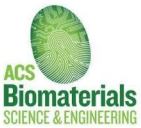

Preparation of a porous solid fibroin scaffold based on a foaming and UV crosslinking procedure of a methacrylate fibroin solution: evaluation of the influence of the composition on the sponge properties.

Alessio Bucciarelli, Muthukumar Thangavelu, Jin Su Kim, Won Kyung Kim, Alberto Quaranta, Devid Maniglio, Gilson Khang, Antonella Motta

4.1. Introduction

Silk fibroin sponges have been extensively studied in literature, in particular in all the applications where porosity is an essential feature. In tissue engineering porous structures serve as materials that closely mimic the biological microenvironment. Porous fibroin sponges have been successfully adopted in the case of soft tissues (muscle, skin, adipose, and neural tissues) and bones[5,27,155,156].

To produce an efficient scaffold, different parameters are essential. In order to mimic the living tissues the porosity should be open and tunable, the mechanical stiffness should be adjusted according to the treated tissue, and the sponge should be stable in water[157–160]. Plenty of different methods were

developed to produce silk fibroin sponges, among them: salt-leaching[161–164], freeze drying[22,26,165,166], freeze-thaw treatment[68], ammonium bicarbonate sublimation[167], self-assembly[168], and N_2O expansion[24]

All these methods are based on the transition of the protein secondary structure from random coil to crystalline β-sheet structure that makes the sponge stable in water. This transition, known as physical crosslinking, can be performed both with a post-production treatment as water annealing or the immersion in methanol or ethanol or using a method that produces by itself a stable crystalline sponge, as, for instance, the N_2O expansion[24]. However, the physical crosslinking, due to a change in the protein configuration, is less stable than a chemical crosslinking, in which the stability is ensured by the formation of a 3D continuous network of covalent bonds. Once the protein is in its β-form it could always be denaturated by solutions able to break the H-bond between the β-strands.

In this chapter we propose a simple and innovative method to produce a chemically crosslinked silk fibroin sponge with tunable porosity, and enhanced stability in water. The chemical crosslinking is ensured by the use of chemically

modified fibroin (methacrylated fibroin, Sil-MA), in which vinyl groups are added as side groups in the protein chain through a chemical reaction[14]. A foam is initially produced from the aqueous solution of Sil-MA by incorporating air using a mixer. The addition of a photoinitiator and the successive UV exposure allow the radical polymerization to take place opening the double carbon bonds, forming a 3D network and stabilizing the foam. Freeze-drying was used in the final step to remove the water and to obtain the sponge.

A design of experiment (DOE) was performed to model the porosity, the water absorption, the dissolution in a simulated body fluid (SBF), and the cell viability. In particular, we analyzed how the sponge composition influences the sponge properties. The 3 factors considered were: the protein concentration in solution, the quantity of photoinitiator, and the addition of a surfactant. The resultant sponges were analyzed by SEM and the mean and median pores area calculated within the standard deviation and the interquartile range. The secondary structure was evaluated by FTIR spectroscopy. The water uptake and the dissolution in SBF were evaluated by weight comparison.

Finally, to evaluate the biological response a preliminary cytotoxicity test was performed. Using our method, we proved the possibility to tune the porosity, its dispersion as much as the sponge degradation just by changing the initial composition. This could constitute a platform system to produce different kinds of scaffolds responding to the necessity of the different tissues to be treated. In addition, the possibility to change further process parameters could give, in the future, additional degrees of freedom, and probably an increase in the tunability range of the considered properties.

4.2. Results

Silk fibroin sponges were widely used in literature as scaffolds for different tissues: from bones to soft tissue. Different methods were used to fabricate this material and each of them gives a different distribution of the pore diameters. The porosity of a sponge and the possibility to tune it is extremely important to properly design a scaffold. The optimal pore size of the scaffolds depends on the cell phenotype and the target tissue: a structure in which both macropores and micropores

are present ensures both cell attachment and proliferation, and the neovascularization[169].

The prepared samples are shown in **Figure 4-1**. Only the initial composition of the sponge was changed leaving the process parameters constant. Interestingly, just from a visual comparison, we can clearly see how the amount of LAP can influence the colour of the sponge. This is not related to the colour of LAP, that results to be bright white in its solid form, and perfectly transparent in water solution. The colour could be, instead, related to crosslinking; in fact, it appears only after the UV treatment. Another noticeable difference is related to the sample uniformity: samples made by a 20 % solution presented visible holes in their structures and did not adhere to the vials' surface.

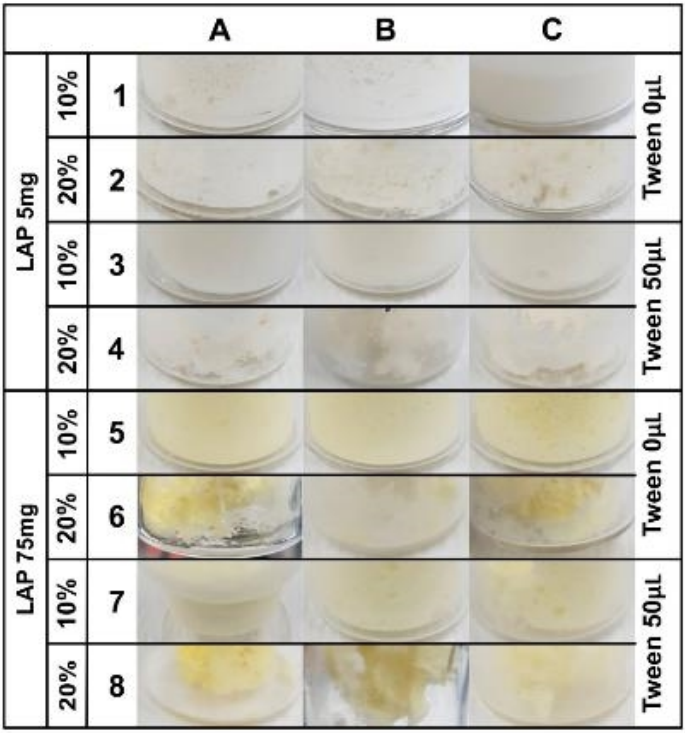

Figure 4-1: Prepared samples, A, B and C indicate the three replicas for each condition. Some trends can be recognized immediately: the addition of 75mg of LAP makes the samples yellowish after the photocrosslinking, this effect is present only on the skin of the sponges not inside; the samples prepared with a 10 % solution appears to be more uniform than the samples prepared with a 20 % solution; this can be attributed to a partial gelation during the process of the sample with higher concentration.

The higher crosslinking ensures a better performance in terms of stability in water, especially during the first hour (before the transition to the β structure, occurring due to the water treatment). The design of experiment method was

performed to understand which of the components of the sponge composition are crucial to modify the properties studied. The porosity was analyzed by SEM imaging and with an automated method for pore recognition and area measurement. FTIR confirmed the successful functionalization, and the fact that the composition does not influence the secondary structure. The dissolution test proved the influence of the quantity of photoinitiator and thus the level of crosslinking on the degradation of the sponge, especially after the first day of test.

4.2.1. Structural Analysis

Both the presence of functional groups and the protein secondary structure were studied by infrared spectroscopy (FTIR-ATR). In **figure 4-2,** the comparison between a lyophilized sample of regenerated silk fibroin and of the methacrylated silk fibroin is shown. In accordance with previous works[14], small variations of the spectra due to the presence of the functional group can be individuated on the methacrylated silk fibroin films (both crosslinked and uncrosslinked) in comparison with the unmodified (**figure 4-2 A**). In particular the

peaks at 1265 cm^{-1} (CHOH stretching)[14], 1165 cm^{-1} (CH2 wagging stretching)[14] and the modification of the Sil-MA spectra in the 960-1080 cm^{-1} range (vinyl out of plane CH bending)[170], indicate the presence of the functional groups. These peaks can also be recognized in the GMA spectra (highlighted parts in yellow). However, no variation could be detected between the crosslinked and uncrosslinked Sil-MA films.

Is worth noting that, as observable from the GMA spectrum of **figure 4-2 A**, the absorbance of the GMA in the I Amide region is low, and in a first approximation negligible. For this reason, the evaluation of the secondary structures can be performed with the method of **paragraph 3.3.1**. The chemical modification influenced the protein secondary structure as can be seen from **Figure 4-2 C** as a result of the deconvolution of the primary amide peak (**Figure 4-2 B**). A slightly increase of the β parallel and antiparallel structures and a decrease of the amount of random coil and turn structures were detected after the methacrylation. Instead, after the UV exposure and the consequently crosslinking, the secondary structure remains the same. An interesting result appears from the comparison of the

secondary structures of the crosslinked methacrylated protein (rSF-MA) with a 12h water annealed fibroin (rSF-WA12h); the water annealing stabilizes the protein by the formation of β parallel and antiparallel structures at the expense of Random coil. The water annealed film resulted to be more crystalline than the crosslinked film.

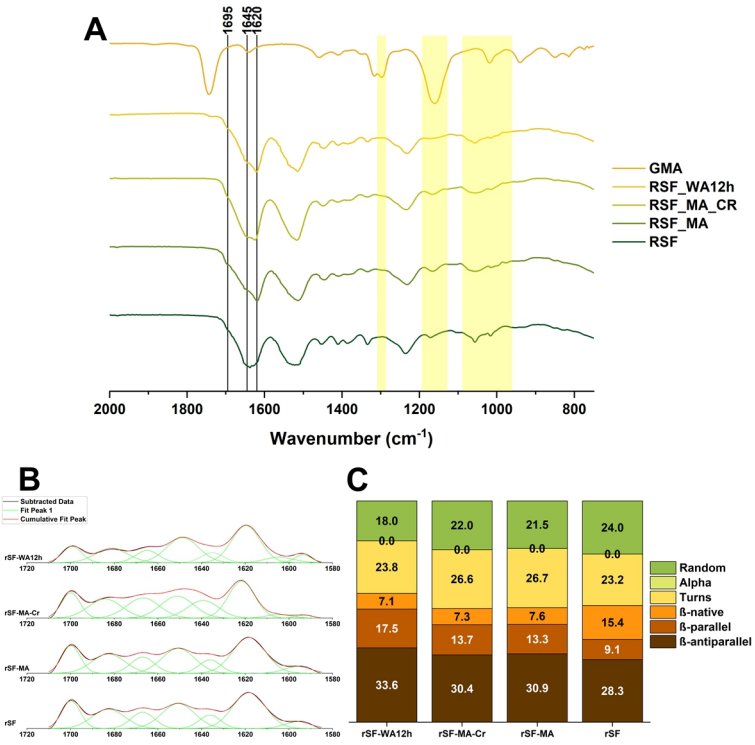

*Figure 4-2: (**A**) Comparison between the FTIR-ATR spectra of a regenerated fibroin(rSF), a methacrylate (rSF-MA) fibroin, a crosslinked methacrylated fibroin (rSF-MA-Cr), a water annealed fibroin rSF-WA12h) film. In addition, as reference we collected the GMA spectra from solution. Small variation the rSF-MA spectra due to*

*the presence of the functional group could be recognized at 1265 (CHOH stretching), 1165 (CH_2 wagging stretching) and 1015 cm^{-1} (out of plane CH stretching) can be reconducted to the presence of the functional groups (**B**) Gaussian fitting of the Fourier self-deconvolution (FSD) conducted on the primary amide peaks to determine the percentage of the different secondary structure. (**C**) Comparison in percentage between secondary structures.*

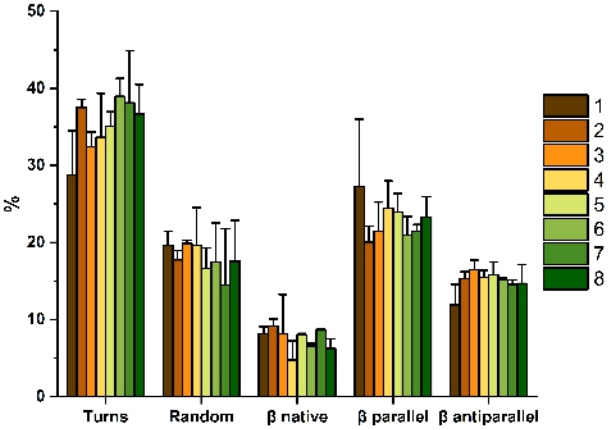

Figure 4-3: Secondary structure percentage composition of the 8 types of sponges, no statistical difference can be detected by ANOVA analysis between the single secondary structure components of the different compositions.

We analyzed the sponges' secondary structure of each of the 3 replicates of the 8 composition by deconvolution and fitting of the Amide I peak. The results were separated into groups each containing a specific secondary structure for all the 8 composition. An ANOVA test was then performed within each group to individuate if any significant difference in the

secondary structure due to the change in composition was detectable.

The data is presented in **Figure 4-3**: for each secondary structure there were no significant differences between their percentage level among the different compositions. This allows to state that the sponge composition had no appreciable effect on its secondary structure. As a consequence, it was not possible to build a model for the variation of the secondary structures. Indeed, the ANOVA performed in the DOE method to test the significance of the model gave a negative result.

4.2.2. Pore distribution and morphology

From the SEM micrography of **Figure 4-4 A** we could observe how the initial structure was stabilized, and, in fact, the original walls of the air bubble are clearly visible. In **Figure 4-4 B**, the interconnection between pores is clearly observable. In fact, several small pores are visible inside bigger pores (highlighted in blue). This kind of structure gives a sort "spherical" interconnected pores visible in the micrographies of **Figure 4-5 C**, with a wide distribution.

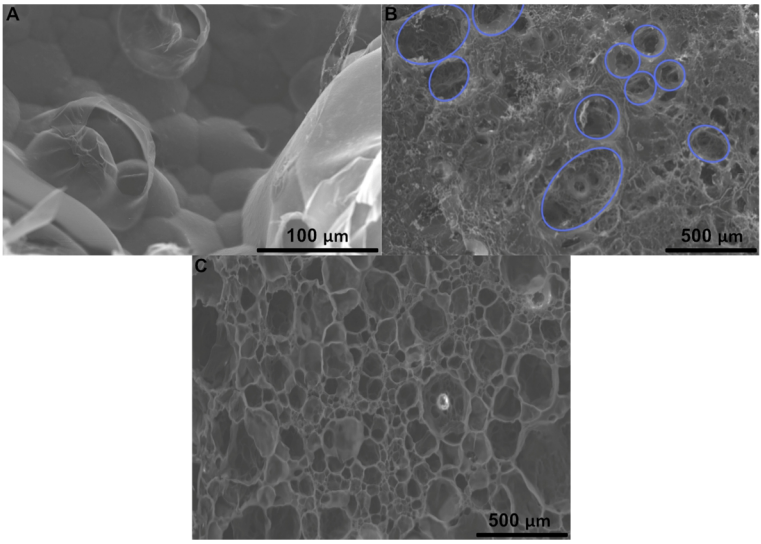

*Figure 4-4: SEM micrography of the sponge. (**A**)The bubbles structure produced by the mixer is clearly visible in the background. Some cut bubbles are present in the first plane. (**B**) Pores (highlighted in blue) where smaller inner pores are visible. (**C**) Cross-section of a chemically crosslinked sponge.*

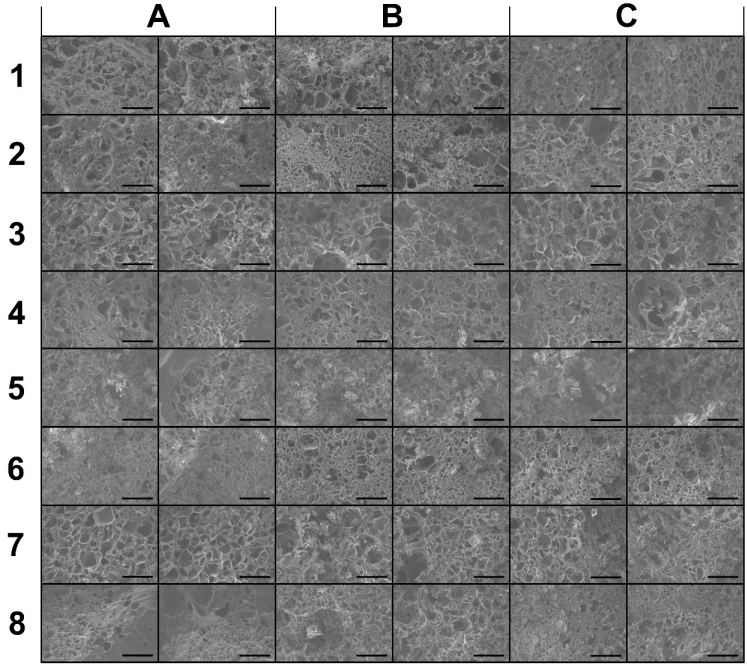

Figure 4-5: SEM micrographies for the porosity evaluation; for each sample 2 images at 60 X were captured, the scale bar represents a length of 500 µm. These images were used for the evaluation of the pore distribution, and subsequently the median pore area and the interquartile range.

The distribution of the pore area was evaluated by the analysis of 2 images per each sample (**Figure 4-5**). All the distribution resulted to be not normal and skewed to the left as shown in **Figure 4-6 A** and **B**, and, for this reason, we evaluated both the mean and the standard deviation, and the median and the interquartile range (IQR). The results are listed in **Table 4-1** and **Table 4-2**. Both the mean and the median were below 100

µm but considering the standard deviation and the interquartile range (IQR) we could deduce that a significant part of distributions was above 100 µm. The third interquartile and the maximum pore diameter gives a measurement of how spread out each distribution was: in all cases the former results to be higher than 79 µm and the latter higher than 150 µm. We modeled, as statistical parameters, the mean and the median pore area, the standard deviation and the interquartile range (IQR). All the models were significant (ANOVA tables from **table 2-6** to **table 2-8**).

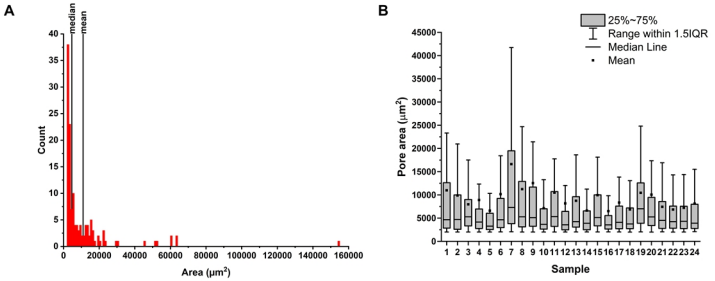

*Figure 4-6: (**A**) Pore distribution of the first sample, shows that the distribution is skewed, implying that the median and the mean are not in the same position. (**B**) The box-cox plot of samples pore distributions shows that all the distributions were skewed, so both the mean and the median were considered as a statistical measure of the porosity. 50% of the data points are concentrated inside the interquartile range represented by the box (IQR, 25%-75%) and the 80% inside the whiskers (90%-10%).*

N.	Mean Pore A µm²	Mean pore d µm	St.Dev A µm²	St.Dev d µm	Median pore A µm²	Median pore d µm	IQR A µm²	IQR d µm
1	9609	62	13075	72	4887	44	7615	55
2	8552	59	13638	74	4025	40	4666	43
3	13476	74	21890	94	5896	49	11301	67
4	8603	59	20179	89	4182	41	5278	46
5	8439	58	12043	70	4425	42	5754	48
6	7237	54	9772	63	3793	39	4083	40
7	9319	61	12311	70	5591	47	6845	52
8	7394	55	9006	60	4151	41	4924	45

Table 4-1: Mean pore area and its standard deviation (St.dev.), median pore area and associated interquartile range (IQR). All measurements are given in area and equivalent diameter. The standard deviation should be considered as a measure of the dispersion of the pore distribution and not as an uncertainty on the mean pore area. The mean pore diameter results to be under 100 µm but considering the standard deviation, a portion of the distribution is above that threshold. The median results to be below 50 µm but considering the IQR we can deduce that a consistent part of the distribution is above that value.

N.	1 QR A µm²	1 QR d µm	3 QR A µm²	3QR d µm	Max A µm²	Max d µm
1	2924	34	10539	89	98199	196
2	2752	33	7418	76	86922	187
3	3393	37	14694	104	168187	258
4	2780	34	8058	80	216504	284
5	2969	35	8723	77	93935	192
6	2694	33	6777	92	72541	169
7	3360	37	10206	89	111747	206
8	2783	34	7707	79	57052	150

Table 4-2: Quartile value and maximum pore size, given in area and equivalent diameter. The quartiles give a measure of how spread the pore size distribution is: half of the pores are between the first (1 QR) and the third (3QR); and, half of the measurement are in the outer region. Maximum diameters are between 150 and 300 µm, so part of the pore distributions (between the 3 QR and the Max) are in the correct range for cell attachment and grow.

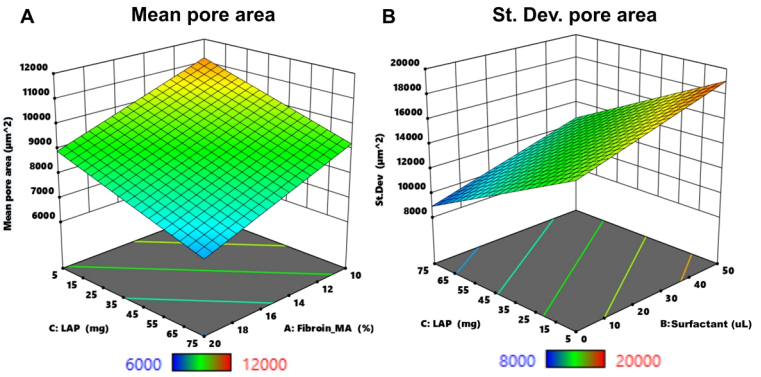

*Figure 4-7: (**A**) Modelled mean pore area trend (the scales are inverted for the sake of clarity). All the considered variables influenced the trend: the increasing of the surfactant volume, and the decreasing of both the solution concentration and the initiator tend to increase the mean pore area. (**B**) Modelled standard deviation (St. Dev.), in this case the trend was not influenced by the protein concentration. The St. Dev. increase with an increasing of the surfactant and a decreasing of the initiator.*

$$A_{mean} = 9078.77 - 1131.99 * A - 981.37 * B$$

$$A_{mean(CI\ 90\%\ Low)} = 8285.93 - 1924.82 * A - 1774.20 * B$$

$$A_{mean(CI\ 90\%\ High)} = 9871.60 - 339.16 * A - 188.54 * B$$

Source	Sum of Squares	Df	Mean Square	F-value	p-value	
Model	5.387E+07	2	2.693E+07	7.72	0.0031	**
A-Sil-MA Conc	3.075E+07	1	3.075E+07	8.82	0.0073	**
C-LAP Conc	2.311E+07	1	2.311E+07	6.63	0.0177	*
Residual	7.325E+07	21	3.488E+06			
Lack of Fit	2.658E+07	5	5.316E+06	1.82	0.1653	**not significant**
Pure Error	4.667E+07	16	2.917E+06			
Cor Total	1.271E+08	23				

Table 4-3 ANOVA table for the model (first equation on the top of the table) of the mean pore area. The significance level was assigned as follows: p≤0.1 (.), p≤0.05 (*), p≤0.01(**), p≤0.001(***). The significant terms in order of importance are: A- the concentration of the fibroin solution and C – the concentration of the photoinitiator (LAP). No higher order terms are present, so this implies that the model is linear.

From the ANOVA table (**Table 4-3**) we could assert that only two terms resulted to influence the mean. In order of importance: A – the concentration of the fibroin solution and C – the quantity of the photoinitiator (LAP). A decreasing of these terms results in an increasing of the mean pore area (**Figure 4-7 A**). Unexpectedly, the quantity of surfactant (term B) did not play a role in the mean pore area. Higher order terms resulted not significant, so the model could be considered linear.

$$St.DEV = 13989.23 + 1857.23 * B - 3206.15 * C$$

$$St.DEV_{(CI\ 90\%\ Low)} = 11856.80 - 257.20 * B - 5338.58 * B$$

$$St.DEV_{(CI\ 90\%\ High)} = 16121.66 - 3989.66 * B - 1073.72 * C$$

Source	Sum of Squares	df	Mean Square	F-value	p-value	
Model	3.295E+08	2	1.647E+08	6.53	0.0062	**
B-Surfactant	8.278E+07	1	8.278E+07	3.28	0.0844	.
C-LAP Conc	2.467E+08	1	2.467E+08	9.78	0.0051	**
Residual	5.299E+08	21	2.523E+07			
Lack of Fit	1.232E+08	5	2.465E+07	0.9697	0.4653	**not significant**
Pure Error	4.067E+08	16	2.542E+07			
Cor Total	8.594E+08	23				

Table 4-4: ANOVA table for the model of the standard deviation of the pore area distribution. The significance level was assigned as follows: p≤0.1 (.), p≤0.05 (*), p≤0.01(**), p≤0.001(***). The significant terms in order of importance are: C – the concentration of the photoinitiator (LAP) and B- the quantity of surfactant. No higher order terms are present, this imply that the model is linear.

The standard deviation, as can be seen in its ANOVA table (**Table 4-4**), is instead influenced by the amount of surfactant (term B) as well as the quantity of photoinitiator (term C): the increasing of the former and a decreasing of the latter ensured a higher standard deviation, resulting in a broader distribution (**Figure 4-7 B**).

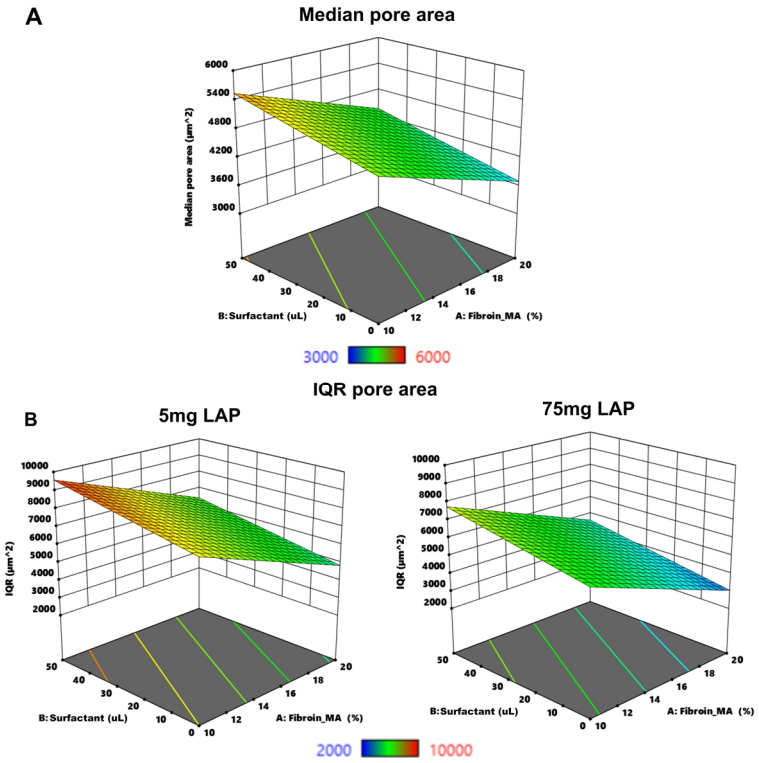

*Figure 4-8: (**A**) Modelled median pore area: in this case only the protein and the initiator concentration have an influence. An increasing of the area could be detected with an increasing of both factors. (**B**) Modelled interquartile range (IQR): all the three factors influence the trend. The IQR increases with the decrease of the protein concentration, the increase of the surfactant and the decrease of the initiator.*

$A_{median} = 4618.72 - 580.97 * A + 336.27 * B$

$A_{median(CI\ 90\%\ Low)} = 4296.90 - 902.79 * A + 14.46 * B$

$A_{median(CI\ 90\%\ High)} = 4940.54 - 259.16 * A + 658.09 * B$

Source	Sum of Squares	df	Mean Square	F-value	p-value	
Model	1.081E+07	2	5.407E+06	9.41	0.0012	**
A-Sil-MA Conc	8.101E+06	1	8.101E+06	14.09	0.0012	**
B-Surfactant	2.714E+06	1	2.714E+06	4.72	0.0414	*
Residual	1.207E+07	21	5.747E+05			
Lack of Fit	1.576E+06	5	3.153E+05	0.4807	0.7855	**not significant**
Pure Error	1.049E+07	16	6.558E+05			
Cor Total	2.288E+07	23				

Table 4-5: ANOVA table for the model (first equation on the top of the table) of the median pore area. The significance level was assigned as follows: p≤0.1 (.), p≤0.05 (*), p≤0.01(**), p≤0.001(***). The significant term in order of importance are: A- the concentration of the fibroin solution and B –the quantity of surfactant. No higher order terms are present, this imply that the model is linear.

The median pore area, from its ANOVA table (**Table 4-5**), resulted to be influenced by A – the Sil-MA concentration and B – the quantity of surfactant. A decreasing of the first term and an increasing of the second gave an increment in the mean pore area (**Figure 4-8 A**).

The interquartile range was influenced by all the three considered factors (**Table 4-6**): a decreasing in A – the concentration of fibroin in solution, an increasing of B – the

quantity of surfactant and C – the quantity of photoinitiator gave an increase in the IQR (**Figure 4-8 B**).

$$IQR = 6308.15 - 1570.57 * A + 778.59 * B - 906.77 * C$$

$$IQR_{(CI\ 90\%\ Low)} = 5447.98 - 2430.74 * A - 81.58 * B - 1766.94 * C$$

$$IQR_{(CI\ 90\%\ High)} = 7168.32 - 710.40 * A + 1638.76 * B - 46.60 * C$$

Source	Sum of Squares	df	Mean Square	F-value	p-value	
Model	9.348E+07	3	3.116E+07	7.64	0.0014	**
A-Silk_MA Conc	5.920E+07	1	5.920E+07	14.51	0.0011	**
B-Surfactant	1.455E+07	1	1.455E+07	3.57	0.0736	.
C-LAP Conc	1.973E+07	1	1.973E+07	4.84	0.0398	*
Residual	8.162E+07	20	4.081E+06			
Lack of Fit	2.008E+07	4	5.021E+06	1.31	0.3099	**not significant**
Pure Error	6.154E+07	16	3.846E+06			
Cor Total	1.751E+08	23				

Table 4-6: ANOVA table for the model (first equation on the top of the table) of the interquartile range (IRQ) of the pore area distribution. The significance level was assigned as follows: p≤0.1 (.), p≤0.05 (*), p≤ 0.01(**), p≤0.001(***). The significant terms in order of importance are: A - the concentration of the fibroin solution, C – the quantity of photoinitiator and B – the quantity of surfactant. No higher order terms are present, this imply that the model is linear.

4.2.3. Dissolution test and water absorption

The dissolution in SBF and the water absorption are reported in **Figure 4-9 A** and **B** as percentage of the initial weight of the sponge. The dissolution at day 1 is dramatically

different for samples with different compositions; in particular we could recognize the effect of the quantity of photoinitiator (sample 1-4 versus samples 5-8) and, with a minor contribution, the effect of the amount of the surfactant (sample 1-2 versus sample 3-4). These differences remain stable throughout the experimental time.

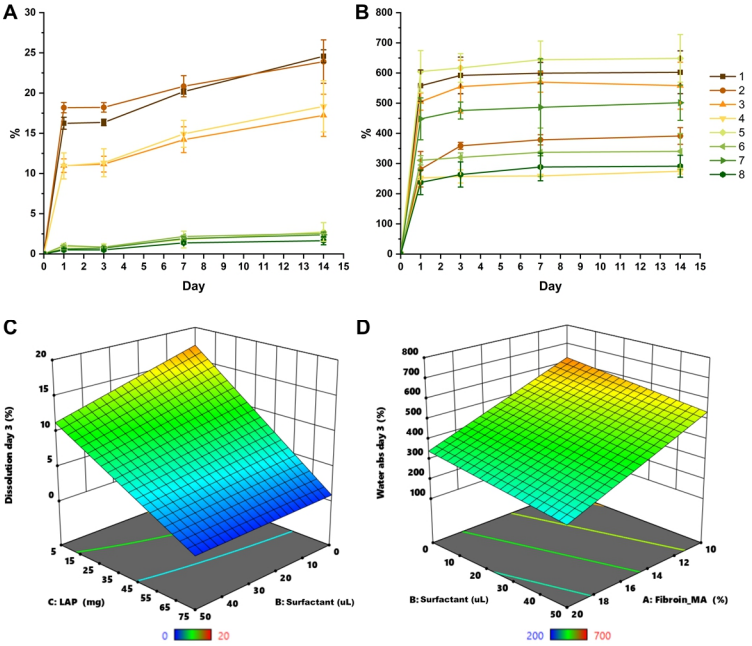

*Figure 4-9: (**A**) Dissolution test in simulated body fluid (SBF). A striking effect can be observed passing from 5 mg (samples 1-4) to 75 mg (samples 5-8) of photoinitiator, a second difference can be observed between the sample 1-2 and 3-4 and this is related to the presence of the surfactant. (**B**) Water absorption. In this case a difference can be seen between the samples 1-3-5-7 and the samples 2-4-6-8, this is due to the concentration of the initial solution that pass from 10 to 20%. (**C**) Modelled dissolution at day 3, the decrease of the quantity of surfactant and the quantity of photoinitiator increase the percentage of*

*dissolved fibroin. (**D**) Modelled water absorption at day 3, the decrease of the protein concentration and quantity of surfactant increase the amount of adsorbed water.*

The effect of the photoinitiator and the surfactant resulted to be significant also from an ANOVA analysis (**Table 4-7**). Interestingly the model resulted to be non-linear because of the significance of the second order term B*C. The model showed that a decrease of the quantity of surfactant and photoinitiator gives an increase in the amount of dissolved fibroin. The amount of photoinitiator influences the degree of crosslinking and consequently the sponge stability. Thus, a lower amount of LAP gives a higher amount of solubilized sponge. Instead, the lower amount of the surfactant gives a lower dispersion of the pore distribution that could be related to the higher stability.

$$m_{SF} = 7.53 - 1.55 * B - 6.78 * C + 1.43 * B * C$$

$$m_{SF_{(CI\ 90\%\ Low)}} = 7.11 - 1.97 * B - 7.20 * C + 1.01 * B * C$$

$$m_{SF_{(CI\ 90\%\ High)}} = 7.95 - 1.13 * B - 6.36 * C + 1.85 * B * C$$

Source	Sum of Squares	df	Mean Square	F-value	p-value	
Model	1209.58	3	403.19	414.25	< 0.0001	***
B-Surfactant	57.82	1	57.82	59.41	< 0.0001	***
C-LAP Conc	1102.94	1	1102.94	1133.18	< 0.0001	***
BC	48.82	1	48.82	50.16	< 0.0001	***
Residual	19.47	20	0.9733			
Lack of Fit	5.45	4	1.36	1.56	0.2337	**not significant**
Pure Error	14.01	16	0.8758			
Cor Total	1229.05	23				

*Table 4-7: ANOVA table for the model (first equation on the top of the table) of the dissolution in SBF at day 3. The significance level was assigned as follows: p≤0.1 (.), p≤0.05 (*), p≤0.01(**), p≤0.001(***). The significant terms are all equal in term of importance: B – the quantity of surfactant and C – the quantity of photoinitiator. Interestingly, in this case a higher order term is present B*C, the model is, therefore, not linear. The model is significant, and the lack of fit is not significant, indicating that the model correctly fit the data.*

The only clear effect visible from the water absorption is due to the protein concentration in solution (**Figure 4-9 B** sample 1, 3, 5, 7 versus sample 2, 4, 6, 8). Interestingly, the ANOVA table for the water absorption at day 3 (**Table 4-8**) revealed the significant effect of the volume of surfactant.

$$m_{H_2O} = 440.43 - 141.63 * A - 44.53 * B$$

$$m_{H_2O_{(CI\ 90\%\ Low)}} = 414.05 - 168.01 * A - 70.91 * B$$

$$m_{H_2O_{(CI\ 90\%\ High)}} = 466.81 - 115.24 * A - 18.15 * B$$

Source	Sum of Squares	df	Mean Square	F-value	p-value	
Model	5.290E+05	2	2.645E+05	68.47	**< 0.0001**	***
A-Silk_MA Conc	4.814E+05	1	4.814E+05	124.62	**< 0.0001**	***
B-Surfactant	47592.16	1	47592.16	12.32	**0.0021**	**
Residual	81123.55	21	3863.03			
Lack of Fit	12645.62	5	2529.12	0.5909	**0.7072**	**not significant**
Pure Error	68477.93	16	4279.87			
Cor Total	6.101E+05	23				

Table 4-8: ANOVA table for the model (first equation on the top of the table) of the water absorbance at day 3. The significance level was assigned as follows: p≤0.1 (.), p≤0.05 (*), p≤0.01(**), p≤0.001(***). The significant term in order of importance are: A - the concentration of the fibroin solution and B – the quantity of surfactant. No higher order terms are present, this imply that the model is linear. The model is significant, and the lack of fit is not significant indicating that the model correctly fit the data.

The model is shown in **Figure 2-9 D**: the decrease of the protein concentration and of the quantity of surfactant increase the amount of adsorbed water. Since the median pore area goes the same direction, we could assert that a decrease in the area of the pores (in the lower region of the dispersion) could result in a higher amount of adsorbed water. The data were model only for the day 3 because, as stated before the effect of the composition on the dissolution and water

absorption is visible from day 1; then even though there are small variations, the mutual differences between the data of different compositions remains constant throughout the duration of the experiment.

4.2.4. Preliminary in vitro evaluation

The MTT assay was performed to evaluate the cell viability: in **Figure 4-10 A** the viability in percentage of the control sample is reported. The ANOVA test made against the control showed a significant difference from samples 5, 7 and 8. This is related to the effect of the initiator that, even though it is widely used in material with biological application[14,171–173], could be toxic at high concentration. This became clear by using the collected data in combination with the DOE method. In fact, from the ANOVA **Table 4-9** the main effect on the cell viability is due to the factor C – the quantity of photoinitiator. Unexpectedly, the second order mixed term A*B resulted to be significant, so also the single terms A and B were included to maintain the model hierarchy.

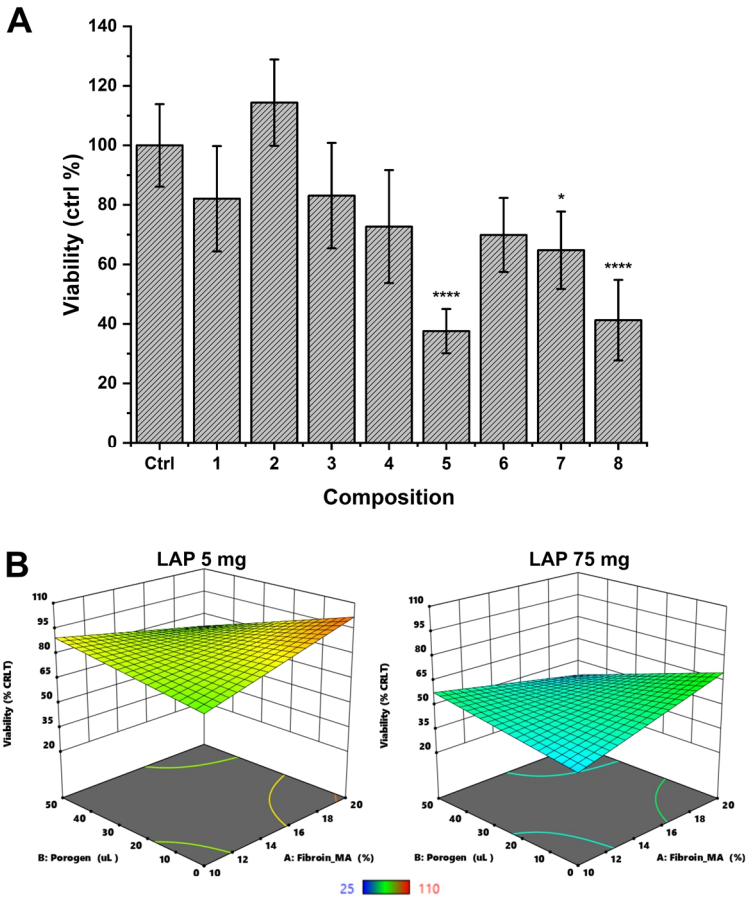

*Figure 4-10: MTT assay response. (**A**) The cell viability was evaluated as percentage of the positive control, an ANOVA test was conducted to evaluate the significance versus the control: samples 5, 7 and 8 results to have a significantly lower viability. This effect is clearly due to the higher amount of LAP as shown in figure (**B**) where the modelled response is shown. Passing from 5 to 75 mg of LAP the model pass from around 97 to 62 % of cell viability. The response is not linear due to the significance of the term A*B – Sil-MA concentration * quantity of surfactant.*

$$V_{\%} = 69.00 + 2.29 * A - 3.86 * B - 15.81 * C - 10.93 * A * B$$

$$V_{\%_{(CI\ 90\%\ Low)}} = 61.39 - 5.31 * A - 11.47 * B - 23.42 * C - 18.54 * A * B$$

$$V_{\%_{(CI\ 90\%\ High)}} = 76.60 + 9.90 * A + 3.75 * B - 8.21 * C - 3.33 * A * B$$

Source	Sum of Squares	df	Mean Square	F-value	p-value	
Model	0.9562	4	0.2390	7.38	0.0009	***
A-Fibroin -MA Conc	0.0129	1	0.0129	0.3987	0.5353	
B-Surfactant	0.0365	1	0.0365	1.13	0.3016	
C-LAP Conc	0.6135	1	0.6135	18.93	0.0003	***
AB	0.2932	1	0.2932	9.05	0.0072	**
Residual	0.6157	19	0.0324			
Lack of Fit	0.0514	3	0.0171	0.4855	0.6971	**not significant**
Pure Error	0.5643	16	0.0353			
Cor Total	1.57	23				

*Table 4-9: ANOVA table for the model (first equation on the top of the table) of the cell viability at day 3. The significance level was assigned as follows: p≤0.1 (.), p≤0.05 (*), p≤0.01(**), p≤0.001(***). As we deduced C – the amount of photoinitiator is the most significant parameter. Surprisingly a second order effect could be detected the A*B – Sil-MA concentration * quantity of surfactant is significant. This effect can be seen in the curvature of the plotter model of **figure 10 B**.*

The effect of A*B is clearly visible in the curvature present in the model (**Figure 4-10 B**): A*B is negative so, even if the concentration of protein is not relevant, due to this mixed term the viability is maximized at higher protein concentration and lower quantity of surfactant. Another maximum, but with a lower viability, is obtained when the surfactant is in its high level and the concentration of silk at its low level. The response

surface undergoes a negative translation when the LAP quantity increases from 5 to 75 mg, confirming the cytotoxicity of LAP when used in high concentration.

4.3. Discussion

Sponge properties resulted to be composition dependent. In case of Sil-MA the porosity and the compressive modulus on hydrogel were studied and resulted to be influenced by the concentration of protein in solution and the amount of GMA used in the modification reaction[14]. In our study, we confirmed the dependence of the mean pore area on the concentration of protein in solution, but we also proved its dependence on the amount of photoinitiator (LAP). We studied the standard deviation as the statistical parameter of the range of the mean pore area distribution. This parameter resulted to be influenced by the amount of surfactant (Tween20) and LAP. The surfactant effect could be explained by considering the amphiphilic nature of its molecules, that allows an effective stabilization of the air-liquid interface[174–177], and possibly, the formation of bigger bubbles. An increase in the amount of LAP decreased the standard deviation. This could be related to the higher number

of radicals produced thus the faster crosslinking[178] and the impossibility for the structure to partially collapse leaving bigger holes.

The stability of the sponge in simulated body fluid was mainly controlled by the photoinitiator concentration that, influencing the degree of crosslinking[179], could modulates the chemical resistance. The effect of the surfactant amount was also significant, in this case the wider distribution of pore area due to an increase in the volume of Tween 20 could probably explain the lower stability of the sponge due to the higher permeability to the SBF[180,181].

In the preliminary *in vitro* test, the cell viability was primarily dependent on the amount of photoinitiator. Even if this photoinitiator has been widely used for scaffold fabrication[14,171,179,182,183] it resulted to be, in our experiment , cytotoxic if used in high concentration. This discrepancy is probably due to the low concentration generally adopted in literature[14,171,179,182,183] (between 0.1 and 1 %) which is much lower than the concentration used in the high level of our experiment (15 %). The cell viability resulted to be influenced

also by a second order mixed term: the surfactant volume and the amount of photoinitiator resulted to be interacting factors. Considering the fact that the absence of cytotoxicity is a prerequisite for a scaffold, the amount of photoinitiator is the limiting factor of our protocol. In fact, as reported above, the low amount of photoinitiator required for high mean pore area, wide pore distribution and low cytotoxicity, is not compatible with a limited degradation of the scaffold in SBF.

4.4. Conclusion

Silk fibroin sponges are a widely studied material used as scaffold in tissue engineering both for bones and for soft tissues. Among their properties porosity and stability are the most important ones. An open porosity with a wide distribution of diameters ensures an optimal cells attachment and growth while the stability in a simulated body fluid allows enough time to regenerate the tissue prior to the scaffold degradation. Both properties should be tunable to fit the requirement of the natural tissue. In this work we were able to optimize a methodology to obtain a sponge from a methacrylated fibroin (Sil-MA) solution with tunable porosity and stability.

The effect of the sponge composition on the secondary structure, the porosity distribution, the water absorption, the stability in SBF, and the cell viability was studied with a full factorial design of experiment (DOE). Using this method, we were able to model the significant parameters for each properties of interest. For instance, the amount of photoinitiator and the concentration of Sil-MA solution both resulted to affect the mean pore area. The increase of these parameters decreases the mean pore area. The standard deviation of the mean pore area, directly related to the range of the distribution, resulted to be affected by the amount of photoinitiator and the volume of surfactant. In this case, the increase of the former decreases the standard deviation while an increase of the latter had the opposite effect. The stability of the sponge resulted to improve with the increasing of the amount of photoinitiator; on the other hand, the cell viability resulted to be lower. Interestingly, some second order terms, not detectable using the conventional “one variable versus one response” method, resulted to be significant.

The main limitation of our protocol is the impossibility to conjugate a high stability in SBF with the optimal material

proprieties parameters needed for a scaffold (low cytotoxicity, high mean pore area with a wide pore distribution). However, this limitation could be addressed in the future by considering as parameter the energy absorbed from the sample during the UV exposure. This energy is usually tuned by changing the exposure time. The porosity as reported in the literature, in good agreement with our results, is dependent on the concentration of the solution. A more extensive DOE taking into consideration other process parameters could result beneficial in achieving an optimal compromise.

5. Low temperature, high pressure sintered fibroin

Part of this chapter has been published in:

A Thermal-Reflow-Based Low-Temperature, High-Pressure Sintering of Lyophilized Silk Fibroin for the Fast Fabrication of Biosubstrates

Alessio Bucciarelli, Silvia Chiera, Alberto Quaranta, Vamsi K. Yadavalli, Antonella Motta, Devid Maniglio
Adv. Funct. Mater., **2019**, 1901134, 1-13

5.1. Introduction

Solid-fibroin is a bulk, non-porous material produced from silk cocoons. For its aspect it can resemble a hard-plastic but with mechanical properties that are in an intermediate position between a plastic and a glass. In fact, solid fibroin has an extremely low glass transition temperature (around 60 °C) and above it the material is easily deformable. However, under the glass transition, it has extremely high compressive and tensile modulus. The mild preparation condition and the facile embedding of biomolecules, can serve as a platform to implement different functions into a mechanical stable

material[15]. Thanks to this fact, recently solid-fibroin has been adopted in surgery for cranial fixation[28].

The protocol to prepare fibroin bulk material is based on the slow transition of the regenerated silk fibroin solution to the gel and then to the solid state through solvent evaporation (*solid-fibroin by casting*). The sol-gel-solid transition is triggered by nucleation and aggregation phenomena that are generally slow [69,184], taking from several weeks in case of water solution to several days in case hexafluoroisopropanol solution. The long time needed to fully evaporate the solvent and the large shrinkage of the monoliths during the transitions constitute two limiting factors for large-size objects and large-scale production. In order to overcome these limitations, the use of an alternative method is desirable.

A possible approach, already proposed in a few works in literature, is a sintering procedure where starting from fibroin powder a solid material is obtainable in few minutes by compression into a hot mold[16–18]. While in the conventional sintering approach the temperature to achieve the full compaction of dry fibroin powder has been reported to be in a range between 150 and 200 °C[17,18], introducing a pulsatile

electric potential (pulse-energizing sintering) and wetting the fibroin powder, the temperature could be decreased down to 100 °C[16]. However even 100 °C is too high to allow the incorporation of thermally degradable molecules, such as drugs or enzymes[185].

In this chapter, we present an improvement of the previous methods, a high-pressure, low-temperature sintering that allows to obtain solid-fibroin (*solid-fibroin by sintering*) at 40 °C in few minutes. In addition, we hypothesize a possible mechanism for this solid-solid transition occurring during the sintering since in literature this transition is not fully explained yet. It was supposed that two factors may play an important role: the glass transition temperature (T_g) and the secondary structure[16,17].

It is reported that at a process temperature higher than T_g a significant molecular interdiffusion (thermal-reflow) can occur[186–188]. In this phenomenon, the addition of water, acting as plasticizer, leads to a decreasing in the glass transition temperature (T_g)[186–188] and, consequently, of the energy needed to activate the thermal-reflow[140]. On wet fibroin films, this principle has been used to imprint microstructures[95] and

hydrolyzable metal microstructure using a hot mold[94], to produce laminates of staked films by compression[97], and, more recently, to produce a fibroin device with programmable degradation time[189]. Even if the T_g of fibroin is reported to decrease down to 40 °C in some conditions, none of the above processes report the use of a such low temperature. On the contrary, to activate thermal-reflow, silk fibroin films are usually treated at 120÷140 °C.

Pressure (application of stress), temperature and water content can also influence the secondary structures inducing the transition to a higher stability crystalline phase[51,70,188]. In the case of sintering processes the use of intrinsically crystalline fibroin powder leads to the necessity to increase temperature up to 200 °C to obtain satisfactory thermal reflow [16,190,191].

We propose, as an improvement of the sintering processes, the use of lyophilized silk fibroin with a low crystallinity in combination with the fast addition of water by moisture adsorption. The fast addition of water permits the decrease of T_g, plasticizing the powder without inducing a high degree of crystallization before compression, thus activating the

thermal-reflow even at a low temperature (40°C) and the consequent solid-solid transition during compression.

Using Fourier transform infrared spectroscopy (FTIR) and digital scanning calorimetry (DSC), the variation of the protein secondary structures and the T_g was observed throughout the process in order to study the solid-solid transition process at a molecular level. We proved that this transition can occur even if the T_g of the initial material is higher than the temperature used in the compression phase. The reduction of the glass transition temperature due to the compression effect on the moisturized material was deduced by SEM microstructural analysis through which the thermal-reflow in the material, as a function of the compression time, was observed.

To determine the parameters influencing the process and their optimum value a design of experiments (DOE) based on two yields has been adopted: the material's transparency and the compressive Young modulus. Compression tests were performed in both dry and wet samples. Finally, to study the potential role of LTS fibroin samples in biomedical applications, we preliminary evaluated their effect on *in vitro* cell culture.

Human adipose-derived mesenchymal stem cells (AdMSCs) were cultured on the samples in static condition and their adhesion and proliferation were studied by confocal analysis.

5.2. Results

The study of the production of a solid material from regenerated silk fibroin using a fast and cold compression is important to provide a suitable method for the development of a new generation of biomaterials. Understanding how the process parameters influence the final material and in which direction the solid-solid transition occurs gives useful insight on the process and allows to determine the optimal procedure to form a fully sintered object.

To this purpose, a screening was done using a 2^4 full factorial design of experiment (DOE). Each variable is unambiguously associated to a factor as reported in **table 3-1**: from here on the term “factor” will be used interchangeably with “variables”. To follow the process an optical and a mechanical measurement has been selected: the former allows to follow the fibroin transition from a white reflective to a transparent

material, the latter from soft to hard. The overall results of the analysis are listed in **Table 3-3**, where the 16 samples are listed with their associated yields.

	Factors				Yields	
	A	B	C	D		
Std. Order	Ramp time [s]	Max Pressure [MPa]	Maint. time [s]	Added water %	UV-Vis normalized area	E [MPa]
1	120	200	0	0	527.9	484
2	600	200	0	0	479.9	524
3	120	400	0	0	503.3	538
4	600	400	0	0	515.7	690
5	120	200	1200	0	521.6	560
6	600	200	1200	0	434.2	589
7	120	400	1200	0	444.4	589
8	600	400	1200	0	350.6	632
9	120	200	0	20	407.3	509
10	600	200	0	20	253.7	420
11	120	400	0	20	209.2	1400
12	600	400	0	20	270.8	697
13	120	200	1200	20	296.0	729
14	600	200	1200	20	296.0	633
15	120	400	1200	20	106.1	1285
16	600	400	1200	20	334.5	487

Table 5-1: Design of experiment table of the sintering process, four factors and two levels for each of them were evaluated for a total of 16 samples. Two yields were used for the data analysis: the normalized area under the visible part of the UV-Vis spectrum, and the Young modulus obtained with a compression test. Both values help to predict the direction in which the sintering process occurs.

5.2.1. Process optimization: optical method

An optimal transformation of the silk fiber powder into a solid compact material by compression molding implies the turning of a shiny, white, solid into a compact yellowish, partially transparent material. This change in the optical behaviour of the material can be used to evaluate the quantity of sintered material. In particular, the area of the absorbance spectra in the visible region (400 ÷ 700 nm) is related to the presence of inhomogeneities in the structure. Therefore, the lower the area of the absorbance spectrum, the higher the amount of fibroin that has undergone the transition. Based on the results obtained from the UV-VIS spectra (**Figures 5-1, 5-2, 5-3, 5-4**) an empirical predictive model was built. This model (equation in **Table 5-2**) reports the value of the area under the spectra (in the visible range) as a function of the considered factors.

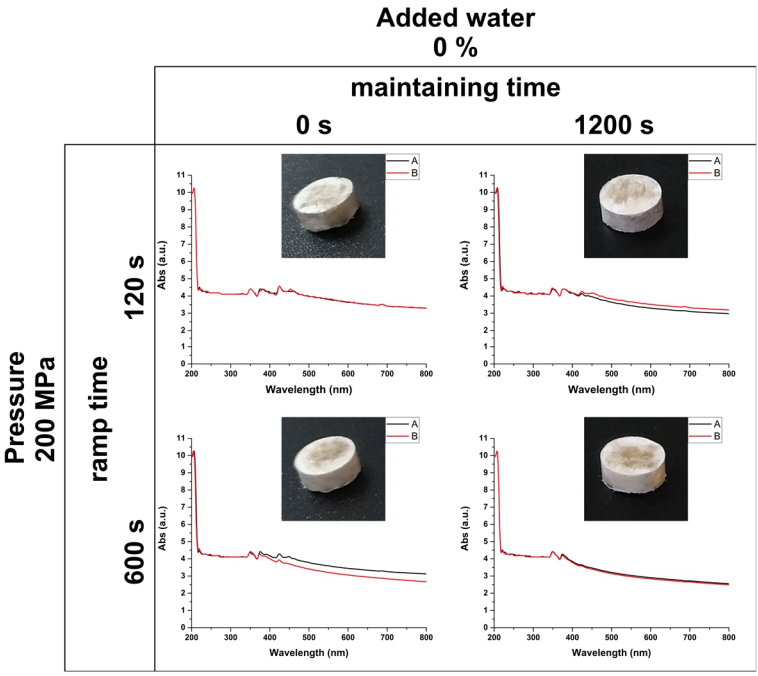

Figure 5-1: UV-VIS absorbance spectra of the 4 samples prepared without addition of water and with a maximum pressure of 200 MPa.

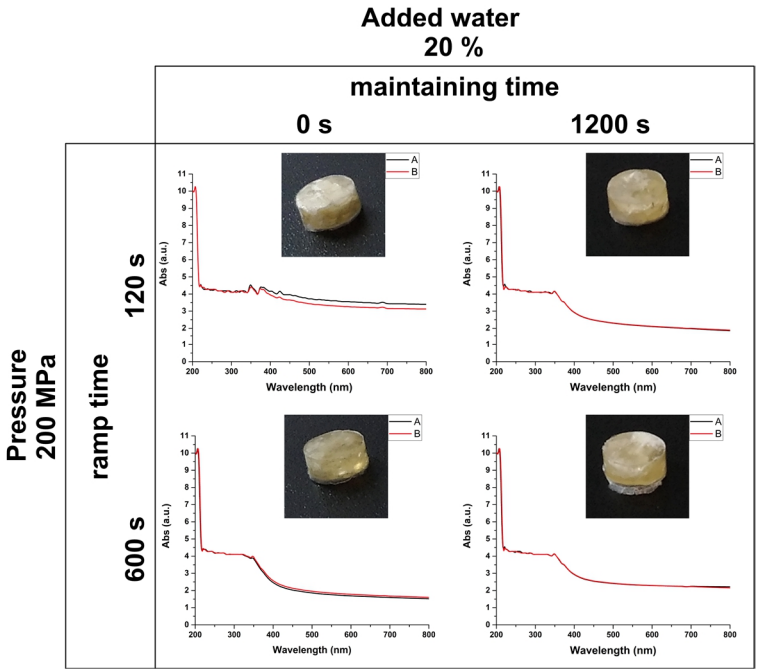

Figure 5-2: UV-VIS absorbance spectra of the 4 samples prepared with the addition of a 20% of water and with a maximum pressure of 200 MPa.

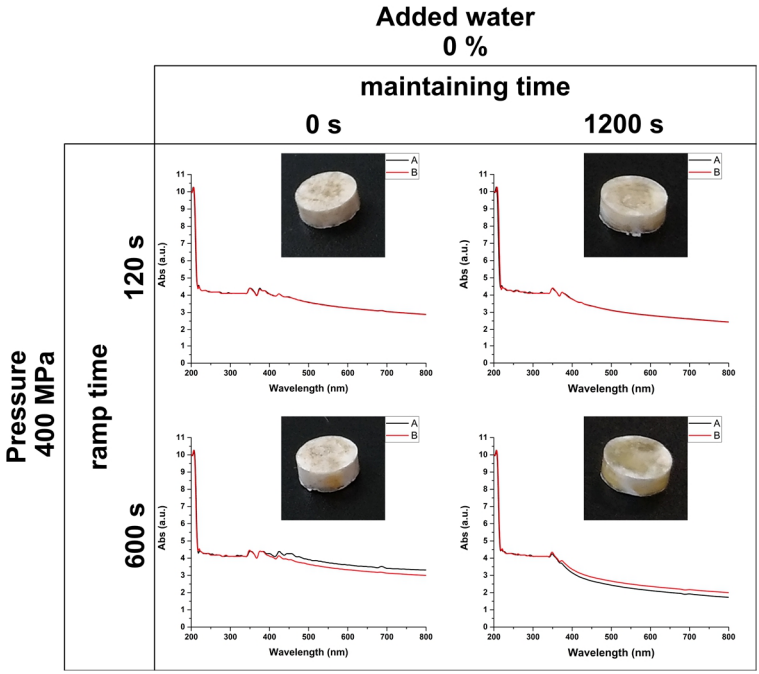

Figure 5-3: UV-VIS absorbance spectra of the 4 samples prepared without the addition of water and with a maximum pressure of 400 MPa.

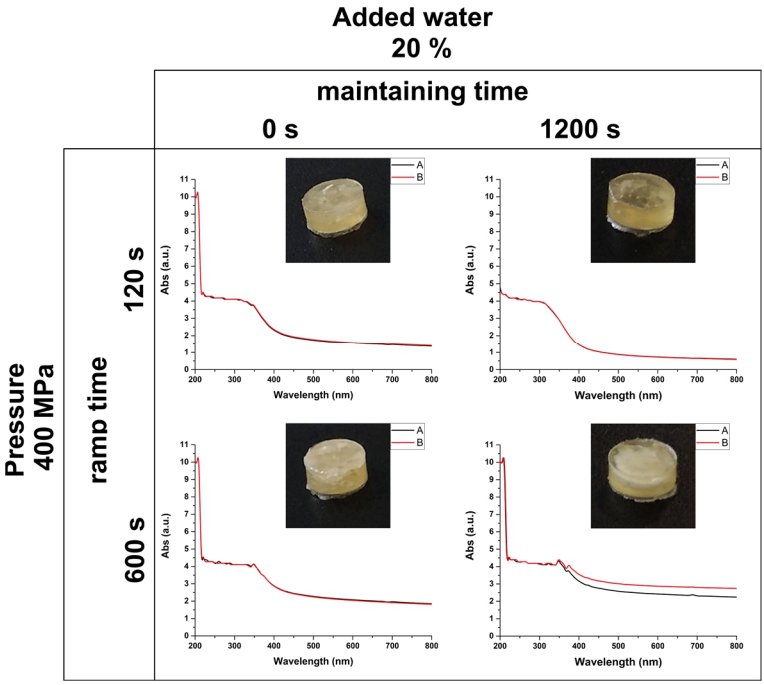

Figure 5-4: UV-VIS absorbance spectra of the 4 samples prepared with the addition of 20% of water and with a maximum pressure of 400 MPa.

Based on this model, the analysis of variance (ANOVA) was done to evaluate its significance and the significance of the terms included. The ANOVA test (**Table 5-2**) shows that the built model is significant, so it can be used to predict the trend of the yield. The results of our predictive model are shown in **Figure 5-5** as surface plot. The lower area is obtained for a 120 s ramp time, a maximum pressure of 400 MPa, a maintenance time of 1200 s, and in presence of 20% of water.

The addition of water ensures better results with a VIS area in the range of 150-400 nm, instead, in absence of water the range increases to 400-560 nm. This can be also noticed by a simple comparison between the samples presented in **Figures 5-1, 5-3** with those in **Figures 5-2, 5-4** which shows that the quantity of lyophilized white fibroin dramatically decreases passing from 0 to 20 % of added water.

It is worth noting that in presence of water the absorbance spectrum area decreases with the decreasing of the ramp time. We can explain this phenomenon considering that, since the transition to solid is promoted by the presence of water, a high compression rate forces the water to diffuse into the spongy lyophilized fibroin, prior to the transition to the solid phase, allowing a more homogenous compaction of the structure. Instead, a low compression rate induces the transition on the surfaces first (probably starting where the percentage of adsorbed water is higher) preventing the transition of the core.

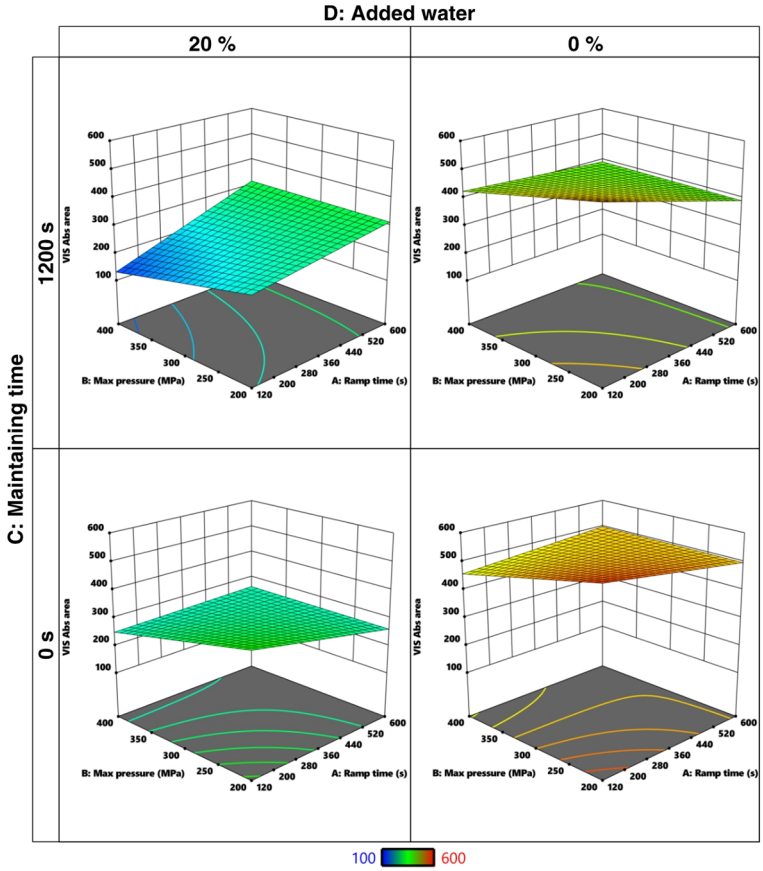

Figure 5-5: Surface plots based on the empirical model that report the trend of the area under the visible part of the absorbance spectrum (400÷780 nm) versus the considered variables. This allows to establish the optimal process conditions. In this case the lower area can be obtained with a low ramp time (t_{ramp}=120 s), a high pressure (P_{max}=400 MPa), a high maintenance time (t_{maint}=1200 s), and with the presence of added water ($m_{w\%}$= 20 %).

In absence of adsorbed water, the absorbance area decreases with the increasing of the ramp time: the transition occurs in all the material and probably it starts where the local

presence of water is higher giving, as a result, a material in which the solid and the lyophilized phases are mixed together in a continuous fashion. In this case, a higher amount of time allows the transition of a higher amount of material.

$$A_{Abs} = 370.47 - 3.53 * A - 28.63 * B - 25.53 * C - 101.74 * D + 29.59 * A * B + 12.24 * A * C + 23.58 * A * D + 8.99 * C * D + 30.62 * A * C * D$$

$$A_{Abs(95\%\ CI\ Low)} = 340.35 - 33.65 * A - 58.76 * B - 55.65 * C - 131.87 * D - 0.53 * A * B - 17.70 * A * C - 6.54 * A * D - 21.14 * C * D + 0.49 * A * C * D$$

$$A_{Abs(95\%\ CI\ High)} = 400.60 - 26.60 * A - 1.49 * B - 4.59 * C - 71.62 * D + 59.72 * A * B + 42.55 * A * C + 53.70 * A * D + 39.11 * C * D + 60.74 * A * C * D$$

Source	Sum of Squares	Df	Mean Square	F-value	p-value	
Model	2.310E+05	9	25671.39	10.59	0.0048	**
A-Ramp time	198.81	1	198.81	0.0820	0.7843	
B-Max pressure	13118.66	1	13118.66	5.41	0.0590	.
C-Maintaining time	10428.68	1	10428.68	4.30	0.0834	.
D-Water addition	1.656E+05	1	1.656E+05	68.30	0.0002	***
AB	14011.68	1	14011.68	5.78	0.0530	.
AC	2469.69	1	2469.69	1.02	0.3518	
AD	8895.27	1	8895.27	3.67	0.1039	
CD	1291.97	1	1291.97	0.5328	0.4929	
ACD	14996.84	1	14996.84	6.18	0.0474	*
Residual	14549.27	6	2424.88			
Cor Total	2.456E+05	15				

Table 5-2: ANOVA table for the model (first equation on the top of the table) of the area of the absorbance spectra in the visible range. The significance level was assigned as follows: p≤0.1 (.), p≤0.05 (*), p≤0.01(**), p≤0.001(***). The model results to be significant with a p-value below 0.005. This implies that this model can be used to predict the area and then the direction in with the solid-solid transition occurs. The significant term in order of importance are: D - water addition,

*A*C*D - ramp time*maintaining time*water content, A*B–ramp time*max pressure, B – max pressure, C – maintaining time. The other terms are added to preserve the model hierarchy. Equations of the 95% confidence intervals (CI) are reported after the model equation.*

The effect of the maximum applied pressure is, instead, independent from the water presence but related to the ramp time: the absorbance area decreases with the increase of the maximum applied pressure, but the amount of this decrease depends on the ramp time.

Both the higher order mixed terms t_{ramp}*P_{max} and t_{ramp}*t_{maint}*$m_{w\%}$ (A*B and A*C*D, **Table 5-2**) determine the presence of the curvature. The ramp time and the maximum applied pressure are correlated by the presence of the term t_{ramp}*P_{max} (A*B): upon this finding, we can hypothesize that the important term is the compression rate (A/B), confirming that the process, as could be expected, is sensitive to kinetics. It is worth of noticing that at the maintenance time is 0 a threshold pressure is present: above it the area increases in the same direction of the increase of the ramp time; instead, below it the direction is inverted. This pressure can be estimated in 377 MPa in case of 20 % of added water, and in 330 MPa in case of no water addition.

5.2.2. Process optimization: mechanical method

The mechanical properties of the sample changed during the process: from a spongy, soft to a hard-solid material. Due to this difference, a mechanical compressive test can also be used as an evaluation of the amount of sintered material. The results of the compressive test on the 16 samples is reported in **Figures 5-6, 5-7, 5-8, 5-9** as stress-strain curves. The value of the Young modulus was obtained from the linear part of the curves and used as yield to find a correlation with the process parameters.

An ANOVA test (**table 3-5**) was preformed, revealing that the model is significant. The surface plots of **Figure 5-10** show the results of the predictive model. The higher Young modulus is obtained, for t_{ramp} = 120 s, P_{max} = 400 MPa, t_{maint} = 0 s, and $m_{w\%}$ = 20 % of water.

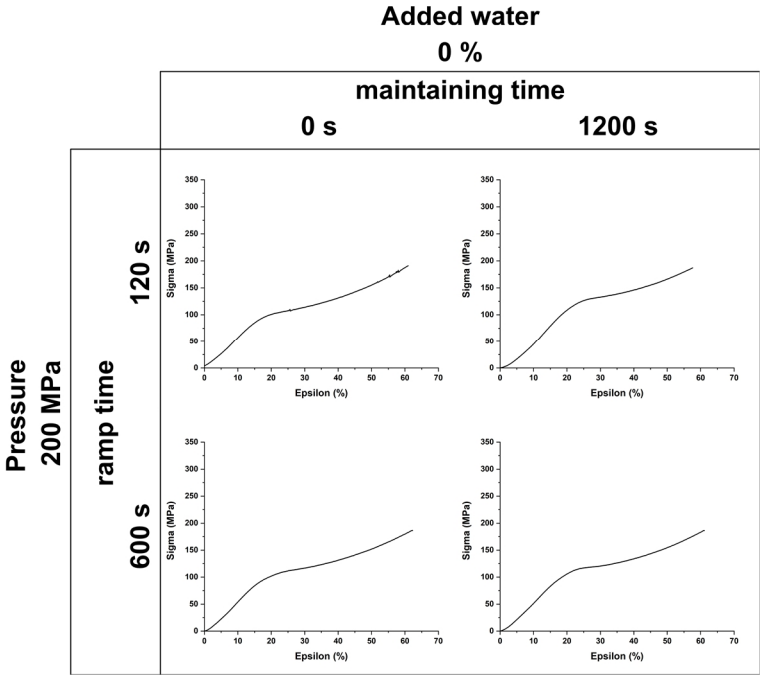

Figure 5-6: Compression test curve of the 4 samples prepared without the addition of water and with a maximum pressure of 200 MPa.

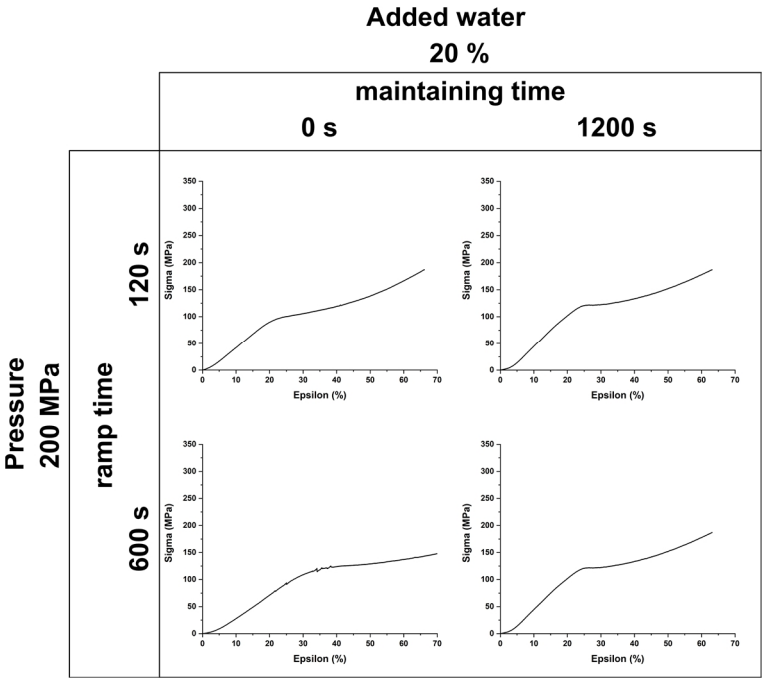

Figure 5-7: Compression test curve of the 4 samples prepared with the addition of 20% of water and with a maximum pressure of 200 MPa.

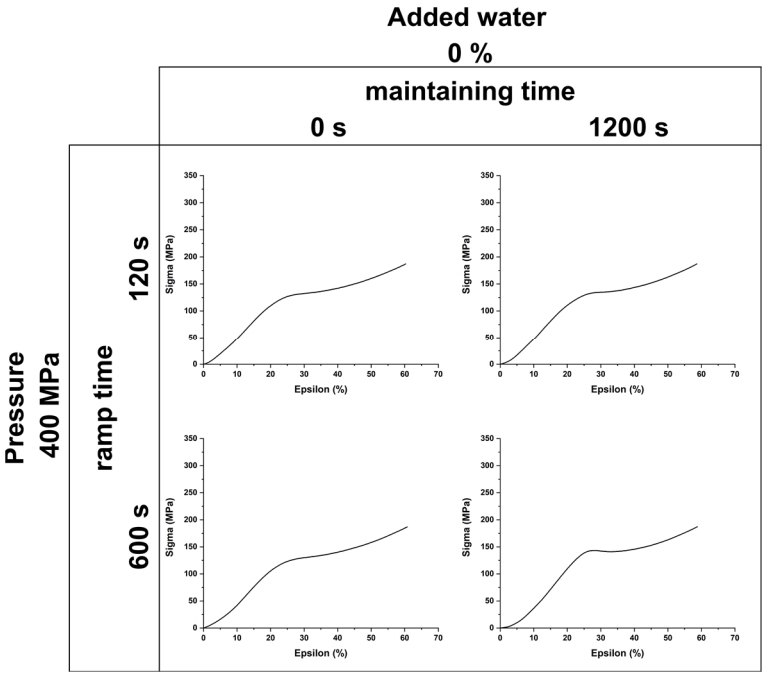

Figure 5-8: Compression test curve of the 4 samples prepared without the addition of water and with a maximum pressure of 400 MPa.

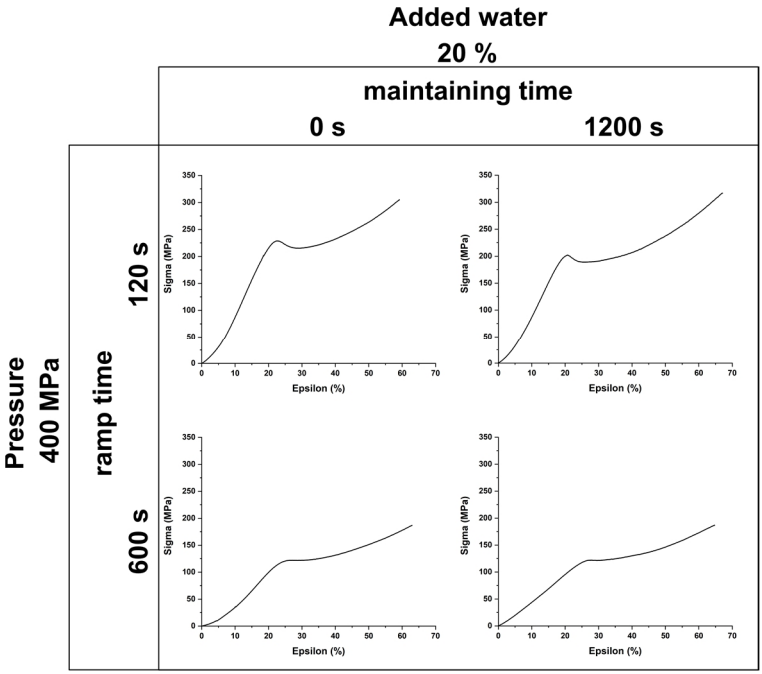

Figure 5-9: Compression test curve of the 4 samples prepared with the addition of 20% of water and with a maximum pressure of 400 MPa.

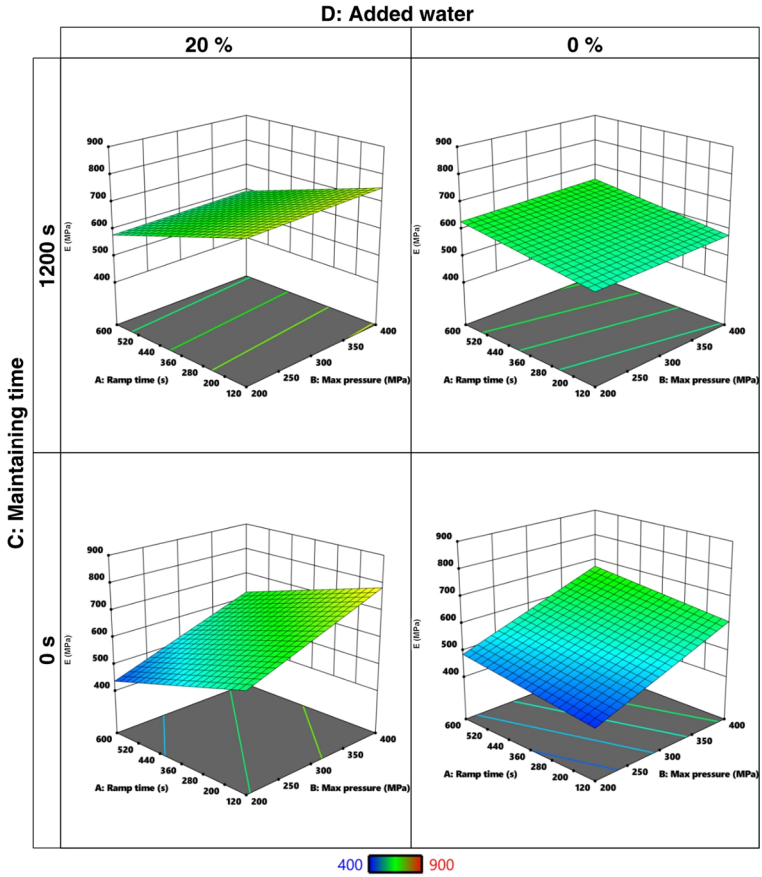

Figure 5-10: Surface plots based on the empirical model of the compression Young modulus as a function of the considered variables. This allows to predict in which direction the transition from lyophilized to solid silk fibroin occurs. In this case the maximization of the Young modulus can be obtained with a low ramp time, a high pressure, a low maintenance time, and with the presence of added water. However, since the maintaining time is not so significant on the Young modulus, in order to contemporary minimize the optical yield, the final chosen parameters for the optimized process are: t_{ramp} = 600 s, P_{max} = 400 MPa, t_{maint} = 1200 s, and $m_{w\%}$ = 20 %.

$$E_{comp} = 607.13 - 23.12 * A + 51.12 * B + 28.13 * C + 31.38 * D - 56.13 * A * D - 43.62 * B * C$$

$$E_{comp(95\%\ CI\ Low)} = 564.03 - 66.22 * A + 8.03 * B - 14.97 * C - 11.72 * D - 99.22 * A * D - 86.72 * B * C$$

$$E_{comp(95\%\ CI\ High)} = 650.22 - 19.97 * A + 94.22 * B + 71.22 * C + 74.47 * D - 13.03 * A * D - 0.53 * B * C$$

Source	Sum of Squares	df	Mean Square	F-value	p-value	
Model	1.596E+05	6	26605.58	4.58	0.0210	*
A-Ramp time	8556.25	1	8556.25	1.47	0.2557	
B-Max pressure	41820.25	1	41820.25	7.20	0.0250	*
C-Maintaining time	12656.25	1	12656.25	2.18	0.1739	
D-Water addition	15750.25	1	15750.25	2.71	0.1340	
AD	50400.25	1	50400.25	8.68	0.0163	*
BC	30450.25	1	30450.25	5.24	0.0478	*
Residual	52254.25	9	5806.03			
Cor Total	2.119E+05	15				

*Table 5-3: ANOVA table for the model (first equation on the top of the table) of the compression Young modulus. The significance level was assigned as follows: p≤0.1 (.), p≤0.05 (*), p≤0.01(**), p≤0.001(***). The model results to be significant with a p-value of 0.0210. The model can be used to predict the Young modulus and then the direction in which the solid-solid transition occurs. The significant term in order of importance are: A*D – max pressure*water content, B*C – max pressure*maintaining time, and B – max pressure. Equations of the 95% confidence intervals (CI) are reported after the model equation.*

As a general trend, the Young modulus increase with the increasing of the maximum applied pressure. In case of water addition this increment is in direction of the decrease of

the ramp time; on the contrary, in case of absence of added water the direction is the opposite: Young modulus increases proportionally with the ramp time. This complex behavior is due to the presence of the mixed term t_{ramp}*$m_{w\%}$ (A*D, **Table 5-3**) and it could be explained considering that water changes the overall kinetics of the process. In presence of added water, a high compression rate allows its diffusion into the sample and a full transition of the lyophilized fibroin to the solid state.

The presence of the mixed negative term P_{max}*t_{maint} (B*C, **table 3-5**) could be explained considering that a high pressure for a prolonged time, even if allows a complete transition, probably damages the sample, decreasing its compressive modulus. In absence of added water, a longer ramp time is necessary to obtain a better compaction and a higher mechanical strength. In conclusion, considering the fact that the maintaining time is not so influential on the Young modulus, to minimize the optical yield while maximizing the mechanical one, optimal parameters should be set as follows: t_{ramp} = 600 s, P_{max} = 400 MPa, t_{maint} = 1200 s, and $m_{w\%}$ = 20 %.

5.2.3. Compression test

Bones and all objects used in osteo-fixation are usually subjected to mechanical stresses. Therefore, to evaluate the response of our material, we performed a preliminary compression test. The compression modulus was evaluated on 3 samples produced by the optimized procedure in two conditions: after drying the samples in a desiccant chamber at 25 °C for 2 days (dried), and immediately after a 6 h immersion in water at 37 °C, to simulate physiological conditions (physio).

In accordance with a previous study, our results plotted in **Figure 5-11 A**, shown a dramatically decrease of the compression modulus in simulated physiological conditions: the modulus passed from 1120 ± 130 MPa (dried) to 205 ± 130 MPa (physio). This effect can be attributed to plasticizing effect of water. As result the samples, as can be seen in **Figure 5-11 B**, were strongly deformed during the compression test, passing from 8 mm to 1.2-1.5 mm of diameter, without braking.

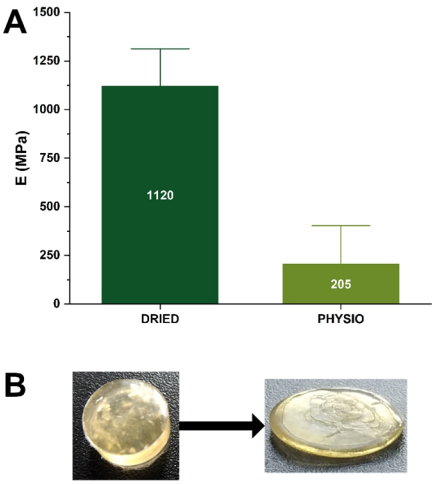

*Figure 5-11: (**A**) Compression modulus in normal condition (20% of humidity, 25 °C) and physiological condition (after 6h in water at 37 °C). The test was performed on 3 samples per each condition. As can be seen, a drastic reduction of the modulus is present in the simulated physiological conditions: this could be attributed to the plasticizing effect of the water. (**B**) Sample before (on the right) and after (on the left) compression, as can be seen the sample is deformed during the test, no breaks occur.*

5.2.4. Structural analysis

On the optimized process the secondary structure was evaluated by FTIR in the three main stages: after lyophilization, after the exposure to moisture, and after compaction. The comparison between the different spectra, in the range of the primary and secondary amide peaks, is shown in **figure 3-7 A**.

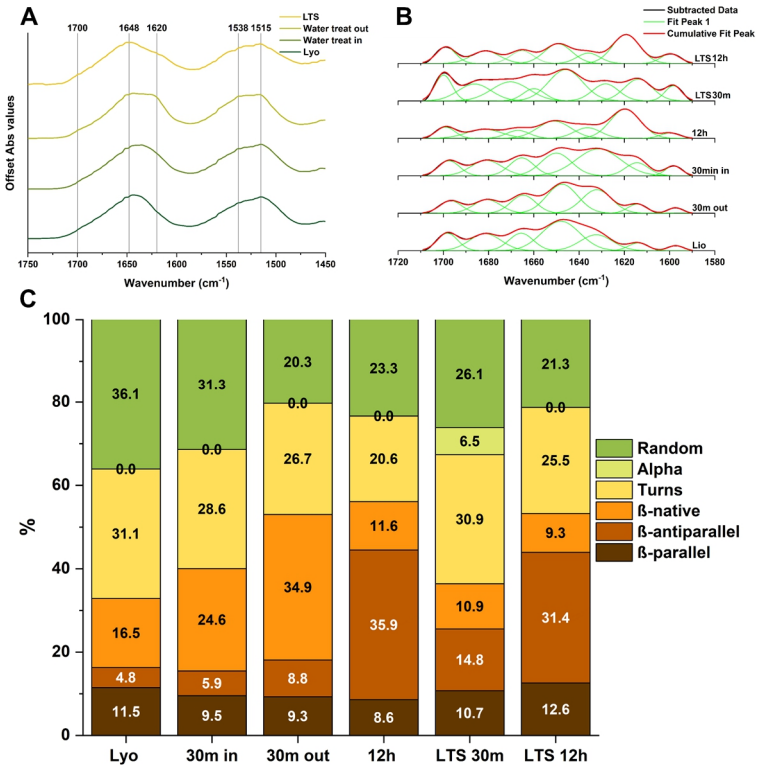

*Figure 5-12: (**A**) FTIR ATR spectra of the fibroin collected after the three principal stages of the process: the lyophilization (Lyo), the water treatment both on the surface (Water treat out) and the inner part (Water treat in) of the silk fibroin cylinder, and after compression (LTS). The wavenumber associated with the ϐ-sheet structure are 1700, 1620, and 1538 cm^{-1}; 1648 and 1515 cm^{-1}, instead, are associated with the random structure. The water addition increases the amount of ϐ-sheet especially on the surface. After the compression a "mean" secondary structure between the two obtained after the water addition is found: the compression phase allows the interdiffusion of the material, generating a uniform solid. (**B**) Deconvolution of the amide primary peak and (**C**) percentage of the respective area (on the bottom). The analyzed samples are: dry lyophilized silk fibroin (**Lyo**), internal part after 30 m of moisture exposure (**30m in**), external part after 30 m of moisture exposure (**30m out**), after 12 h of moisture exposure (**12h**), 30m exposed sample after compression (**LTS 30m**), 12 h exposed sample after compression (**LTS 12h**). The water*

treatment on lyophilized fibroin resulted in an increment of the native β-sheets and therefore in a decrease of the random structure. The inner part of the lyophilized cylinder resulted less susceptible to water addition. After compression the alpha helix structure was formed and the amount of parallel and antiparallel β structure increased, while the amount native β-sheet structure decreased.

After the water treatment we should distinguish between the external part of the fibroin cylinder and the internal part. The rapid addition of water via moisture absorption generates a gradient in the water content that decreases from the surface to inside the material. In this case the spectra (**Figure 5-12 A,** Water treat in) is somehow in between the one collected for the lyophilized fibroin (**Figure 5-12 A,** Lyo) and the one collected on the surface of the cylinder after the water treatment (**Figure 5-12 A**, Water treat out). On the surface (**Figure 5-12 A**, Water treat out) the FTIR spectra shows an increment in the intensity at 1620 cm^{-1} for the primary amide, and at 1538 cm^{-1} for the secondary amide: both are related to an increment of the amount of β-sheet structure[192].

After the compression (**Figure 5-12 A**, LTS) the intensities of the spectra at 1620 cm^{-1} and at 1538 cm^{-1} decreases as an effect of the interdiffusion of the surface and the inner part of the lyophilized silk fibroin cylinder. No further

differences can be detected between the surface and the core. No significant changes have been found in the intensities at 1700 cm^{-1} (β-sheet), 1648 cm^{-1} (random), and 1620 cm^{-1} (random) as can be noticed from **Figure 5-13**.

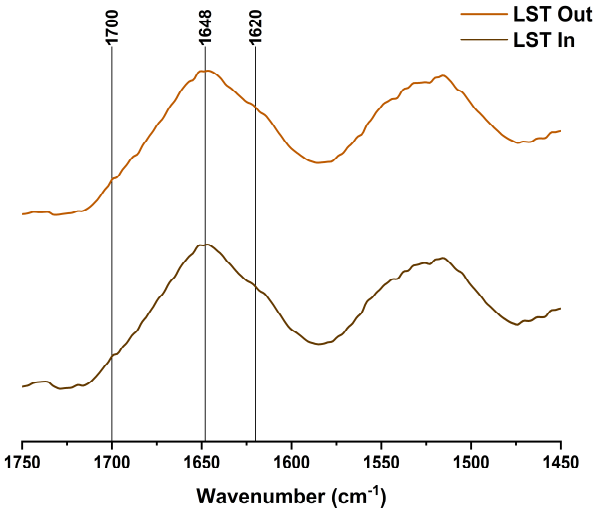

Figure 5-13: Comparison between the internal and the external part of the cylinder spectra collected after sintering.

In order to quantitively evaluate the changes in the secondary structure, a more accurate analysis was conducted on the deconvoluted primary amide peak. The peak assignment was conducted following **Table 1-1**. **Figure 5-12 B** shows the deconvolved curves and **Figure 5-12 C** the percentage amount of each structure in the different phases of the process. These

analyses reveal that the water treatment conducted for 30 m (**Figure 5-12 C**, 30m) increases the amount of native β-sheet (peak centered around 1630 cm^{-1}) on the cylinder surface (35 %) and in a smaller amount also in the inner part (26 %); this is accomplished by a decrement of the random coil and β-turns. On the contrary, parallel and antiparallel β-sheets do not significantly change during this stage. After the compression the secondary structure results to be homogeneous. In fact, an intermediate composition between the two analyzed (external and internal) after the water treatment should be expected. This is true for the random coil structure, resulting 26 % in amount, the exact mean between the 31 % of the surface and the 20 % of the internal part. Conversely, the native β-sheets amount decreases of about 19 % compared to the mean (29.7 %) and both the parallel and the antiparallel β-sheets increase of an amount of 1.3% and 7.3 % respectively (compared with the mean values 9.4% and 7.4 %). In addition, the alpha helices are formed in an amount of 6 %.

We can hypothesize that the stabilization due to the β structure before the compression plays an important role in the possibility for fibroin to undergo a complete solid-solid

transition. To prove this hypothesis, we tried to produce a sintered sample, leaving a block of lyophilized silk fibroin in a humidostatic chamber overnight, and then compressing it without success. The reason of the missing transition can be attributed to the conversion occurred between β-native and β-antiparallel structures. As can be noticed, from **Figure 5-12 C**, passing from a 30 min to 12 h of moisture exposition caused a significant increase in β-antiparallel (from 8.8 to 35.9 %) and decrease in β-native (from 34.9 to 10.9 %) structures: this transition could explain the stabilization of silk fibroin due to water exposition, differentiating the natural material from the treated one (water annealing).

As a negative result, when we compressed the sample that had been exposed 12 h to moisture, the molecular interdiffusion did not occur, even applying the best process conditions. To explain this effect, we observed that the deconvolution of the primary amide peak of the material post-compression (**Figure 5-12 C**, LTS 12h) had few differences in the secondary structures if compared with the pre-compression (**Figure 5-12 C**, 12h): an increase in the amount of β-turn (from 20.6 to 25.5 %) and β-parallel (from 8.6 to 12.6 %) and a slightly

decrease in the amount of random coil (from 23.3 to 21.1 %) and β-antiparallel (from 35.9 to 31.4 %). We can attribute the impossibility of a thermal-reflow to the large amount of β-antiparallel structures that, due to their high conformation stability, can withstand the external applied force without undergoing to conformational changes.

5.2.5. Thermal analysis

Differential scanning calorimetry in the range of 40-320 °C, shown in **Figure 5-14 A**, has been used to evaluate the glass transition temperature (T_g)**.** Lyophilized silk fibroin (Lyo) shows a T_g around 180 °C (black arrow), followed by an exothermic peak of crystallization with the maximum centered around 225 °C (red arrow, ΔH = 3.45 mJ/mg). The loss of water and the degradation peaks maximums are at 100 °C (ΔH = 20.63 mJ/mg) and at 285 °C (ΔH = 27.34 mJ/mg).

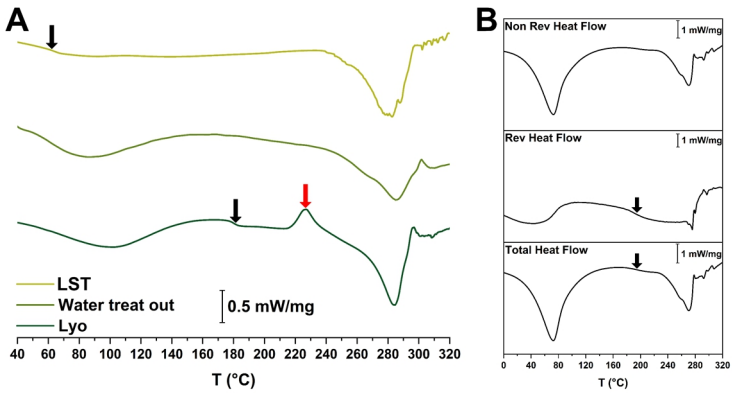

*Figure 5-14: (**A**) Differential scanning calorimetry (DSC) of the sample after the three main stages of the process: the lyophilization (Lyo), the water addition (Water treat out) and, the compression (LTS). The black arrows indicate the position of the glass transition temperature (T_g). (**B**) Modulated DCS of the water treated sample. The reversible and the total heat flow show a T_g around 180 °C, the same position of the one reported for the lyophilized sample. The rapid exposition of lyophilized silk fibroin to water does not change the glass transition temperature.*

A T_g at 65 °C (black arrow) can be identified after compression (LTS). In this case neither the water peak, nor the crystallization peaks are present, indicating the absence of both water in the network and of structural transitions to the crystalline form. The degradation peak is in the same position as the previous case. The T_g cannot be detected for the material exposed to moisture: the presence of water and the thermal treatment of the DCS process, in fact, can plasticize the material and, because of the little amount of random structure, it is

extremely difficult to determine the glass transition temperature. In this case, the water peak has a maximum at 85 °C (ΔH = 25.38 mJ/mg) with a larger area as a consequence of water addition, while the position of degradation peak remains, in this case as well, unchanged, with a maximum at 285 °C (ΔH = 19.24 mJ/mg).

To correctly estimate the position of T_g, a modulated DSC was performed on this material. The reversible, non-reversible, and total heat flows are shown in **Figure 5-14 B**. The T_g can be detected in both the total and the reversible heat flow signal around 180 °C (black arrows). We can conclude that the rapid exposure to water moisture does not change the glass transition temperature of the lyophilized fibroin and the decrease of the T_g on the solid protein is obtained during the compression phase; this is in accordance with the previous result obtained by the optical and the mechanical DOE when the significance of mixed term involving the water addition had been uncovered (for the optical method A*C*D , A*D, for the mechanical method A*D C*D ramp time*max pressure).

5.2.6. Microstructural analysis

We observed the thermal-reflow at the microstructural level by following the compression test at different time points (0, 40, 80, and 120 s). The SEM micrographs shown in **Figure 5-15** reveal the formation of planes perpendicular to the compression direction (indicated with the black arrows).

Separate planes are visible at low magnification (column 1) in the pre-compressed sample (0 s) and after just 40 s they appear to be collapsed. After 80 s the planes are no longer visible; on the contrary, some ripples along the compression direction (80 s, 100 X) indicate that the planes are melted together, and the overall structure is more compact. After 120 s the structure is fully compact: no more planes or ripples are recognizable, and the microstructure shows the typical appearance of a brittle fracture (120 s, column 1).

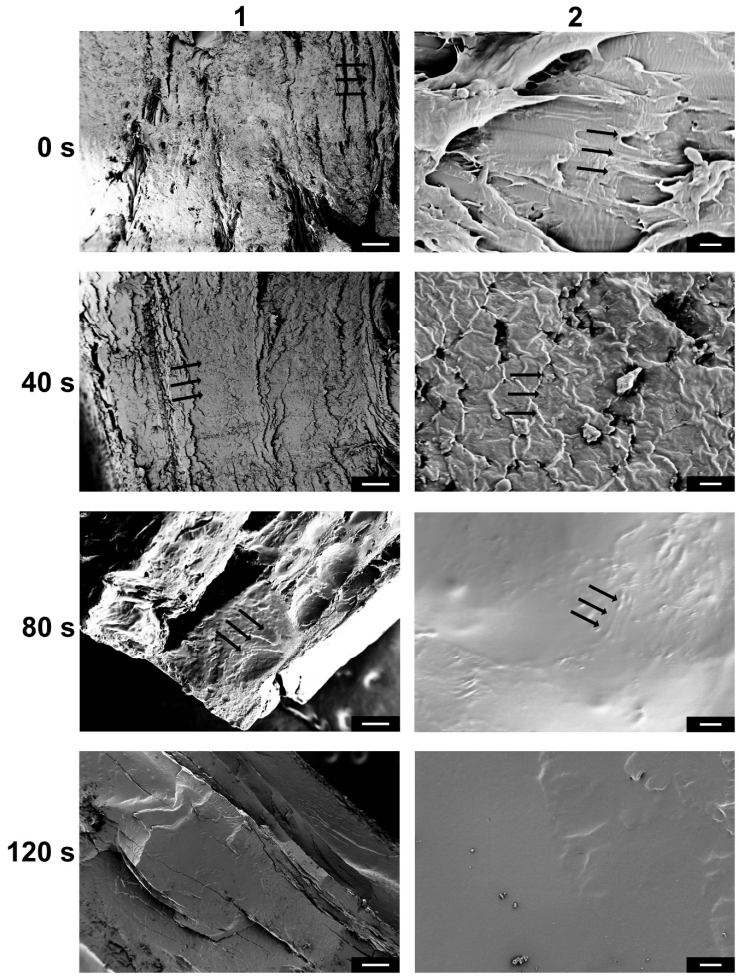

Figure 5-15: SEM micrographs during different time points on the optimized compression phase: just after the pre-compression (0 s), then at 40 s and 80 s, and at the end of the process (120 s). The black arrows indicate the direction of the compression (detectable from the stratified structure formed during the process). In particular, the "planes" are perpendicular to the compression. These structures can be clearly recognized in the pre-compressed material (0 s) and in the first time point (40 s), in the lower magnification (column 1). At higher magnification (column 2) we can observe the viscous flow occurring, the formation of ripples (40 s) and their flow (80 s), forming a compact

material (120 s). The flow is visible also at higher magnification (80 s, column 1), where the material seems to be in a sort of melted state. After 120 s the material results to be compact (120 s column 2), with typical microstructure of a brittle fracture (120s, column 1). Scale bar are 250 µm for column 1, and 2 µm for column 2.

At higher magnification (column 2) we could observe the thermal-reflow taking place: nanometric ripples appear after the pre-compression (0 s), with a crest to crest distance of 288 ± 15 nm. At 40 s we could observe a ripples structure in the micrometric scale; in this case the estimated crest to crest distance is 3 ± 1 µm. This kind of structure is no longer visible at 80 s where we can observe only few crests in a compact material. At 120 s the material is fully compacted. The overall process can be a flow of material that, from the micrographs, seems to be a sort of viscous fluid until it reaches a solid form. This is compatible to previous studies that reports this phenomenon when fibroin temperature is raised above the T_g.

5.2.7. *In vitro* cell culture and confocal imaging

Cell substrate (adhesion) and cell-cell interactions are crucial to regulate wound healing and functional tissue regrowth. To evaluate the impact of surface chemistry on cell adhesion, adipose-derived mesenchymal stem cells (AdMSCs) were cultured on all samples up to 5 d, and cell adhesion, morphology, and cytoskeleton organization were evaluated through confocal microscope imaging. Cytoskeleton fibres, mainly composed by actin, play an important role particularly in cell adhesion, cell shape, and cell migration, and their organization is affected by intracellular signaling integrin activation[193] **Figure 5-16** displays images acquired at the confocal microscope on samples at different culture time points. Cytoskeleton fibres structures are visible in green (CytoPainter Phalloidin-iFluor488 dye) in all sample images. Cells nuclei, coloured in blue (4′,6-diamidine-2′-phenylindole dihydrochloride (DAPI dye)), are difficult to detect in the cells adhered to LST samples. In fact, DAPI and silk fibroin are both excited in the same range of wavelength and they also emit in the same spectral region. As a result of the fibroin autofluorescence the

material underlying the cells is visible and of the same colour of the cell nuclei. In general, cells were able to homogeneously adhere and populate all sample surfaces starting from day 1 (Figure 7). However, at day 5 LTS and poly-ε-caprolactone (PCL) surfaces influenced, in a different fashion, cell adhesion in terms of spreading degree, cell density, and cytoskeleton organization. Cell adhered to PCL with high density but with a low degree of spreading, assuming a more spindle shape fibroblastic-like, anchored to the substrate through numerous filopodia (particularly evident 3 d after seeding). On the contrary, in LTS samples a lower density of cells, with higher spread, and an osteoblastic-like morphology was observed. Cytoskeleton stress fibers adopted a quite different organization, with actin filaments along the cellular processes. It should be noticed that cell–cell and cell–substrate interactions are mediated by lamellipodia formation, visible starting from day 1.

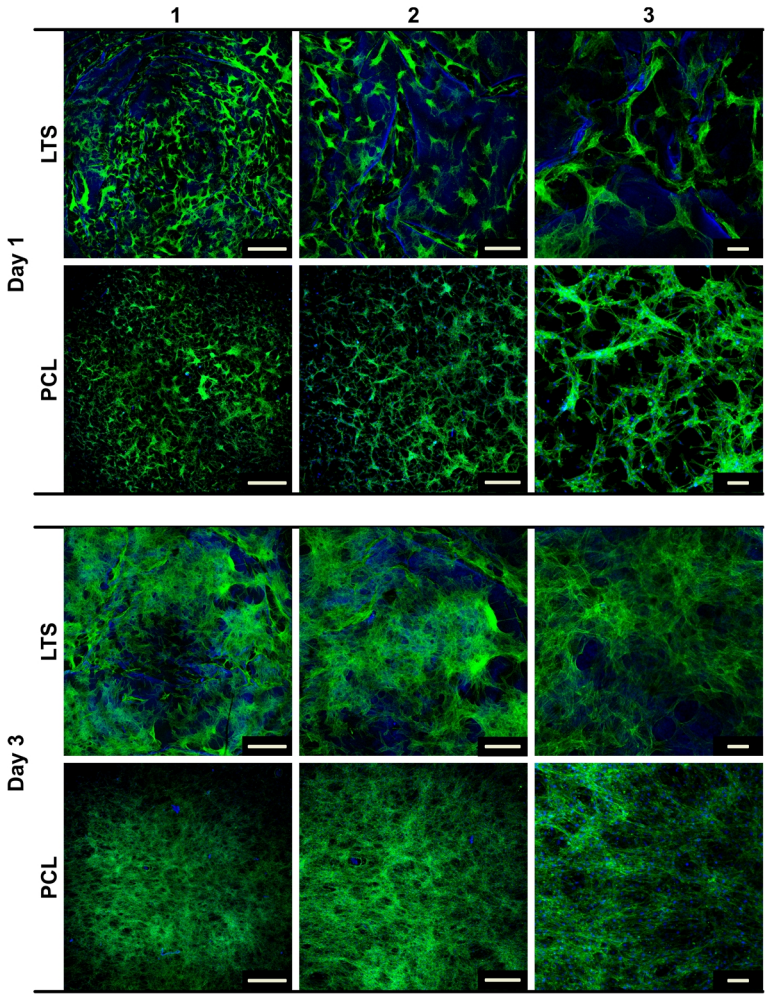
1
2
3
Day 1
LTS
PCL
Day 3
LTS
PCL

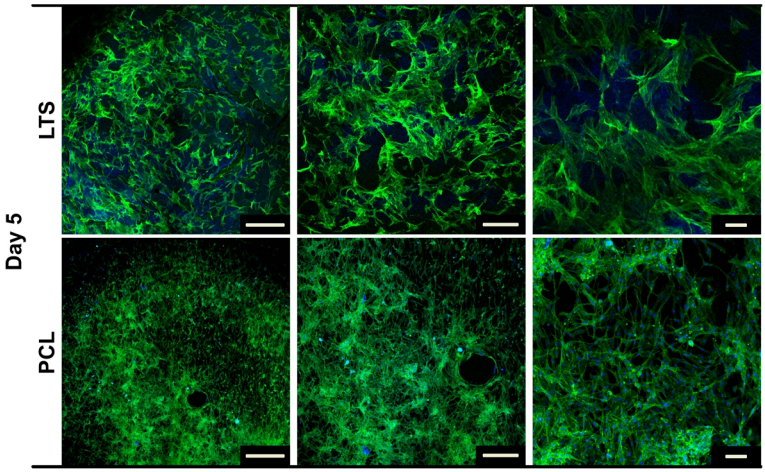

Figure 5-16: Confocal microscopy images of adhered cells at different time points on both types of samples at three different magnifications. AdMSCs cytoskeletal morphology and distribution (green staining cytoskeleton, blue staining DAPI and LTS fibroin samples). Scale bar are 1000 µm for column 1, 500 µm for column 2, and 100 µm for column 3.

5.3. Discussion

The possibility to obtain under compression, at low temperature, a full transition to a bulk solid material resulted to be susceptible to several restrictions. The thermal-reflow is a phenomenon that occurs in silk fibroin at temperature higher than T_g and allows a molecular flow that permits a reconfiguration of the material[186–188]. The addition of water as plasticizer can promote this process allowing a decrease of the T_g[186–188]. However, the exposure to water modifies the protein

secondary structure promoting the physical crosslinking (the transition of the secondary structures to the stable β form)[187,194–197].

In our case, a trade-off between the reduction of T_g and the necessity to maintain a starting material with a low crystallinity was fundamental. To achieve this result, the lyophilized silk fibroin was rapidly exposed (30 to 60 min) to water moisture in an humidostatic chamber prior to its compression. This allowed to avoid a high degree of crystallization of the material even if a 20% w/w of water was added. However, the T_g resulted to be unaffected by the treatment. Interestingly, this finding seems to be in contrast with previous literature results where a decrease of T_g down to 40°C due to water absorption is reported[187].

However, we must take into consideration the different nature of films and lyophilized silk fibroin blocks: the former exposes the major part of their surface, while the latter exposes only a part of their free surface; in this latter case water moisture needs more time to enter the pores and plasticize the material.

During compression the fast application of a high pressure allows the fast diffusion of the water in the inner part

of the lyophilized block and the thermal-reflow occurred. We hypothesize a fast decrement of the glass transition temperature by the combined effect of the high pressure applied and the presence of water. Therefore, even though after the exposure to water moisture the T_g of the lyophilized silk fibroin was around 180 °C, during the compression its value decreased under 40 °C, allowing the molecular flow to take place. This hypothesis was further confirmed by SEM microstructural analysis, where a “flow” appeared to take place before the full compaction. The hypothesis of the decrease of the T_g under high pressure compression is reported as measured effect on glasses[198–200]; on the contrary, in case of polymers the compression is reported to increase the T_g[201]. To our knowledge, no study on the shift of the glass transition temperature has been reported in the specific case of proteins. Our hypothesis still needs further study to be confirmed.

After the compression some alpha structures were formed, and the sample resulted to be higher in β-turns, parallel, and antiparallel β-sheets all at the expense of a decrease in the native β-sheet. Instead, the random coil percentage remained unchanged. The shift from native β-sheet to the more stable

form of β-sheets was recently reported in literature[40] for fibroin where the transition from the native solution collected in a specific area of the Bombyx mori worm to micrococoons has been studied. This transition is well-established in literature for proteins that tends to form amyloid[42,43,48,57].

The necessity to have a starting material with a low crystallinity was proved by performing the compression on a highly crystalline lyophilized sponge (obtained by 12 h of water annealing). As discussed above, we were not able to obtain the transition to a solid material. This effect was attributed to the large amount of β-structures of the starting material, which are mechanically resistant[34] and could in some extent prevent the molecular flow. To our knowledge, this is the first time that this effect has been reported in literature. In fact, a high crystalline silk powder is usually used in compression molding a high temperature (100-200 °C) to produce solid monoliths[16–18], while low temperatures were never accessed before.

The material obtained with our protocol showed interesting results in term of cell adhesion through different time points and comparable to the results obtained on PCL, material commonly used in biomedical applications[202]. The high degree

of spreading of cells on the surface can indicate that, since LTS fibroin samples are made of protein, their surfaces offer more adhesion sites to cells, improving the mechanism of interaction between cells and surface[99,203–208].

5.4. Conclusions

We were able to optimize a methodology that combines a fast processing, typical of the solid-solid transition obtained by sintering, with a low temperature, typical of the solution-gel-solid transition obtained by solvent evaporation.

Our process allows the dramatical reduction of time to obtain a solid form of fibroin (from weeks to minutes) and, the decreasing of the temperature required down to 40°C, thus proving the possibility of a thermal-reflow at low temperature.

The main limitation of our protocol is the necessity of high pressure; this parameter can be lowered at the expense of the requirement of an increase of the temperature. Regarding the material, the low glass transition temperature and the decrease of the compressive elastic modulus in a wet environment represents the main limitations for possible applications (e.g.

osteo-fixation[209]). These problems could be solved in the future by the use of a chemical modified material as Sil-MA and performing a chemical crosslinking during the compression process.

6. Micropatterning of optical quality fibroin films

Part of this chapter has been published in:

Fabrication of nanoscale patternable films of silk fibroin using benign solvents

Alessio Bucciarelli, Ramendra K. Pal, Devid Maniglio, Alberto Quaranta, Viviana Mulloni, Antonella Motta, Vamsi K. Yadavalli
Macromol. Mater. Eng, **2017**, 1700110,1-9

A comparative study of the refractive index of silk protein thin films towards biomaterial based optical devices

Bucciarelli a, V. Mulloni, D. Maniglio, R.K. Pal, V.K. Yadavalli, A. Motta,A. Quaranta
Optical Materials, **2018**, 28, 407-414

6.1. Introduction

Optical devices and bioelectronics required the use of micro- and nanopatterns[10]. In optical applications, this kind of structures when in the same order of magnitude of the used wavelength, are able to interact directly with light[96]. The production of these features using silk fibroin is reported in literature by using different techniques such as

nanoimprinting[96], soft lithography[210], silk transfer applied micropatterning (STAMP)[211], electron beam lithography (EBL)[126], breath figures[212], laser ablation[213], and photolithography[83,124].

Photolithography is a standard and convenient technique to produce engineered structures with controllable dimensions over multiple length scales and it allows to produce patterns, even on large surfaces at high resolution and speed. Resolution of 1 μm can be obtained by using chemically modified silk fibroin produced by grafting methacrylate groups as side groups on the protein chain residues[12,13]. This modified protein, called fibroin photocrosslinkable photoresist (FPP), can be processed after film formation by UV exposure through photomask and then etched to produce microstructures.

FPP due to its chemical features is reported to be water insoluble so, to produce a film from this material the original protocol required the use of hexafluoroisopropanol (HFIP) as solvent. However, HFIP is not an optimal solvent owing to its acute oral, dermal and inhalation toxicity, high cost and need for careful disposal[214]. As a fluorinated alcohol, HFIP needs to be handled using the pesticides disposal protocols and, this

make its management expensive. In addition, its high volatility makes it difficult to obtain a uniform film thickness with low roughness using spin coating processes. To form stable films with characteristics that match the requirements for optical applications, the use of an alternative and possibly green solvent is highly desirable.

To improve the pre-existing protocol, we proposed Formic Acid (FA) as solvent for FPP. Formic Acid is the simplest organic acid: it decomposed in carbon monoxide (CO) and water (H_2O) herein it is environmentally friendly and easily disposed. Further, the lower vapor pressure of FA ensures a lower evaporation rate, if compared with HFIP, allowing the liquid phase to last longer and, indeed, to control the spin coating process more accurately.

Using an optimized spin coating procedure in combination of FPP dissolved in FA, we were able to produce thin films (100-1000 nm) and to pattern them. An extensive comparison between films obtained by the two solvents (HFIP and FA) has been conducted in order to prove their interchangeability. Both solvents result in similar film morphology, roughness and mechanical properties at the

nanoscale as observed using atomic force microscopy. However, using spin-coating, FA can form more stable and uniform films with controllable thickness in comparison to HFIP.

Since this resist and its counterpart obtained from sericin[19] (sericin photocrosslinkable photoresist, SPP) were used to develop micro-optical devices[215], we decided to perform a refractive index characterization taking the advantage of the superior quality of films produced by our technique. We were able to determine, for the first time, the index of refraction of this resist. Furthermore, using the same technique we characterized the refractive index of the resist obtained from sericine (Sericine Photocrosslinkable Photoresist, SPP) and of the natural proteins, fibroin and sericine, both in water and in FA.

6.2. Results

In the early stage of the production of components such as MEMS, flexible electronic devices, microfluidics the deposition of a film is required. At the industrial level these films are usually produced via spin coating, a scalable and easy technique that ensures reproducible results. This process,

commonly used for commercial photoresists, has been adopted in literature also for the deposition of aqueous solutions of fibroin[124,126].

However, forming thin (100-1000 nm) and ultrathin (1-100 nm) silk films is still a challenge. In case of fibroin photoresist, due to its hydrophobicity, the use of water as solvent is not possible. So, to form films and then micropattern HFIP is the common solvent[12,13,137,215]. The choice of the solvent is especially fundamental to the process of spin coating itself, as it affects the viscosity of the film and coating parameters. Here, the use of HFIP does not allow the production of films with a quality suitable for optical applications. In particular, the thickness obtained via spin coating results to be not reproducible.

Modifying the precedent protocol[20,21], introducing the use of formic acid (FA) as an alternative solvent we were able to produce films with an excellent surface quality and a controllable thickness. This allowed the determination of the refractive index of FPP, and using the same technique also of SPP.

6.2.1. Thickness characterization

Films were formed from protein solutions with equal concentration but different solvent (HFIP and FA) using the identical spin coating process and increasing the maximum angular velocity (RPM) at each produced film in order to observe the trend of the thickness versus RPM in relation with the used solvent. The maximum achieved rotations per minute (RPM) were set to 1000, 1500, 2000, 3000, 4000.

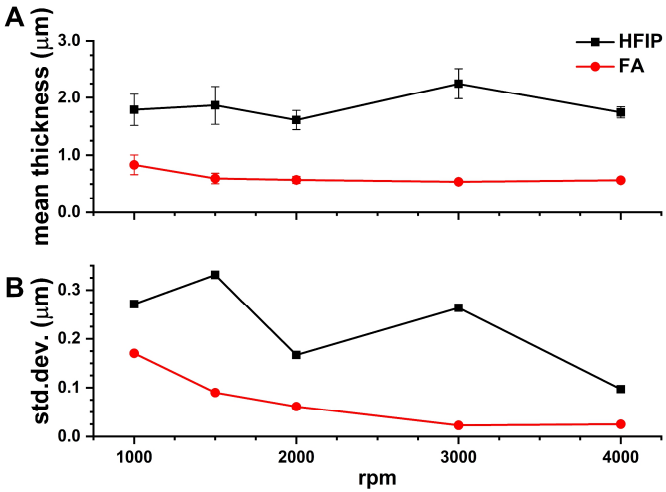

*Figure 6-1: Profilometry data for fibroin films formed by spin coating of solution made with two different solvents - HFIP (black) and formic acid (red): (**A**) mean thickness trend over rpm, (**B**) standard deviation of the mean thickness trend over rpm. Films formed using FA results to be thinner and more uniform (as the standard deviation suggests).*

From the results shown in **Figure 6-1** we can observe that use of FA as a solvent formed thinner and more homogeneous films in comparison with the films produced under the same conditions using HFIP as solvent (**Figure 6-1 A**). The mean thickness of FA films are 2-4 times lower than the thickness of HFIP films formed under the same conditions (**Figure 6-2 A**).

The mean thickness standard deviation is proportional to the thickness uniformity (**Figure 6-2 B**): this measure was calculated to determine the height variation across different films prepared under similar conditions. The lower standard deviation obtained in case of FA shows that the reproducibility of film thickness was higher. The best result was obtained at 3000 rpm, in this condition thin films (0.54±0.02 μm thickness) were formed with a very low deviation. In order to form thinner films, the concentration of the solution was reduced: with a concentration of 1.5% w/v in FA the thickness obtained was approximately 172 nm, using even a lower concentration, 1.2% w/v, the thickness was around 115 nm. In this case, the film thickness was obtained via ellipsometry while in other cases the uses of AFM on film scratch was adopted[86,216].

6.2.2. Optical characterization

The transmittance spectra, shown in **Figure 6-2 B**, over the visible range (400nm-700nm) shows that FA fibroin films tend to have a flat response with transmittance around 90%. In comparison, HFIP films have not flat response and their transmittance monotonically decreases from 68% (700 nm) to 45% (400 nm). Both films have UV absorption edge, lying around 300 nm.

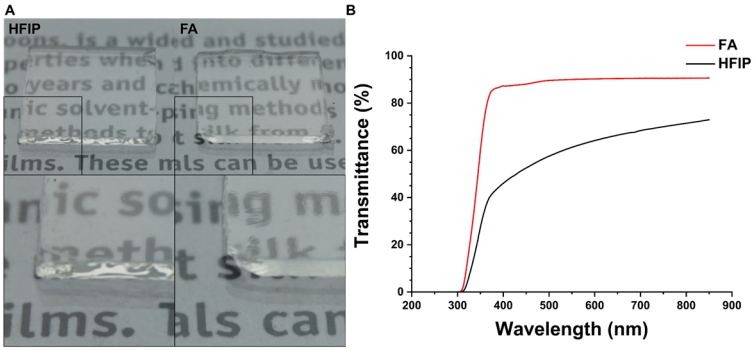

*Figure 6-2: (**A**) Images of films obtained by solvent casting showing optical properties: produced using HFIP and Formic acid. (**B**) UV-Vis spectra of films made using formic acid (red) and HFIP (black) showing the percentage transmittance and absorbance spectra. As can be noted FA films result to have a more homogenous surface (**A**, **FA**) in comparison with the surface obtained by HFIP (**A, HFIP**). This result is clearly shown also in the transmittance spectra (**B**) where films produced by FA tends to have a flat and high response.*

The flat and high transmittance spectra of FA films ensure their transparency whereas, the spectra of the HFIP

films is indicative of low transparency, probably due to the light scattering from the superficial inhomogeneities at the milli- and microscale, as highlighted from the morphology obtained with the mechanical and optical profilometer. This scattering phenomenon is an issue for light that has to be transmitted through the material; in fact, due to the monotonical decrease in the transmittance, the spectra of the transmitted light could be modified in accordance with it, giving an output spectrum with modified relative intensities.

The better quality of the FA films can be also seen by a visual comparison. In fact, as shown in **Figure 6-2 A** the surface of the HFIP film results to be high enough to deform the image of the underlying text. In comparison the FA film consent a perfect readability, permitted by the low roughness.

Thus, as a solvent for optical purposes such as low loss waveguides, FA should be preferred to HFIP. Interestingly, the high optical quality of these films allowed ellipsometric analysis, which is quite unusual in the case of protein materials due their typical optical inhomogeneity.

6.2.3. Refractive index characterization

The knowledge of the refractive index is fundamental for the design of optical components: it allows, in fact to simulate the response of the material via ray tracing[217–219] or solving the Maxwell equations[220,221]. The optimized spin coating deposition on silicon substrates of a low concentration of protein consents to obtain films with an extremely low roughness even at the square millimeter scale. On these films we were able to conduct ellipsometric measurements from 400 nm to 1500 nm in order to determine the refractive index of the material.

Sellmeier and Cauchy dispersion models (equations in **Table 6-1**) were used to fit the collected data assuming an extinction coefficient k equal to zero. In our specific case this last hypothesis appears to be reasonable; indeed, the absorbance of the thin films is negligible out of the UV region[222]. The two models gave RI values identical to four significant figures, for this reason only one result is reported in **Table 6-2**.

Film	Sellmeier Parameters $n(\lambda) = A + B\frac{\lambda^2}{\lambda^2 - {\lambda_0}^2}$			Cauchy Parameters $n(\lambda) = A + \frac{10^4 B}{\lambda^2} + \frac{10^9 C}{\lambda^4}$		
	A	**B**	**λ_0**	**A**	**B**	**C**
FPP/FA Ex	1.5	0.8	151	1.533	0.7	-0.02
SD FPP/FA Ex	0.2	0.2	16	0.002	0.1	0.3
FPP/FA Unex	1.3	1.0	150	1.528	0.82	-0.08
SD FPP/FA Unex	0.2	0.2	12	0.002	0.09	0.1
rSF/FA	1.8	0.5	189	1.527	0.55	0.3
SD rSF/FA	0.1	0.1	17	0.001	0.05	0.2
rSF/H_2O	1.82	0.53	164	1.533	0.43	0.2
SD rSF/H_2O	0.05	0.05	3	0.001	0.09	0.1
SPP/FA Ex	1.5	0.8	164	1.524	0.6	0.4
SD SPP/FA Ex	0.3	0.3	27	0.001	0.1	0.3
SPP/FA Unex	1.5	0.8	162	1.525	0.65	0.2
SD SPP/FA Unex	0.2	0.2	21	0.001	0.08	0.1
SN/FA	1.56	0.80	158	1.536	0.69	0.11
SD SN/FA	0.07	0.08	9	0.001	0.03	0.05

Table 6-1: Fitting parameters and their standard deviation (SD) for the two models used to calculate RI of silk films. Average fitting parameters and SD values were calculated from the results of different measurements on films of the same type.

Wavelenght (nm)	500	630	800	1000	1200	1400	1500
FPP/FA Ex	**1.5595**	**1.5494**	1.5432	1.5398	1.5377	1.5366	1.5362
SD	**0.0013**	**0.0010**	0.0009	0.0008	0.0008	0.0008	0.0008
FPP/FA Unex SD	**1.5605** **0.0018**	**1.5485** **0.0014**	1.5411 0.0012	1.5371 0.0012	1.5347 0.0012	1.5334 0.0013	1.5329 0.0013
rSF/FA	**1.5541**	**1.5429**	1.5363	1.5326	1.5307	1.5295	1.5291
SD	**0.0024**	**0.0018**	0.0013	0.0010	0.0009	0.0008	0.0008
rSF/H_2O	**1.5537**	**1.5456**	1.5406	1.5378	1.5364	1.5355	1.5352
SD	**0.0005**	**0.0001**	0.0003	0.0005	0.0005	0.0006	0.0006
SPP/FA Ex	**1.5543**	**1.5424**	1.5352	1.5311	1.5290	1.5277	1.5272
SD	**0.0004**	**0.0010**	0.0012	0.0013	0.0013	0.0013	0.0013
SPP/FA Unex SD	**1.5536** **0.0021**	**1.5423** **0.0014**	1.5353 0.0012	1.5314 0.0012	1.5293 0.0012	1.5280 0.0012	1.5275 0.0012
SN/FA	**1.5651**	**1.5538**	1.5470	1.5431	1.5411	1.5398	1.5394
SD	**0.0010**	**0.0009**	0.0011	0.0012	0.0013	0.0014	0.0014

Table 6-2: RI and SD of the measured thin films at different wavelengths. The two commonly used wavelengths (500 nm and 630 nm) for the characterization of silk fibroin are in good agreement with those reported in the literature. Note that the RI values were the same regardless of the dispersion model used.

In case of biopolymers such as silk protein, due to their intrinsic variability, both in the chemical composition and in the secondary structure, the RI of films prepared from the same batch and under the same conditions may be slightly different. In addition, we should take into account the variability present in the process. Therefore, 2 measurements were taken on each of the 3 films prepared from the same protein in the same conditions, then the mean and the standard deviation (SD) were

calculated. In this case, the standard deviation has to be considered as a measure that considers the overall reproducibility of the process, and not the precision of a single measurement.

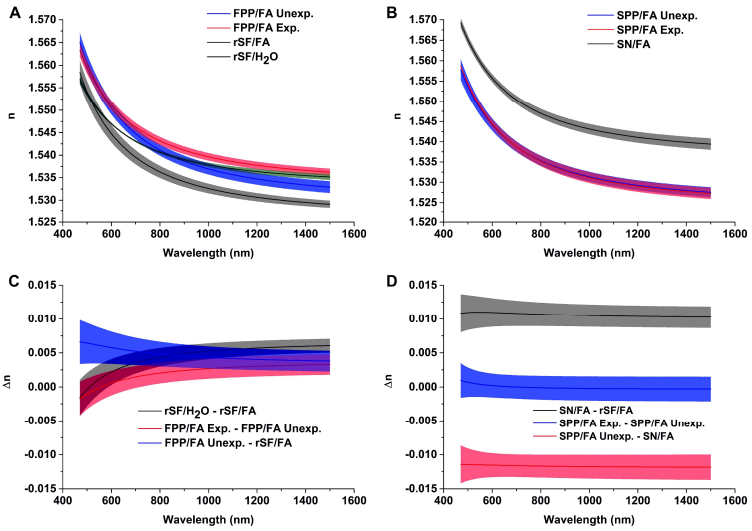

*Figure 6-3: (**A**) and (**B**), dispersion curves with error bars of RI for rSF/FA (a, black line), FPP/FA Unex (**A**, blue line), FPP/FA Ex (**A**, red line), SN/FA (**B**, black line), SPP/FA Unex (**B**, blue line) and SPP/FA Ex (**B**, red line). As can be noticed, the methacrylation process increases the RI for silk fibroin and decreases the RI for silk sericin. The UV exposure further increases the RI for FPP/FA films and leaves unchanged the RI for SPP/FA films. (**C**) and (**D**), RI difference and error bars as a function of the wavelength between different film types. A positive difference indicates that the first material can be used as lightguide when surrounded by the second material. On the contrary, a negative difference indicates the possibility to use the second material as lightguide when surrounded by the first one. A difference should be considered significant if the error bars do not intersect the 0 line (dashed black line).*

In **Figure 6-3 A** and **B** the RI dispersion curves are reported for the different films calculated from the interpolation of the ellipsometric data. The SD are indicated by the bands surrounding the curves. In **Table 6-2** the RI at the reference values of 500 nm and 630 nm are reported. For instance, the value obtained at those wavelengths (**Figure 6-3 A**, green and black line respectively) are consistent with the literature data [20,222–225]. The refractive index at 630 nm of rSF from FA is 1.5429 and from water is 1.5456 and, at 500 nm the RI are 1.5541 and 1.5537, respectively.

At higher wavelengths the RI of films produced from these two solvents start to diverge (**Figure 6-3 C**, black line). **Figure 6-3 C** and **D** report the differences of RI across curves of each biomaterial within the relative SD deviations calculated using the error propagation formula. The difference should be considered significant for a specific wavelength if there is no overlap between the error bar and the 0 line.

The RI variation (0.0064 at 500nm, 0.0022 at 630 nm, **Figure 6-3 C** blue line) of FPP with respect to rSF is significant and can be related to the presence of methacrylate groups. A further small difference of RI (0.0010 at 500 nm, 0.0009 at 630

nm, **Figure 6-3 C** red line) after the UV exposure is detectable on FPP films and is probably due to the protein crosslinking. Sericin thin films made from FA results show a RI (1.5651 at 500 nm, 1.5538 at 630 nm, **Figure 6-3 B** black line) higher than the corresponding RI for rSF. In particular this difference of RI is significant (0.0110 at 500 nm, 0.0109 at 630 nm, **Figure 6-3 D** black line) and is on the second digit, suggesting a possible use of the combination sericine/fibroin for the development of optical waveguides in core-cladding configuration[226].

Methacrylated silk sericin shows, in comparison with the unmodified material, a significant RI decrement (-0.0114 at 500 nm, -0.0116 at 630 nm, **Figure 6-3 D** red line). The UV exposure of the sericine resist has no influence on the RI (**Figure 6-3 D** blue line), in fact, the RI difference between the crosslinked and the uncrosslinked material is not significant (the blue band cross the 0 line).

6.2.4. Film morphology

To compare the effect on the superficial morphology of the two studied solvents, the films were characterized by atomic force microscopy (AFM), optical and mechanical profilometry.

At nanoscale the AFM scans showed no significant difference between films made by HFIP and FA (**Figure 6-4 A**). In both cases the root mean square (RMS) roughness results to be around 5 nm over a 25 μm^2 area. As previously observed[227] the surfaces presented nanoscale holes and the same holes appears regardless of the fabrication methods as can be clearly seen from the comparison in **Figure 6-4**.

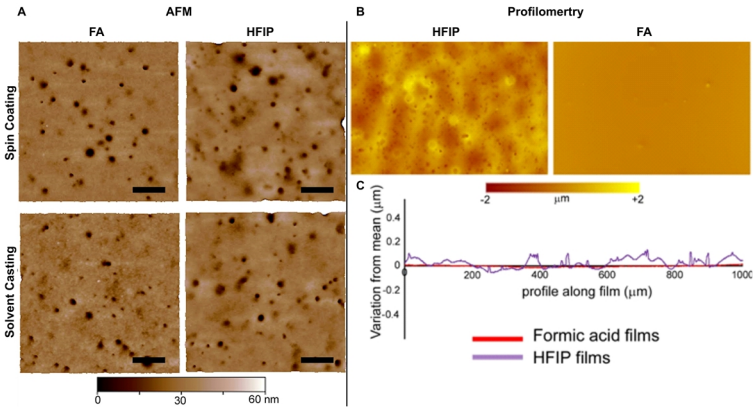

*Figure 6-4: (**A**) AFM images of films produced using different methods (Spin coating on the top, Film casting on the bottom) and different solvents (formic acid and HFIP). Scale bar = 1 µm. (**B**) optical profilometry (OP) images of films produced by casting on a glass substrate using FA and HFIP. (**C**), mean value of 5 lines profiles performed over films made by the two solvents (FA (red) and HFIP (purple)).*

Instead, in the millimetric scale, FA films are flatter than HFIP films: from the optical profilometry (OP), on a rectangular surface of 1.424 mm^2 the calculated roughness (Ra) resulted to

be 57 nm for FA and 327 nm for HFIP films (**Figure 6-4 B**). The results obtained by line profilometry (**Figure 6-4 C**) confirmed the optical profilometry and the roughness value was estimated in 13 nm for FA films and 179 nm for HFIP films.

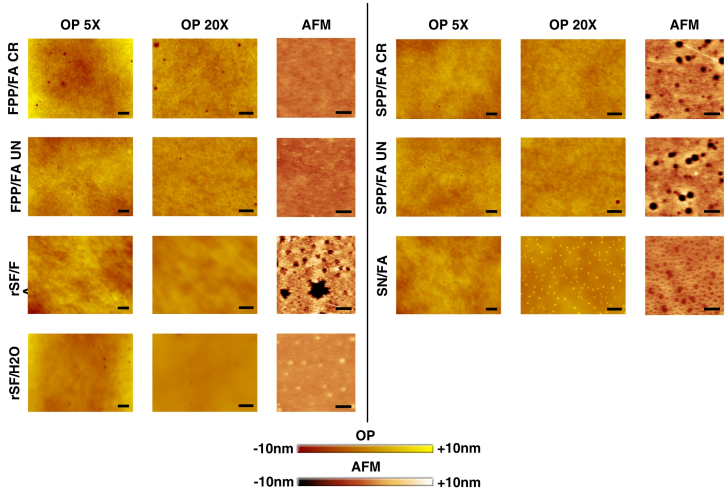

Figure 6-5: Micrographies of silk protein thin films deposited by spin coating on silicon surfaces: Optical Profilometry (OP) at 5X (scale bar 150µm) and 20X (scale bar 50 µm) magnification, and Atomic Force Microscopy (AFM) (scale bar 2 µm). Nanometric holes can be noticed at different scales in each sample. A fractal-like structure can be seen for SN/FA film in the OP taken at 20X. Despite the morphological features, all the resulting surfaces are extremely smooth and allow precise RI measurement via ellipsometry.

The results obtained from the morphological study of thin films are reported in **Figure 6-5**. The calculated average roughness (Ra) and root mean square roughness (Rrms) are reported in **Table 6-3**. At millimetric scale we used optical

profilometry. Moving to the micrometric scale, we used instead atomic force microscopy (AFM) to conduct characterization at a lower length scales (micrometer).

Film	Protein Conc. %	OP 5×		OP 20×		AFM	
		R_a [nm]	R_{rms} [nm]	R_a [nm]	R_{rms} [nm]	R_a [nm]	R_{rms} [nm]
FPP/FA Ex.	1.5	2.0	3.0	1.3	2.9	0.4	0.5
FPP/FA UnEx.	1.5	1.8	2.3	0.9	1.6	0.6	0.7
rSF/FA	2	1.9	2.6	0.8	1.1	2.3	3.3
rSF/H_2O	2	1.8	2.3	0.5	0.6	1.0	1.5
SPP/FA Ex.	1.5	1.4	1.9	1.2	0.9	1.7	2.8
SPP/FA UnEx.	1.5	1.2	1.7	1.0	2.9	1.9	3.1
SN/FA	2	1.4	1.8	0.9	1.3	0.9	1.9

*Table 6-3: Surface roughness values (arithmetic Ra, and root mean square R_{rms}) calculated from the thin films micrographies of **Figure 6-5**. Even on a large scale (OP 5×, surface of 1410 µm × 1010 µm), a R_{rms} < 3.5 nm was obtained. At a smaller scale (OP 20×, surface of 700 µm × 500 µm), this is < 3 nm. These values of roughness allow the use of the ellipsometry measurements for the determination of the RI.*

Our optimized coating methodology allowed to obtain protein films with an extremely low roughness even on large areas. On a 1410 µm×1010 µm (OP 5×) surface area the average Ra was lower than 2.5 nm (average RMS lower than 3 nm), on a to 700 µm × 500 µm (OP 20×) surface area lower than 1.5 nm (average RMS lower than 3.5 nm) and, on a 10 µm × 10

μm surface area (AFM) lower than 2.5 nm (average RMS lower than 3.5 nm).

6.2.5. Structural analysis

Figure 6-6 and **6-7** show the IR spectra (black line), the fitted peaks (green line), and the fitted curve (red line). The analysis was conducted by ATR on self-standing films (**Figure 6-6**), to compare the effect of HFIP and FA, and by DRIFT on thin films deposed on silicon substrates (**Figure 6-7**), to understand the effect of the solvent on the refractive index.

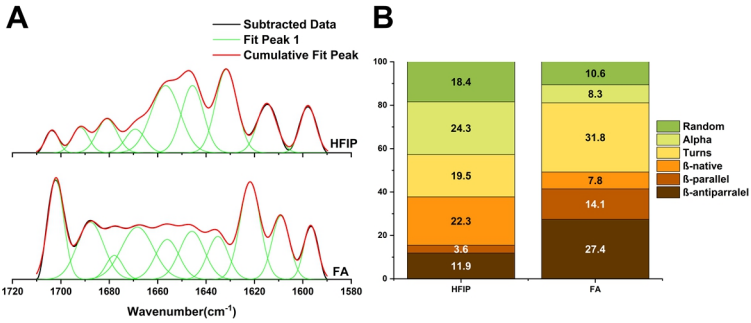

*Figure 6-6: (**A**) Deconvolved amide I peaks for the quantification of the secondary structure on self-standing films. The spectra were collected using ATR with a high resolution (0.25 cm^{-1}), more peaks respect to the previous chapters were recognizable during the deconvolution. However, the same assignment has been used. (**B**) Percentage amount of the different secondary structures. Fibroin films made by FA tends to be more crystalline than fibroin films made by HFIP.*

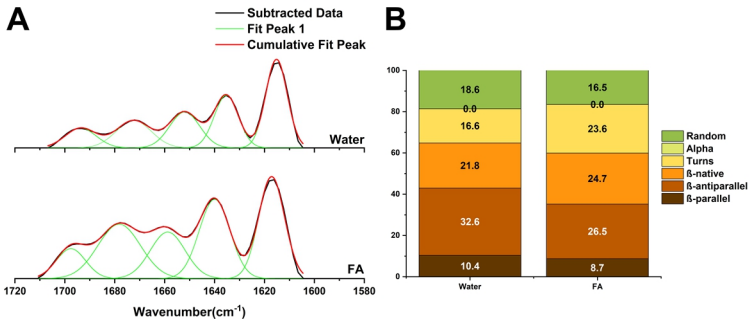

*Figure 6-7: (**A**) Deconvolved amide I peaks for the quantification of the secondary structure on thin films on silicon substrate. The spectra were collected using the DRIFT technique. (**B**) Percentage amount of the different secondary structures. Thin fibroin films made by water tend to be more crystalline than fibroin films made by FA. This effect can be related to the change in the RI.*

In case of self-standing film (**Figure 6-6 B**) formed using FA the total amount of β-sheets (49.3%) and, β-turns (31.8%), was higher than the corresponding structure in protein films prepared by HFIP (37.8% and 19.5%, respectively). Instead α-helices and random coil resulted to be lower (8.3% versus 24.3% for α-helices, and 10.6% versus 18.4% for random coil). It should be noticed that the better resolution of this spectra allowed to distinguish a higher number of peaks after the FSD.

In case of thin films, due to their thickness (between 100 and 200 nm), neither the FTIR in ATR mode nor the use of a

Grazing Angle accessory gave spectra with a signal level suitable for further analysis. The use of a diffuse reflectance (DRIFT) FTIR ensured a signal strong enough for a quantitative evaluation (**Figure 6-7 B**). In this case, thin films made starting form water solution had higher content of ß-sheet structure (64.8%) in comparison with FA based thin films, where ß-sheet structure was 59.9%.

6.2.6. Thermal analysis

DSC and TGA were conducted in order to evaluate the thermal stability of films made by FA, in comparison with the ones obtained by the other protocol (HFIP)[12,13]. DSC curves are shown in **Figure 6-8 A**.

The detected glass transition temperature (Tg) is at 150 °C and 158 °C respectively for HFIP and FA. The evaporation of water is indicated by the presence of a wide endothermic peak[50,53]: this peak is centered around 100 °C (ΔH=35.6 $J*g^{-1}$) and at 75 °C (ΔH=42.8 $J*g^{-1}$) for HFIP. An exothermic crystallization peak[53] (160.4 °C, ΔH=4.8 $J*g^{-1}$) is present only for HFIP. In FA films this peak is not present confirming the

transition to crystalline structures during the solvent drying[228,229].

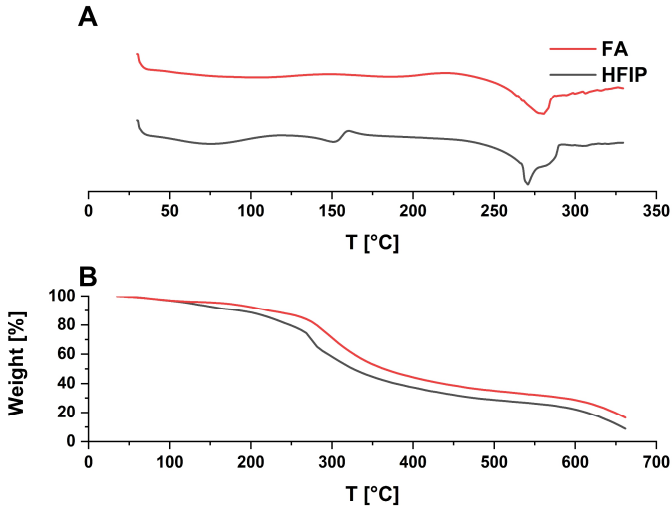

*Figure 6-8: (**A**) DSC curves and (**B**) TGA curves for films made by FA (red line) and HFIP (black line).*

In case of HFIP the degradation peak is about 271 °C (ΔH=99.1 J*g^{-1}) with a shoulder centered at 282 °C; FA instead has a single peak at 281 °C (ΔH=50.1 J*g^{-1}).

In **Figure 6-8 B** the TGA curves are shown. The initial weight loss is due to water evaporation (35-170 °C for HFIP, 35-135 °C for FA). Other low temperature volatile components provoked second weight loss (170-280 °C weight loss 29.0% for HFIP, 135-300 °C weight loss of 19.5 % for FA)[53]. The

fibroin decomposition begins at higher temperatures: at the start of the decomposition the higher remaining mass for FA films (74%) vs. HFIP films (66%) and the lower slope during the decomposition process (maximum slope 0.0058 mg $°C^{-1}$ for FA vs. 0.0074 mg.$°C^{-1}$ for HFIP) demonstrate the higher thermal stability of FA made. This can be explained by the higher amount of β-structures present in protein films made by FA, and it was previously reported in literature in a comparison made with an amorphous silk fibroin[228–230]. In fact, carboxylic acids have a potential for interacting with polar side groups of silk fibroin. As a consequence, nonpolar side groups become closer, thus increasing the possibility of local crystallization[228–230].

6.2.7. Micropatterning

As discussed above, in this work, the chemically modified photo-crosslinkable fibroin was used for the film fabrication. As shown before by our group, this variant of fibroin is very similar in properties to rSF but allows the precise patterning of microscale architectures using UV light assisted photolithography[12]. Herein the material was used as a negative

tone photoresist. However, in a previous work, the patterning was conducted using films prepared using HFIP as solvent [12,13].

The use of FA as a solvent does not alter the ability to form microscale architectures of similar resolution and fidelity using photolithography. Films fabricated using FA were exposed through a chrome photomask via contact photolithography to 365 nm UV light. Then the development of the films to remove the non-crosslinked material, revealed the microstructures attached to the substrate (typically silicon or glass slides).

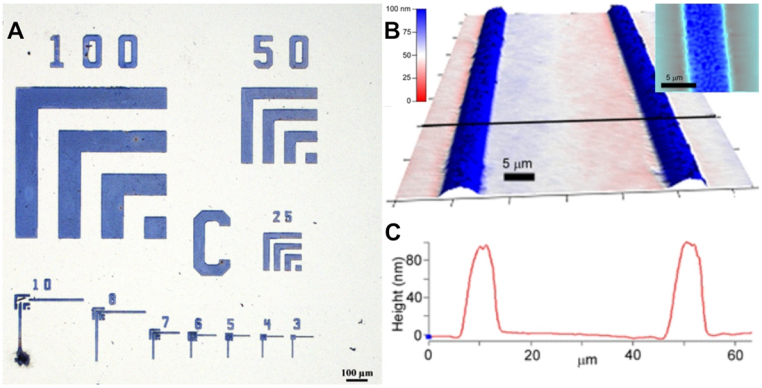

*Figure 6-9: (**A**) Optical microscopy images of fibroin micropatterns formed on a silicon surface using photolithography with formic acid as solvent. Coomassie brilliant blue was used to stain the patterns for easy visualization (scale bar = 100 µm). (**B**) AFM image of nanoscale thin films patterned with 5 µm lines. The line profile below shows that the feature height is ~100 nm. (**C**) close-up of the lines shows the uniformity of the micropatterns (scale bar = 5 µm).*

Figure 6-9 shows the result of the process applying a testing mask: even on large areas microstructures with dimensions in the 3-100 μm range can be easily obtained in a reproducible and precise fashion. The AFM imaging of **Figure 6-9 B** shows that high-resolution lines can be formed by patterning, the line profiles revealed a thickness of 100 nm, consistent with the results obtained via ellipsometry (115 nm). The surface roughness of the features was evaluated in 8.1 nm over 5 μm square area (**Figure 6-9 C**).

6.3. Discussion

The better uniformity and lower thickness obtained by FA, regardless of the coating conditions is probably related to the slower evaporation rate of this solvent that allows a better control over the process and a longer time to achieve a stable configuration.

The uniformity of the FA films can be clearly noticed comparing the films made by the two different solvents. Indeed, the standard deviation for the HFIP films is in the order of hundreds of nanometers so that the film features are large

enough to be seen by eye. In contrast, thin, optical grade films of fibroin can therefore be easily obtained using the spin casting process in combination with FA solvent and a low concentration of protein.

The role of formic acid is mainly due to its interaction with the protein in solution and, more specifically, to the hydrodynamic radius of fibroin molecules that is extremely low in FA (19 nm), even in comparison with water (139 nm)[228,230]. Even though AFM analysis at the nanoscale showed that FA and HFIP have the same morphology, optical and mechanical profilometry analysis proved the lower roughness and more uniform nature of films made from FA solution, which further ensures low surface scattering. The lower roughness of FA films at the microscale can be explained considering the interaction of the solvent with the fibroin, and the its lower volatility[228].

The optical grade thin films prepared with our optimized method allowed the determination of the refractive index using the ellipsometry. In fact, a critical issue in ellipsometric measurements is the roughness: even a small roughness (above 5 nm) can induce considerable errors[231]; higher surface

roughness (5 nm - 50 nm) produces light scattering which affects the ellipsometric results, making them difficult to fit in a suitable model.

In our films we obtained values of R_a even in the sub-nanometer, and never above 5 nm. The higher values of Rms for some samples could be related to holes or bumps clearly visible in the topography: Rms value strongly depends on the presence of peak values that are squared in the roughness calculations[232]. Also in case of thin films, nanoscale level holes were observed both in AFM and OP[227].

The determination of the RI has been conducted on these optical grade films; the knowledge of the RI is extremely important in materials that have a potential application in optics. In fact, the difference of RI between materials influence their possible application. For instance, planar fiber or optical fiber require RI difference $\geq$ to 0.01[223,224].

In our case the combination of sericin with fibroin or SPP produces RI difference on that range. Materials with RI difference value lower than 0.01, instead, could be used to produce periodic structures as photonic crystals[233–235] or Fiber Bragg gratings[236–238]. This could be the case of the RI difference

between crosslinked and uncrosslinked FPP films. It should be noted that the comparison with films in water has been done because HFIP does not allow to obtain films with a quality suitable for ellipsometric measurements.

The higher content of β-sheets structure in FA films in comparison with HFIP is not unexpected since this phenomenon has been widely reported in literature[228–230]. Even if the crystallites may decrease the transparency of films, the effect of the scattering from the surface has a greater impact[239]. For this reason, despite the higher content in ordered structure, FA films result to have a higher transmittance than HFIP films.

In case of thin films, the higher RI of films made out from water can be explained considering the secondary structure: the high content of ß-sheets in films produced by water solution is consistent with the literature for thin and ultrathin films produced by a Spin Assisted Layer by Layer method (SA-LBL)[86]. The higher crystallinity in our thin films is probably related to the presence of TMP on the substrate surface, giving rise to surface-protein interactions that facilitate the crystalline phase formation. These interactions can be partially

suppressed when the solvent is FA, which coordinates the side groups of fibroin chains [228,230].

Finally, the possibility to pattern protein resist films using the same technique previously used[212] made the use of FA as solvent a suitable alternative to perform silk lithography.

6.4. Conclusions

Photocrosslinkable fibroin was successfully dissolved in FA as an alternative solvent to the conventionally used solvent HFIP, reducing the cost and the environmental impact. In addition, the possibility to produce thin films with an extremely low roughness allowed us to characterize the refractive index of materials such as FPP and SPP that was never characterized before.

The use of FA instead of HFIP allowed to decrease the costs and the environmental impact of the previous protocol. Using the optimized spin coating procedure thin films, with a thickness between 100 and 200 nm, and an extremely low roughness, below 5 nm, can be produced. Ellipsometric measurements allowed to determine the RI of FPP and SPP, in comparison with their counterpart fibroin and sericine. Furthermore, the possibility to pattern FA made films, using contact photolithography has been proven.

The main limitation of our protocol consists in the use of FA. In fact, even though FA result to be environmentally friendly if compared to HFIP, the use of water would be of great advantage. The lack of water solubility for FPP restricts its use

to the field of film micropatterning, where the solvent is completely removed by evaporation and successive washing.

7. Final summary

This thesis work describes methodologies developed to produce silk fibroin-derived materials with the scope to implement some specific characteristics that were not fulfilled with the previous used methodologies.

Specifically, we worked on the fabrication of three materials: a chemically crosslinked silk fibroin sponge, a bulk non-porous solid starting from lyophilized fibroin, and films from a fibroin photoresist.

In the first activity, sponges were prepared using a mixer incorporating air into a water solution of a methacrylate version of fibroin (Sil-MA) containing a photoinitiator (LAP) and a surfactant (Tween20). The foam structure was blocked by UV crosslinking, and then the water was removed by freeze-drying. In this case, a design of experiment has been used to understand how the material properties change the solution composition. The porosity distribution was deduced by SEM image analysis and, some statistical measures (mean pore area and its standard deviation, median pore area and its interquartile range) were calculated and then modelled. The sponge dissolution in a simulated body fluid (SBF) was also

modelled and, in this case the ANOVA table indicates an increase in the degradation time in accordance with the amount of photoinitiator. Since all the other process parameters were kept constant, this indicates a direct relation between the chemical crosslinking and the sponge stability. Cell viability was evaluated by MTT assay. Interestingly, we were able to detect a lower cell viability for a high amount of photoinitiator, revealing its cytotoxicity in case of high concentration.

In the second activity a solid bulk fibroin has been prepared by a new low-temperature, high-pressure, sintering method. The idea was to make this technique suitable for an industrial production and for the incorporation of bioactive molecules, reducing both the time and the temperature needed with respect to other methods proposed in literature[15–18]. This task was accomplished using a statistical optimization called design of experiment (DOE), in which two parameters, related to the transition of the fibroin sponge to the solid material, were used as yields. The study of the secondary structures in combination with a thermal analysis gave us the possibility to formulate hypothesises about the mechanism underlying the transition. The experiment showed that the solid-solid transition

occurs only if compaction was achieved prior to the transition to the stable β form. Kinetics resulted therefore to be fundamental.

The last activity dealt with the preparation of films from a fibroin resist (FPP). In particular, we proposed the substitution of 1,1,1,3,3,3-hexafluoro-propan-2-ol (HFIP), used as FPP solvent, with formic acid. This resulted in three main achievements: the avoidance of harsh chemicals with difficult disposal such HFIP; the production of thin and even ultrathin films with an extremely low roughness with an excellent reproducibility; and, the possibility to determine the refractive index of the fibroin photoresist and extend its possible applications.

All the new methodologies were developed with the perspective of making silk fibroin more appealing to the industrial transfer. In fact, even though fibroin has been studied for some decades, only few products are currently available in the market. The possibility to have a faster, low temperature process (sintered fibroin), to model the material properties controlling its composition (crosslinked sponges), to avoid harsh chemicals (FPP films), and to have a good process

reproducibility (in all three cases), make the new procedures, presented in this thesis, more suitable to a scale up.

Looking into the future, a big effort should be made in the control and standardization of the processes present in literature. A special attention should be given to the process's robustness, hence to their capacity of producing the same material every single time that the process is applied, regardless the variability of the natural sources. This parameter is, in fact, rarely evaluated, and it represents one of the fundamental parameters to translate the scientific work into production. The impact of the basic treatment on the natural material should be evaluated considering all the process factors: degumming, dissolution and regeneration should be studied in a more detailed fashion in the perspective of producing a large quantity of material.

I do believe that this work is just the beginning of a more complete study on protocols revision and standardization that will be conducted in the next few years, moving from the research to the production.

8. References

[1] L.-D. D. Koh, Y. Cheng, C.-P. P. Teng, Y.-W. W. Khin, X.-J. J. Loh, S.-Y. Y. Tee, M. Low, E. Ye, H.-D. D. Yu, Y.-W. W. Zhang, M.-Y. Y. Han, *Prog. Polym. Sci.* **2015**, *46*, 86.

[2] X. Hu, D. L. Kaplan, **2011**, 207.

[3] Y. Cheng, L.-D. Koh, D. Li, B. Ji, M.-Y. Han, Y.-W. Zhang, *J. R. Soc. Interface* **2014**, *11*, 20140305.

[4] Y. Cao, B. Wang, *Int. J. Mol. Sci.* **2009**, DOI 10.3390/ijms10041514.

[5] B. Kundu, R. Rajkhowa, S. C. Kundu, X. Wang, *Adv. Drug Deliv. Rev.* **2013**, *65*, 457.

[6] J. G. Hardy, L. M. Römer, T. R. Scheibel, *Polymer (Guildf).* **2008**, *49*, 4309.

[7] Y. Qi, H. Wang, K. Wei, Y. Yang, R. Y. Zheng, I. S. Kim, K. Q. Zhang, *Int. J. Mol. Sci.* **2017**, DOI 10.3390/ijms18030237.

[8] F. G. Omenetto, **2014**, 28.

[9] D. N. Rockwood, R. C. Preda, T. Yücel, X. Wang, M. L. Lovett, D. L. Kaplan, *Nat. Protoc.* **2011**, *6*, 1612.

[10] H. Tao, D. L. Kaplan, F. G. Omenetto, *Adv. Mater.* **2012**, *24*, 2824.

[11] A. R. Murphy, D. L. Kaplan, *J. Mater. Chem.* **2009**, *19*, 6443.

[12] N. E. Kurland, T. Dey, S. C. Kundu, V. K. Yadavalli, *Adv. Mater.* **2013**, *25*, 6207.

[13] W. Liu, Z. Zhou, S. Zhang, Z. Shi, J. Tabarini, W. Lee, Y. Zhang, S. N. Gilbert Corder, X. Li, F. Dong, L. Cheng, M. Liu, D. L. Kaplan, F. G. Omenetto, G. Zhang, Y. Mao, T. H. Tao, *Adv. Sci.* **2017**, *1700191*, DOI 10.1002/advs.201700191.

[14] S. H. Kim, Y. K. Yeon, J. M. Lee, J. R. Chao, Y. J. Lee, Y. B. Seo, M. T. Sultan, O. J. Lee, J. S. Lee, S. Il Yoon, I. S. Hong, G. Khang, S. J. Lee, J. J. Yoo, C. H. Park, *Nat. Commun.* **2018**, *9*, 1.

[15] B. Marelli, N. Patel, T. Duggan, G. Perotto, E. Shirman, C. Li, D. L. Kaplan, F. G. Omenetto, *Proc. Natl. Acad. Sci.* **2017**, *114*, 451.

[16] A. Kaneko, Y. Tamada, S. Hirai, T. Kuzuya, T. Hashimoto, *Macromol. Mater. Eng.* **2012**, *297*, 272.

[17] H. A. Tuan, S. Hirai, Y. Tamada, S. Akioka, *Mater. Sci.*

Eng. C **2019**, *97*, 431.

[18] T. G. Tirta Nindhia, Y. Koyoshi, A. Kaneko, H. Sawada, M. Ohta, S. Hirai, M. Uo, *Trends Biomater. Artif. Organs* **2008**, *22*, 25.

[19] N. E. Kurland, T. Dey, C. Wang, S. C. Kundu, V. K. Yadavalli, *Adv. Mater.* **2014**, *26*, 4431.

[20] A. Bucciarelli, R. K. Pal, D. Maniglio, A. Quaranta, V. Mulloni, A. Motta, V. K. Yadavalli, A. Bucciarelli, D. Maniglio, A. Quaranta, A. Motta, V. Mulloni, **2017**, *201700110*, 1.

[21] A. Bucciarelli, V. Mulloni, D. Maniglio, R. K. Pal, V. K. Yadavalli, A. Motta, A. Quaranta, *Opt. Mater. (Amst).* **2018**, *78*, 407.

[22] S. Bai, H. Han, X. Huang, W. Xu, D. L. Kaplan, H. Zhu, Q. Lu, *Acta Biomater.* **2015**, DOI 10.1016/j.actbio.2015.04.004.

[23] N. Kasoju, U. Bora, *Adv. Healthc. Mater.* **2012**, *1*, 393.

[24] D. Maniglio, W. Bonani, C. Migliaresi, A. Motta, *J. Biomater. Sci. Polym. Ed.* **2018**, DOI 10.1080/09205063.2018.1423811.

[25] R. Nazarov, H. J. Jin, D. L. Kaplan, *Biomacromolecules*

2004, DOI 10.1021/bm034327e.

[26] J. Rnjak-Kovacina, L. S. Wray, K. A. Burke, T. Torregrosa, J. M. Golinski, W. Huang, D. L. Kaplan, *ACS Biomater. Sci. Eng.* **2015**, DOI 10.1021/ab500149p.

[27] C. Vepari, D. L. Kaplan, *Prog. Polym. Sci.* **2007**, *32*, 991.

[28] K. Liu, Z. Shi, S. Zhang, Z. Zhou, L. Sun, T. Xu, Y. Zhang, G. Zhang, X. Li, L. Chen, Y. Mao, T. H. Tao, *Adv. Healthc. Mater.* **2018**, *7*, 1701359.

[29] D. Kuhn, *T'oung Pao* **2008**, DOI 10.1163/156853284x00099.

[30] D. Christian, *Centr. Asian Surv.* **2013**, DOI 10.1080/02634937.2013.850900.

[31] A. J. Andrea, *Asian Rev. World Hist.* **2014**.

[32] S. W. Ha, H. S. Gracz, A. E. Tonelli, S. M. Hudson, *Biomacromolecules* **2005**, DOI 10.1021/bm050294m.

[33] M. S. Zafar, D. J. Belton, B. Hanby, D. L. Kaplan, C. C. Perry, *Biomacromolecules* **2015**, DOI 10.1021/bm501667j.

[34] L. D. Koh, Y. Cheng, C. P. Teng, Y. W. Khin, X. J. Loh, S. Y. Tee, M. Low, E. Ye, H. D. Yu, Y. W. Zhang, M. Y. Han, *Prog. Polym. Sci.* **2015**, *46*, 86.

[35] X. Hu, D. Kaplan, P. Cebe, *Macromolecules* **2006**, *39*, 6161.

[36] C. Jung, *J. Mol. Recognit.* **2000**, DOI 10.1002/1099-1352(200011/12)13:6<325::AID-JMR507>3.0.CO;2-C.

[37] C. Mouro, C. Jung, A. Bondon, G. Simonneaux, *Biochemistry* **1997**, DOI 10.1021/bi9700173.

[38] H. Teramoto, M. Miyazawa, *Biomacromolecules* **2005**, DOI 10.1021/bm0500547.

[39] A. Dong, P. Huang, W. S. Caughey, *Biochemistry* **1990**, DOI 10.1021/bi00465a022.

[40] U. Shimanovich, F. S. Ruggeri, E. De Genst, J. Adamcik, T. P. Barros, D. Porter, T. Müller, R. Mezzenga, C. M. Dobson, F. Vollrath, C. Holland, T. P. J. Knowles, *Nat. Commun.* **2017**, *8*, 1.

[41] B. Shivu, S. Seshadri, J. Li, K. A. Oberg, V. N. Uversky, A. L. Fink, *Biochemistry* **2013**, DOI 10.1021/bi400625v.

[42] F. S. Ruggeri, G. Longo, S. Faggiano, E. Lipiec, A. Pastore, G. Dietler, *Nat. Commun.* **2015**, DOI 10.1038/ncomms8831.

[43] G. Zandomeneghi, M. R. H. Krebs, M. G. McCammon, M. Fändrich, *Protein Sci.* **2009**, *13*, 3314.

[44] O. N. Tretinnikov, Y. Tamada, *Langmuir* **2001**, DOI 10.1021/la010791y.

[45] P. Taddei, P. Monti, *Biopolymers* **2005**, DOI 10.1002/bip.20275.

[46] E. GOORMAGHTIGH, V. CABIAUX, J. -M RUYSSCHAERT, *Eur. J. Biochem.* **1990**, DOI 10.1111/j.1432-1033.1990.tb19354.x.

[47] P. Monti, G. Freddi, *J. Raman Spectrosc.* **1998**, *29*, 297.

[48] D. Wilson, R. Valluzzi, D. Kaplan, *Biophys. J.* **2000**, DOI 10.1016/S0006-3495(00)76813-5.

[49] X. Chen, Z. Shao, N. S. Marinkovic, L. M. Miller, P. Zhou, M. R. Chance, *Biophys. Chem.* **2001**, *89*, 25.

[50] E. Callone, S. Dire, X. Hu, A. Motta, S. Dirè, X. Hu, A. Motta, *ACS Biomater. Sci. Eng.* **2016**, *2*, 758.

[51] M. Tsukada, G. Freddi, P. Monti, A. Bertoluzza, N. Kasai, *J. Polym. Sci. Part B Polym. Phys.* **1995**, *33*, 1995.

[52] M. Sonoyama, M. Miyazawa, G. Katagiri, H. Ishida, *Appl. Spectrosc.* **1997**, DOI 10.1366/0003702971940558.

[53] A. Motta, L. Fambri, C. Migliaresi, **2002**, 1658.

[54] H. J. Jin, J. Park, V. Karageorgiou, U. J. Kim, R. Valluzzi, P. Cebe, D. L. Kaplan, *Adv. Funct. Mater.* **2005**, DOI 10.1002/adfm.200400405.

[55] P. B. Tooke, *Trends Anal. Chem.* **1988**, *7*, 130.

[56] J. Kong, S. Yu, *Acta Biochim. Biophys. Sin. (Shanghai).* **2007**, *39*, 549.

[57] R. Sarroukh, E. Goormaghtigh, J. M. Ruysschaert, V. Raussens, *Biochim. Biophys. Acta - Biomembr.* **2013**, *1828*, 2328.

[58] T. Vazhnova, D. B. Lukyanov, **2013**.

[59] A. Bucciarelli, S. Chiera, A. Quaranta, V. K. Yadavalli, A. Motta, D. Maniglio, *Adv. Funct. Mater.* **2019**, *1901134*, 1901134.

[60] J. L. R. Arrondo, A. Muga, J. Castresana, F. M. Goñi, *Prog. Biophys. Mol. Biol.* **1993**, DOI 10.1016/0079-6107(93)90006-6.

[61] H. L. Casal, U. Köhler, H. H. Mantsch, *Biochim. Biophys. Acta (BBA)/Protein Struct. Mol.* **1988**, DOI 10.1016/0167-4838(88)90152-5.

[62] D. M. Byler, H. Susi, *Biopolymers* **1986**, *25*, 469.

[63] K. Ohgo, M. Kanenari, K. Okuyama, T. Asakura, in

Polym. Prepr. Japan, **2005**.

[64] G. H. Altman, F. Diaz, C. Jakuba, T. Calabro, R. L. Horan, J. Chen, H. Lu, J. Richmond, D. L. Kaplan, *Biomaterials* **2003**, *24*, 401.

[65] U. J. Kim, J. Park, H. Joo Kim, M. Wada, D. L. Kaplan, *Biomaterials* **2005**, DOI 10.1016/j.biomaterials.2004.07.044.

[66] K. Makaya, S. Terada, K. Ohgo, T. Asakura, *J. Biosci. Bioeng.* **2009**, DOI 10.1016/j.jbiosc.2009.02.015.

[67] M. Li, S. Lu, Z. Wu, H. Yan, J. Mo, L. Wang, *J. Appl. Polym. Sci.* **2001**, DOI 10.1002/1097-4628(20010321)79:12<2185::AID-APP1026>3.0.CO;2-3.

[68] Y. Tamada, *Biomacromolecules* **2005**, *6*, 3100.

[69] A. Matsumoto, J. Chen, A. L. Collette, U. Kim, G. H. Altman, P. Cebe, D. L. Kaplan, **2006**, 21630.

[70] X. Wang, J. A. Kluge, G. G. Leisk, D. L. Kaplan, *Biomaterials* **2008**, *29*, 1054.

[71] X. Wang, J. Kluge, G. . Leisk, D. . Kaplan, *US Pat. 8,722,067* **2014**.

[72] T. Yucel, P. Cebe, D. L. Kaplan, *Biophys. J.* **2009**, DOI

10.1016/j.bpj.2009.07.028.

[73] P. R. Laity, C. Holland, *Int. J. Mol. Sci.* **2016**, DOI 10.3390/ijms17111812.

[74] H. Wang, N. Mao, X. Hu, H. Shao, X. Jin, *J. Wuhan Univ. Technol. Mater. Sci. Ed.* **2011**, *26*, 262.

[75] A. Matsumoto, J. Chen, A. L. Collette, U. J. Kim, G. H. Altman, P. Cebe, D. L. Kaplan, *J. Phys. Chem. B* **2006**, *110*, 21630.

[76] A. E. Terry, D. P. Knight, D. Porter, F. Vollrath, *Biomacromolecules* **2004**, DOI 10.1021/bm034381v.

[77] D. L. Kaplan, *Pat. US* **2011**.

[78] C. W. P. Foo, E. Bini, J. Hensman, D. P. Knight, R. V. Lewis, D. L. Kaplan, *Appl. Phys. A Mater. Sci. Process.* **2006**, DOI 10.1007/s00339-005-3426-7.

[79] Q. Lu, Y. Huang, M. Li, B. Zuo, S. Lu, J. Wang, H. Zhu, D. L. Kaplan, *Acta Biomater.* **2011**, DOI 10.1016/j.actbio.2011.02.032.

[80] D. Maniglio, W. Bonani, G. Bortoluzzi, E. Servoli, A. Motta, C. Migliaresi, *J. Bioact. Compat. Polym.* **2010**, *25*, 441.

[81] L. Zhou, X. Chen, Z. Shao, Y. Huang, D. P. Knight, *J.*

Phys. Chem. B **2005**, DOI 10.1021/jp050883m.

[82] D. Su, M. Yao, J. Liu, Y. Zhong, X. Chen, Z. Shao, *ACS Appl. Mater. Interfaces* **2017**, DOI 10.1021/acsami.7b04623.

[83] M. B. Applegate, B. P. Partlow, J. Coburn, B. Marelli, C. Pirie, R. Pineda, D. L. Kaplan, F. G. Omenetto, *Adv. Mater.* **2016**, *28*, n/a.

[84] J. L. Whittaker, N. R. Choudhury, N. K. Dutta, A. Zannettino, *J. Mater. Chem. B* **2014**, *2*, 6259.

[85] X. Wu, J. Hou, M. Li, J. Wang, D. L. Kaplan, S. Lu, *Acta Biomater.* **2012**, DOI 10.1016/j.actbio.2012.03.007.

[86] C. Jiang, X. Wang, R. Gunawidjaja, Y. H. Lin, M. K. Gupta, D. L. Kaplan, R. R. Naik, V. V. Tsukruk, *Adv. Funct. Mater.* **2007**, *17*, 2229.

[87] B. Marelli, M. A. Brenckle, D. L. Kaplan, F. G. Omenetto, *Sci. Rep.* **2016**, DOI 10.1038/srep25263.

[88] D. H. Kim, J. Viventi, J. J. Amsden, J. Xiao, L. Vigeland, Y. S. Kim, J. A. Blanco, B. Panilaitis, E. S. Frechette, D. Contreras, D. L. Kaplan, F. G. Omenetto, Y. Huang, K. C. Hwang, M. R. Zakin, B. Litt, J. A. Rogers, *Nat. Mater.* **2010**, DOI 10.1038/nmat2745.

[89] Z. Shi, F. Zheng, Z. Zhou, M. Li, Z. Fan, H. Ye, S. Zhang, T. Xiao, L. Chen, T. H. Tao, Y. L. Sun, Y. Mao, *Adv. Sci.* **2019**, DOI 10.1002/advs.201801617.

[90] B. Zhu, H. Wang, W. R. Leow, Y. Cai, X. J. Loh, M. Y. Han, X. Chen, *Adv. Mater.* **2016**, *28*, 4250.

[91] C. H. Wang, C. Y. Hsieh, J. C. Hwang, *Adv. Mater.* **2011**, DOI 10.1002/adma.201004071.

[92] P. Tseng, B. Napier, L. Garbarini, D. L. Kaplan, F. G. Omenetto, *Adv. Mater.* **2018**, DOI 10.1002/adma.201703257.

[93] H. Tao, M. A. Brenckle, M. Yang, J. Zhang, M. Liu, S. M. Siebert, R. D. Averitt, M. S. Mannoor, M. C. McAlpine, J. A. Rogers, D. L. Kaplan, F. G. Omenetto, *Adv. Mater.* **2012**, *24*, 1067.

[94] M. A. Brenckle, D. L. Kaplan, F. G. Omenetto, *Adv. Mater. Interfaces* **2016**, DOI 10.1002/admi.201600094.

[95] M. A. Brenckle, H. Tao, S. Kim, M. Paquette, D. L. Kaplan, F. G. Omenetto, *Adv. Mater.* **2013**, *25*, 2409.

[96] J. J. Amsden, P. Domachuk, A. Gopinath, R. D. White, L. D. Negro, D. L. Kaplan, F. G. Omenetto, *Adv. Mater.* **2010**, *22*, 1746.

[97] M. A. Brenckle, B. Partlow, H. Tao, M. B. Applegate, A. Reeves, M. Paquette, B. Marelli, D. L. Kaplan, F. G. Omenetto, *Adv. Funct. Mater.* **2016**, *26*, 44.

[98] Q. Wang, G. Han, S. Yan, Q. Zhang, *Materials (Basel).* **2019**, DOI 10.3390/ma12030504.

[99] H. J. Jin, J. Chen, V. Karageorgiou, G. H. Altman, D. L. Kaplan, *Biomaterials* **2004**, DOI 10.1016/S0142-9612(03)00609-4.

[100] C. Chen, C. Chuanbao, M. Xilan, T. Yin, Z. Hesun, *Polymer (Guildf).* **2006**, DOI 10.1016/j.polymer.2006.07.009.

[101] X. Mo, B. Sun, T. Wu, D. Li, in *Electrospinning Nanofabrication Appl.*, **2019**.

[102] F. Zhang, B. Zuo, Z. Fan, Z. Xie, Q. Lu, X. Zhang, D. L. Kaplan, *Biomacromolecules* **2012**, DOI 10.1021/bm201719s.

[103] A. S. Lammel, X. Hu, S. H. Park, D. L. Kaplan, T. R. Scheibel, *Biomaterials* **2010**, DOI 10.1016/j.biomaterials.2010.02.024.

[104] E. M. Pritchard, D. L. Kaplan, *Expert Opin. Drug Deliv.* **2011**, DOI 10.1517/17425247.2011.568936.

[105] E. Wenk, H. P. Merkle, L. Meinel, *J. Control. Release* **2011**, DOI 10.1016/j.jconrel.2010.11.007.

[106] T. Hino, M. Tanimoto, S. Shimabayashi, *J. Colloid Interface Sci.* **2003**, DOI 10.1016/S0021-9797(03)00584-8.

[107] J. H. Yeo, K. G. Lee, Y. W. Lee, S. Y. Kim, *Eur. Polym. J.* **2003**, DOI 10.1016/S0014-3057(02)00359-2.

[108] X. Wang, E. Wenk, A. Matsumoto, L. Meinel, C. Li, D. L. Kaplan, *J. Control. Release* **2007**, DOI 10.1016/j.jconrel.2006.11.021.

[109] E. Wenk, A. J. Wandrey, H. P. Merkle, L. Meinel, *J. Control. Release* **2008**, DOI 10.1016/j.jconrel.2008.08.005.

[110] Z. Cao, X. Chen, J. Yao, L. Huang, Z. Shao, *Soft Matter* **2007**, DOI 10.1039/b703139d.

[111] T. Tanaka, T. Tanigami, K. Yamaura, *Polym. Int.* **1998**, DOI 10.1002/(SICI)1097-0126(199802)45:2<175::AID-PI883>3.0.CO;2-K.

[112] X. Wang, T. Yucel, Q. Lu, X. Hu, D. L. Kaplan, *Biomaterials* **2010**, DOI 10.1016/j.biomaterials.2009.11.002.

[113] A. Lammel, M. Schwab, U. Slotta, G. Winter, T. Scheibel, *ChemSusChem* **2008**, DOI 10.1002/cssc.200800030.

[114] R. Rajkhowa, L. Wang, X. Wang, *Powder Technol.* **2008**, DOI 10.1016/j.powtec.2008.01.005.

[115] R. Rajkhowa, L. J. Wang, X. A. Wang, *Res. Progresses Mod. Technol. Silk, Text. Mech. I* **2007**.

[116] M. Humenik, G. Lang, T. Scheibel, *Wiley Interdiscip. Rev. Nanomedicine Nanobiotechnology* **2018**, DOI 10.1002/wnan.1509.

[117] S. Bai, S. Liu, C. Zhang, W. Xu, Q. Lu, H. Han, D. L. Kaplan, H. Zhu, *Acta Biomater.* **2013**, DOI 10.1016/j.actbio.2013.04.033.

[118] P. Chen, H. S. Kim, C. Y. Park, H. S. Kim, I. J. Chin, H. J. Jin, *Macromol. Res.* **2008**, DOI 10.1007/BF03218556.

[119] S. Ling, K. Jin, D. L. Kaplan, M. J. Buehler, *Nano Lett.* **2016**, acs. nanolett.6b01195.

[120] H. Y. Wang, Y. Y. Chen, Y. Q. Zhang, *Mater. Sci. Eng. C* **2015**, DOI 10.1016/j.msec.2014.12.028.

[121] B. B. Mandal, A. Grinberg, E. Seok Gil, B. Panilaitis, D. L. Kaplan, *Proc. Natl. Acad. Sci.* **2012**, DOI

10.1073/pnas.1119474109.

[122] B. Ganesh Kumar, R. Melikov, M. Mohammadi Aria, A. Ural Yalcin, E. Begar, S. Sadeghi, K. Guven, S. Nizamoglu, *ACS Biomater. Sci. Eng.* **2018**, *4*, 1463.

[123] J. J. Amsden, P. Domachuk, A. Gopinath, R. D. White, L. D. Negro, D. L. Kaplan, F. G. Omenetto, *Adv. Mater.* **2010**, *22*, 1746.

[124] J. Park, S.-G. G. Lee, B. Marelli, M. Lee, T. Kim, H.-K. K. Oh, H. Jeon, F. G. Omenetto, S. Kim, *RSC Adv.* **2016**, *6*, 39330.

[125] Y. L. Sun, Q. Li, S. M. Sun, J. C. Huang, B. Y. Zheng, Q. D. Chen, Z. Z. Shao, H. B. Sun, *Nat. Commun.* **2015**, *6*, DOI 10.1038/ncomms9612.

[126] S. Kim, B. Marelli, M. A. Brenckle, A. N. Mitropoulos, E.-S. S. Gil, K. Tsioris, H. Tao, D. L. Kaplan, F. G. Omenetto, *Nat. Nanotechnol.* **2014**, *9*, 306.

[127] S. Ghosh, S. T. Parker, X. Wang, D. L. Kaplan, J. A. Lewis, *Adv. Funct. Mater.* **2008**, DOI 10.1002/adfm.200800040.

[128] J. B. Costa, J. Silva-Correia, J. M. Oliveira, R. L. Reis, *Adv. Healthc. Mater.* **2017**, DOI

10.1002/adhm.201701021.

[129] A. M. Compaan, K. Christensen, Y. Huang, *ACS Biomater. Sci. Eng.* **2017**, DOI 10.1021/acsbiomaterials.6b00432.

[130] S. Das, F. Pati, Y. J. Choi, G. Rijal, J. H. Shim, S. W. Kim, A. R. Ray, D. W. Cho, S. Ghosh, *Acta Biomater.* **2015**, DOI 10.1016/j.actbio.2014.09.023.

[131] S. Midha, S. Ghosh, in *Regen. Med. Lab. to Clin.*, **2017**, pp. 259–276.

[132] T. Furuzono, K. Ishihara, N. Nakabayashi, Y. Tamada, *Biomaterials* **2000**, *21*, 327.

[133] W. Liu, S. Zhang, W. Lee, T. H. Tao, in *Proc. IEEE Int. Conf. Micro Electro Mech. Syst.*, **2017**.

[134] M. Xu, S. Pradhan, F. Agostinacchio, R. K. Pal, G. Greco, B. Mazzolai, N. M. Pugno, A. Motta, V. K. Yadavalli, *Adv. Mater. Interfaces* **2019**, DOI 10.1002/admi.201801822.

[135] R. K. Pal, A. A. Farghaly, C. Wang, M. M. Collinson, S. C. Kundu, V. K. Yadavalli, *Biosens. Bioelectron.* **2016**, *81*, 294.

[136] R. K. Pal, V. K. Yadavalli, *Nanotechnology* **2018**, DOI

10.1088/1361-6528/aac855.

[137] R. K. Pal, N. E. Kurland, C. Jiang, S. C. Kundu, N. Zhang, V. K. Yadavalli, *Eur. Polym. J.* **2016**, *85*, 421.

[138] Z. Z. Fang, *Sintering of Advanced Materials*, **2010**.

[139] J. L. Johnson, *Sintering of Advanced Materials*, **2010**.

[140] M. A. Brenckle, B. Partlow, H. Tao, D. L. Kaplan, F. G. Omenetto, *Biomacromolecules* **2013**, *14*, 2189.

[141] R. A. Lawson, A. P. G. Robinson, *Front. Nanosci.* **2016**, *11*, 1.

[142] M. Kumar Sah, A. Kumar, K. Pramanik, *Int. J. Bioinforma.* **2010**, *2*, 33.

[143] D. T. Pham, N. Saelim, W. Tiyaboonchai, *Int. J. Appl. Pharm.* **2018**, *10*, 195.

[144] C. Perucca Orfei, G. Talò, M. Viganò, S. Perteghella, G. Lugano, F. Fabro Fontana, E. Ragni, A. Colombini, P. De Luca, M. Moretti, M. Torre, L. de Girolamo, *Pharmaceutics* **2018**, *10*, 200.

[145] S. F. Arnold, *Design of Experiments with MINITAB*, **2006**.

[146] J. Antony, *Design of Experiments for Engineers and Scientists*, **2003**.

[147] D. C. Montgomery, *Design and Analysis of Experiments Eighth Edition*, **2012**.

[148] G. W. Oehlert, *A First Course in Design and Analysis of Experiments*, **2003**.

[149] P. Di Lazzaro, S. Bollanti, F. Flora, L. Mezi, D. Murra, A. Torre, *IEEE Trans. Plasma Sci.* **2009**, *37*, 475.

[150] W. Rasband, *U. S. Natl. Institutes Heal. Bethesda, Maryland, USA* **2012**.

[151] C. A. Schneider, W. S. Rasband, K. W. Eliceiri, *Nat. Methods* **2012**, DOI 10.1038/nmeth.2089.

[152] K. Kucharczyk, M. Weiss, K. Jastrzebska, M. Luczak, A. Ptak, M. Kozak, A. Mackiewicz, H. Dams-Kozlowska, *Int. J. Nanomedicine* **2018**, DOI 10.2147/IJN.S168081.

[153] L. A. Safonova, M. M. Bobrova, O. I. Agapova, M. S. Kotliarova, A. Y. Arkhipova, M. M. Moisenovich, I. I. Agapov, *Sovrem. Tehnol. v Med.* **2015**, *7*, 6.

[154] T. L. Riss, R. A. Moravec, A. L. Niles, S. Duellman, H. A. Benink, T. J. Worzella, L. Minor, *Cell Viability Assays*, **2004**.

[155] C. Holland, K. Numata, J. Rnjak-Kovacina, F. P. Seib, *Adv. Healthc. Mater.* **2019**, DOI

10.1002/adhm.201800465.

[156] S. C. Kundu, B. C. Dash, R. Dash, D. L. Kaplan, *Prog. Polym. Sci.* **2008**, *33*, 998.

[157] V. Karageorgiou, D. Kaplan, *Biomaterials* **2005**, DOI 10.1016/j.biomaterials.2005.02.002.

[158] D. W. Hutmacher, in *Biomater. Silver Jubil. Compend.*, **2006**.

[159] G. Chen, T. Ushida, T. Tateishi, *Macromol. Biosci.* **2002**, DOI 10.1002/1616-5195(20020201)2:2<67::AID-MABI67>3.0.CO;2-F.

[160] S. J. Hollister, *Nat. Mater.* **2005**, *4*, 518.

[161] C. J. Liao, C. F. Chen, J. H. Chen, S. F. Chiang, Y. J. Lin, K. Y. Chang, *J. Biomed. Mater. Res.* **2002**, DOI 10.1002/jbm.10030.

[162] D. Yao, S. Dong, Q. Lu, X. Hu, D. L. Kaplan, B. Zhang, H. Zhu, *Biomacromolecules* **2012**, DOI 10.1021/bm301197h.

[163] X. Zhang, C. Cao, X. Ma, Y. Li, *J. Mater. Sci. Mater. Med.* **2012**, DOI 10.1007/s10856-011-4476-3.

[164] L. P. Yan, J. M. Oliveira, A. L. Oliveira, S. G. Caridade, J. F. Mano, R. L. Reis, *Acta Biomater.* **2012**, DOI

10.1016/j.actbio.2011.09.037.

[165] Y. Pei, X. Liu, S. Liu, Q. Lu, J. Liu, D. L. Kaplan, H. Zhu, *Acta Biomater.* **2015**, DOI 10.1016/j.actbio.2014.11.016.

[166] B. B. Mandal, S. C. Kundu, *Macromol. Biosci.* **2008**, DOI 10.1002/mabi.200800113.

[167] Y. S. Nam, J. J. Yoon, T. G. Park, *J. Biomed. Mater. Res.* **2000**, DOI 10.1002/(SICI)1097-4636(2000)53:1<1::AID-JBM1>3.0.CO;2-R.

[168] D. Yao, H. Liu, Y. Fan, *RSC Adv.* **2016**, DOI 10.1039/c6ra10670f.

[169] A. Kramschuster, L. S. Turng, in *Handb. Biopolym. Biodegrad. Plast. Prop. Process. Appl.*, **2012**.

[170] J. Coates, *Encycl. Anal. Chem.* **2000**, 10815.

[171] H. Lin, D. Zhang, P. G. Alexander, G. Yang, J. Tan, A. W. M. Cheng, R. S. Tuan, *Biomaterials* **2013**, DOI 10.1016/j.biomaterials.2012.09.048.

[172] K. Dubbin, A. Tabet, S. C. Heilshorn, *Biofabrication* **2017**, DOI 10.1088/1758-5090/aa869f.

[173] L. A. Sawicki, A. M. Kloxin, *J. Vis. Exp.* **2016**, DOI 10.3791/54462.

[174] C. Wu, J. Y. Lim, G. G. Fuller, L. Cegelski, *Langmuir*

2013, DOI 10.1021/la304710k.

[175] D. K. Chou, R. Krishnamurthy, T. W. Randolph, J. F. Carpenter, M. C. Manning, *J. Pharm. Sci.* **2005**, DOI 10.1002/jps.20365.

[176] S. Okino, M. Ikeo, Y. Ueno, D. Taneda, *Bioresour. Technol.* **2013**, DOI 10.1016/j.biortech.2013.05.078.

[177] B. A. Kerwin, *J. Pharm. Sci.* **2008**, DOI 10.1002/jps.21190.

[178] T. Scherzer, U. Decker, in *Radiat. Phys. Chem.*, **1999**.

[179] A. García-Lizarribar, X. Fernández-Garibay, F. Velasco-Mallorquí, A. G. Castaño, J. Samitier, J. Ramon-Azcon, *Macromol. Biosci.* **2018**, DOI 10.1002/mabi.201800167.

[180] S. Tian, W. Ren, G. Li, R. Yang, T. Wang, *Geofluids* **2017**, DOI 10.1155/2017/7492328.

[181] T. J. MARSHALL, *J. Soil Sci.* **1958**, DOI 10.1111/j.1365-2389.1958.tb01892.x.

[182] M. Kesti, M. Müller, J. Becher, M. Schnabelrauch, M. D'Este, D. Eglin, M. Zenobi-Wong, *Acta Biomater.* **2015**, DOI 10.1016/j.actbio.2014.09.033.

[183] A. Linnenberger, M. I. Bodine, C. Fiedler, J. J. Roberts, S. C. Skaalure, J. P. Quinn, S. J. Bryant, M. Cole, R. R.

McLeod, *Opt. Express* **2013**, DOI 10.1364/oe.21.010269.

[184] J. Magoshi, Y. Magoshi, M. A. Becker, M. Kato, Z. Han, T. Tanaka, S. ichi Inoue, S. Nakamura, *Thermochim. Acta* **2000**, *352*, 165.

[185] R. M. Daniel, M. Dines, H. H. Petach, *Biochem. J.* **1996**, *317 (Pt 1*, 1.

[186] N. Agarwal, D. a Hoagland, R. J. Farris, *J. Appl. Polym. Sci.* **1997**, *63*, 401.

[187] X. Hu, D. Kaplan, P. Cebe, *Thermochim. Acta* **2007**, *461*, 137.

[188] K. Yazawa, K. Ishida, H. Masunaga, T. Hikima, K. Numata, *Biomacromolecules* **2016**, *17*, 1057.

[189] Z. Gao, Z. Zhou, H. Tao, N. Qin, in *2018 IEEE Micro Electro Mech. Syst.*, IEEE, **2018**, pp. 498–500.

[190] H. Yoshimizu, T. Asakura, **1990**, *40*, 127.

[191] A. Gholami, H. Tavanai, A. R. Moradi, *J. Nanoparticle Res.* **2011**, *13*, 2089.

[192] J. Zhong, X. Liu, D. Wei, J. Yan, P. Wang, G. Sun, D. He, *Int. J. Biol. Macromol.* **2015**, *76*, 195.

[193] P. Defilippi, C. Olivo, M. Venturino, L. Dolce, L. Silengo,

G. Tarone, *Microsc. Res. Tech.* **1999**, DOI 10.1002/(SICI)1097-0029(19991001)47:1<67::AID-JEMT7>3.0.CO;2-P.

[194] X. Hu, K. Shmelev, L. Sun, E. S. Gil, S. H. Park, P. Cebe, D. L. Kaplan, *Biomacromolecules* **2011**, DOI 10.1021/bm200062a.

[195] B. D. Lawrence, F. Omenetto, K. Chui, D. L. Kaplan, *J. Mater. Sci.* **2008**, DOI 10.1007/s10853-008-2961-y.

[196] B. M. Min, L. Jeong, K. Y. Lee, W. H. Park, *Macromol. Biosci.* **2006**, DOI 10.1002/mabi.200500246.

[197] B. D. Lawrence, S. Wharram, J. A. Kluge, G. G. Leisk, F. G. Omenetto, M. I. Rosenblatt, D. L. Kaplan, *Macromol. Biosci.* **2010**, *10*, 393.

[198] K. Ramesh, N. Naresh, Pumlianmunga, E. S. R. Gopal, *Key Eng. Mater.* **2016**, *702*, 43.

[199] B. . Joiner, J. . Thompson, *J. Non. Cryst. Solids* **1976**, *21*, 215.

[200] S. J. Rzoska, *Front. Mater.* **2017**, *4*, DOI 10.3389/fmats.2017.00033.

[201] J. Pionteck, *Polymers (Basel).* **2018**, *10*, 578.

[202] B. D. Ulery, L. S. Nair, C. T. Laurencin, *J. Polym. Sci.*

Part B Polym. Phys. **2011**, DOI 10.1002/polb.22259.

[203] N. Minoura, S. I. Aiba, M. Higuchi, Y. Gotoh, M. Tsukada, Y. Imai, *Biochem. Biophys. Res. Commun.* **1995**, DOI 10.1006/bbrc.1995.1368.

[204] N. Minoura, S. -I Aiba, Y. Gotoh, M. Tsukada, Y. Imai, *J. Biomed. Mater. Res.* **1995**, DOI 10.1002/jbm.820291008.

[205] P. W. Madden, J. N. X. Lai, K. A. George, T. Giovenco, D. G. Harkin, T. V. Chirila, *Biomaterials* **2011**, DOI 10.1016/j.biomaterials.2010.12.034.

[206] B. B. Mandal, S. C. Kundu, *Biomaterials* **2009**, DOI 10.1016/j.biomaterials.2009.02.006.

[207] S. Talukdar, M. Mandal, D. W. Hutmacher, P. J. Russell, C. Soekmadji, S. C. Kundu, *Biomaterials* **2011**, DOI 10.1016/j.biomaterials.2010.11.052.

[208] T. L. Liu, J. C. Miao, W. H. Sheng, Y. F. Xie, Q. Huang, Y. B. Shan, J. C. Yang, *J. Zhejiang Univ. Sci. B* **2010**, DOI 10.1631/jzus.B0900163.

[209] A. U. Daniels, M. K. Chang, K. P. Andriano, *J. Appl. Biomater.* **1990**, DOI 10.1002/jab.770010109.

[210] H. Perry, A. Gopinath, D. L. Kaplan, L. D. Negro, F. G.

Omenetto, *Adv. Mater.* **2008**, *20*, 3070.

[211] K. Tsioris, H. Tao, M. Liu, J. A. Hopwood, D. L. Kaplan, R. D. Averitt, F. G. Omenetto, *Adv. Mater.* **2011**, *23*, 2015.

[212] F. Galeotti, A. Andicsova, S. Yunus, C. Botta, *Soft Matter* **2012**, *8*, 4815.

[213] Y. Tsuboi, H. Adachi, K. Yamada, H. Miyasaka, A. Itaya, *Jpn. J. Appl. Phys.* **2002**, *41*, 4772.

[214] F. Edition, *Sittig ' S Handbook of Toxic and Hazardous*, **n.d.**

[215] R. K. Pal, N. E. Kurland, C. Wang, S. C. Kundu, V. K. Yadavalli, *ACS Appl. Mater. Interfaces* **2015**, *7*, 8809.

[216] X. Wang, X. Hu, A. Daley, O. Rabotyagova, P. Cebe, D. L. Kaplan, *J. Control. Release* **2007**, *121*, 190.

[217] K. R. McIntosh, J. N. Cotsell, J. S. Cumpston, A. W. Norris, N. E. Powell, B. M. Ketola, in *Conf. Rec. IEEE Photovolt. Spec. Conf.*, **2009**.

[218] S. Nizamoglu, M. C. Gather, M. Humar, M. Choi, S. Kim, K. S. Kim, S. K. Hahn, G. Scarcelli, M. Randolph, R. W. Redmond, S. H. Yun, *Nat. Commun.* **2016**, *7*, 10374.

[219] R. Melikov, D. A. Press, B. G. Kumar, I. B. Dogru, S.

Sadeghi, M. Chirea, I. Yilgör, S. Nizamoglu, *Sci. Rep.* **2017**, DOI 10.1038/s41598-017-07817-1.

[220] C. G. Parazzoli, R. B. Greegor, K. Li, B. E. C. Koltenbah, M. Tanielian, *Phys. Rev. Lett.* **2003**, DOI 10.1103/PhysRevLett.90.107401.

[221] P. G. Bergmann, *J. Acoust. Soc. Am.* **1946**, DOI 10.1121/1.1916333.

[222] G. Perotto, Y. Zhang, D. Naskar, N. Patel, D. L. Kaplan, **2017**, *103702*, DOI 10.1063/1.4998950.

[223] S. T. Parker, P. Domachuk, J. Amsden, J. Bressner, J. a. Lewis, D. L. Kaplan, F. C. Omenetto, *Adv. Mater.* **2009**, *21*, 2411.

[224] M. B. Applegate, G. Perotto, D. L. Kaplan, F. G. Omenetto, *Biomed. Opt. Express* **2015**, *6*, 4221.

[225] G. Perotto, M. Cittadini, H. Tao, S. Kim, M. Yang, D. L. Kaplan, A. Martucci, F. G. Omenetto, *Adv. Mater.* **2015**, *27*, 6728.

[226] J. Arnaud, *Opt. Quantum Electron.* **1980**, DOI 10.1007/BF00620035.

[227] B. Kundu, N. E. Kurland, V. K. Yadavalli, S. C. Kundu, *Int. J. Biol. Macromol.* **2014**, *70*, 70.

[228] I. C. Um, H. Y. Kweon, K. G. Lee, Y. H. Park, *Int. J. Biol. Macromol.* **2003**, *33*, 203.

[229] S. W. Ha, A. E. Tonelli, S. M. Hudson, *Biomacromolecules* **2005**, *6*, 1722.

[230] I. C. Um, H. Kweon, Y. H. Park, S. Hudson, *Int. J. Biol. Macromol.* **2001**, *29*, 91.

[231] C. A. Fenstermaker, F. L. McCrackin, *Surf. Sci.* **1969**, *16*, 85.

[232] T. R. Thomas, *Precis. Eng.* **1981**, *3*, 97.

[233] Q. Li, N. Qi, Y. Peng, Y. Zhang, L. Shi, X. Zhang, Y. Lai, K. Wei, I. S. Kim, K.-Q. Q. Zhang, *RSC Adv.* **2017**, *7*, 17889.

[234] E. Colusso, G. Perotto, Y. Wang, M. Sturaro, F. Omenetto, A. Martucci, *J. Mater. Chem. C* **2017**, *5*, 3924.

[235] Y. Y. Diao, X. Y. Liu, G. W. Toh, L. Shi, J. Zi, *Adv. Funct. Mater.* **2013**, *23*, 5373.

[236] V. Rajoria, J. Singh, M. Tiwari, A. Khare, **2011**, *2*, 61.

[237] K. O. Hill, G. Meltz, *J. Light. Technol.* **1997**, *15*, 1263.

[238] A. P. Zhang, S. Gao, G. Yan, Y. Bai, *Photonic Sensors* **2012**, *2*, 1.

[239] M. Tsukada, K. Hirabayashi, *J. Polym. Sci. Part C-Polymer Lett.* **1980**, *18*, 507.

Acknowledgement

I want to express my profound gratitude to my advisors: prof. Alberto Quaranta and prof. Devid Maniglio. They were able to encourage and guide me whenever I was lost in my thoughts (and it happened quite a lot). To prof. Antonella Motta, that opened the path with her studies on silk and tissue engineering in the University of Trento and, thanks to her collaborations, to travel the world. To Dr. Vamsi Yadavalli, that took me under his wings in the United States when I was vising his laboratory at the Virginia Commonwealth University, and with whom I had a lot of great conversations about our respective scientific visions. To prof. Gilson Kang, who welcomed me in South Korea and to his “family”: the Gilson Lab in Chonbuk University. To Dr. Viviana Mulloni for her patience in helping me perform several measurements and in collaborating to translate my ideas into something real. To all the marvelous people and colleagues that I have met in these three years at BioTech: Rosasilvia Raggio, Silvia Chiera, Francesca Agostinacchio, Sofia Santi, Nicola Cagol, Cristiano Carlomagno, Filippo Benetti, and Lorenzo Moschini. And to all the other colleagues that I have met at the University of Trento: Enrico Zanazzi, Giuglia Fredi, Daniele

Rigotti, Massimiliano Tommasselli, Alessandra Speccher and Fabiano Zenatti. To my mother and my father, who even in the moments of hardest difficulties always supported me. To my sister Meri and to my nephews Naohel and Agnese. To my Finnish sister Tuulia her husband Ville, and to my Finnish nephew Angela.